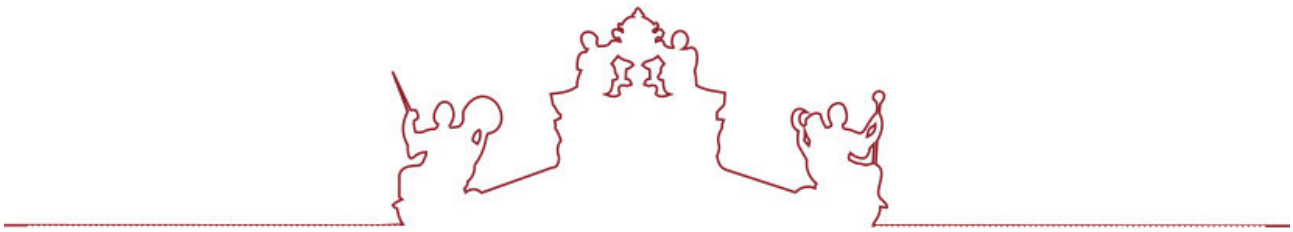

Universidade de Évora - Instituto de Investigação e Formação Avançada
Università degli Studi di Roma "La Sapienza" Aristotle University of Thessaloniki

Mestrado em Ciência dos Materiais Arqueológicos (ARCHMAT)

Dissertação

Archaeometric analysis of Terra Sigillata pottery from the Roman Cistern at Spoletino, Viterbo, Italy.

Sotiria Stromatia

Orientador(es) | Emanuela Borgia
Laura Medeghini

Évora 2023

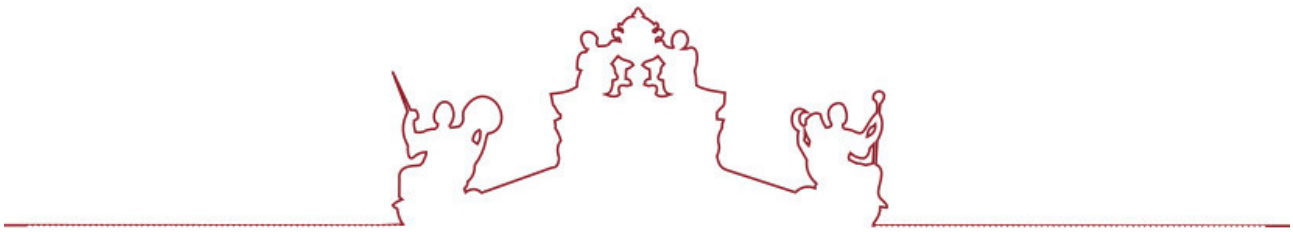

Universidade de Évora - Instituto de Investigação e Formação Avançada
Università degli Studi di Roma "La Sapienza" Aristotle University of Thessaloniki

Mestrado em Ciência dos Materiais Arqueológicos (ARCHMAT)

Dissertação

Archaeometric analysis of Terra Sigillata pottery from the Roman Cistern at Spoletino, Viterbo, Italy.

Sotiria Stromatia

Orientador(es) | Emanuela Borgia
Laura Medeghini

Évora 2023

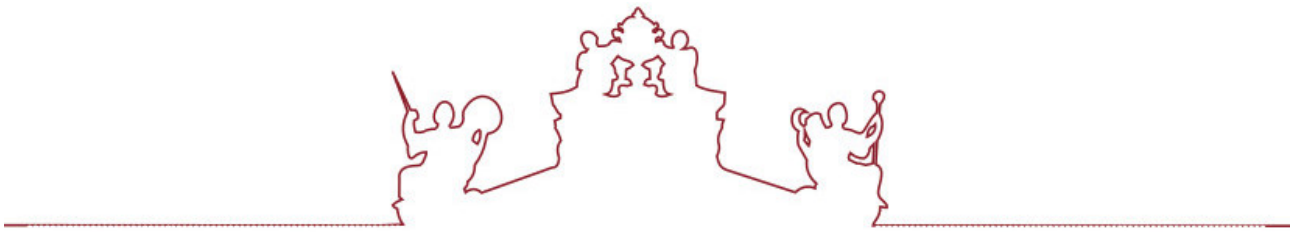

A dissertação foi objeto de apreciação e discussão pública pelo seguinte júri nomeado pelo Diretor do Instituto de Investigação e Formação Avançada:

Presidente	|	Donatella Magri (Università degli Studi di Roma "La Sapienza")
Vogais	|	Eleni Pavlidou (Aristotle University of Thessaloniki) Emanuela Borgia (Università degli Studi di Roma "La Sapienza") Federico di Rita (Università degli Studi di Roma "La Sapienza") Mary Anne Tafuri (Università di Roma La Sapienza) Nicola Schiavon (Universidade de Évora) Panagiotis Spathis (Aristotle University of Thessaloniki)

Évora 2023

Table of Contents

Acknowledgments

First, I would like to thank everyone who contributed to making this project successful. I am deeply grateful to Prof. Marcello Spanu, University of Roma Tre, who is the Spoletino excavation director and the director of the study and publication of pottery from the excavation, for allowing me to study this material. I genuinely thank my thesis supervisor and co-supervisor, Prof. Emanuela Borgia and Prof. Laura Medeghini, for their continuous support of my MA study and research. Their patience, motivation, and in-depth knowledge were invaluable. They assisted me through every step of my project and provided research material and much-needed information. I would also like to sincerely thank Dr. Sara Capriotti for her unconditional support and extensive knowledge of cultural heritage science.

Furthermore, I would like to express my genuine appreciation to Dr. Mara Elefante and Dr. Melania di Fazio for their helpful feedback and practical advice. Finally, I am grateful to the program coordinators, Prof. Nick Schiavon, Prof. Donatella Magri, and Prof. Panagiotis Spathis, for helping me join this program. During this master's, I acquired laboratory training and valuable skills, without which this project could not have come to fruition.

I would also like to mention my friends and colleagues: Pratamanita Widi Rahayu, Medhanit Tamirat, Sotirios Seklos, Ilaeira Maragkou, and Leonidas Aggeletopoulos. I am thankful for their continuous moral support, fruitful discussions, and their honest passion for archaeology and archaeological science. Last, I would like to thank my mother, Panagiota Kretsi, for her encouragement throughout this program.

List of Figures

List of Appendix Figures

List of Tables

Abstract

An integrated analytical approach has been performed to characterize terra sigillata ceramics from the archaeological site of Spoletino (Civitella d'Agliano) in Viterbo, Italy, dated between the 1st and the 4th century AD. This thesis aims to examine the production technologies of the ceramic body and the slip and investigate the features and the provenance of the raw materials. Optical microscopy (OM) and Fourier transform infrared spectroscopy (FTIR) results proved that the ceramic body is composed of quartz, K-feldspar and plagioclase, iron oxides, hematite, mica, biotite, carbonates, calcite, dolomite, diopside, and traces of kaolinite clay minerals in the ceramic body. The firing temperature was estimated at 750–850 °C under controlled oxidizing conditions. The mineralogical composition of the ceramic body is consistent either with the Scoppieto production or sigillata wares from Central Italy. Electron microscopy results coupled with energy dispersive X-ray spectroscopy (SEM-EDS) showed that the slips are more enriched in Al_2O_3, K_2O, and Fe_2O_3 than the matrices, while the matrices are more enriched in CaO. In addition, two samples indicate phosphorous contamination due to post-depositional processes. Results from this study could be utilized to explore trade routes, consumption patterns, and the Roman economy in the middle Tiber Valley.

Keywords: archaeometry; pottery; terra sigillata; Spoletino; Italy.

CHAPTER 1: INTRODUCTION

1.1 The Roman cistern at Spoletino (Civitella d'Agliano)

The archaeological site under study is located at Spoletino, in the municipality of Civitella d'Agliano, in the province of Viterbo. Spoletino is in the middle Tiber Valley, in northeastern Lazio, on the right bank of the Tiber River (Figure 1). Excavations took place as part of a memorandum of understanding signed in 2014, between the Soprintendenza Archeologica, delle Belle Arti e del Paesaggio per l'area metropolitana di Roma, la provincia di Viterbo e l'Etruria Meridionale, the University of Roma Tre and the municipality of Civitella d'Agliano (VT). The excavation director was Prof. Marcello Spanu from the University of Roma Tre, collaborating with Prof. Emanuela Borgia, the University of Sapienza, and the Soprintendenza (Dr. Maria Letizia Arancio) (Mayya, 2019).

Figure 1. Google map of Spoletino

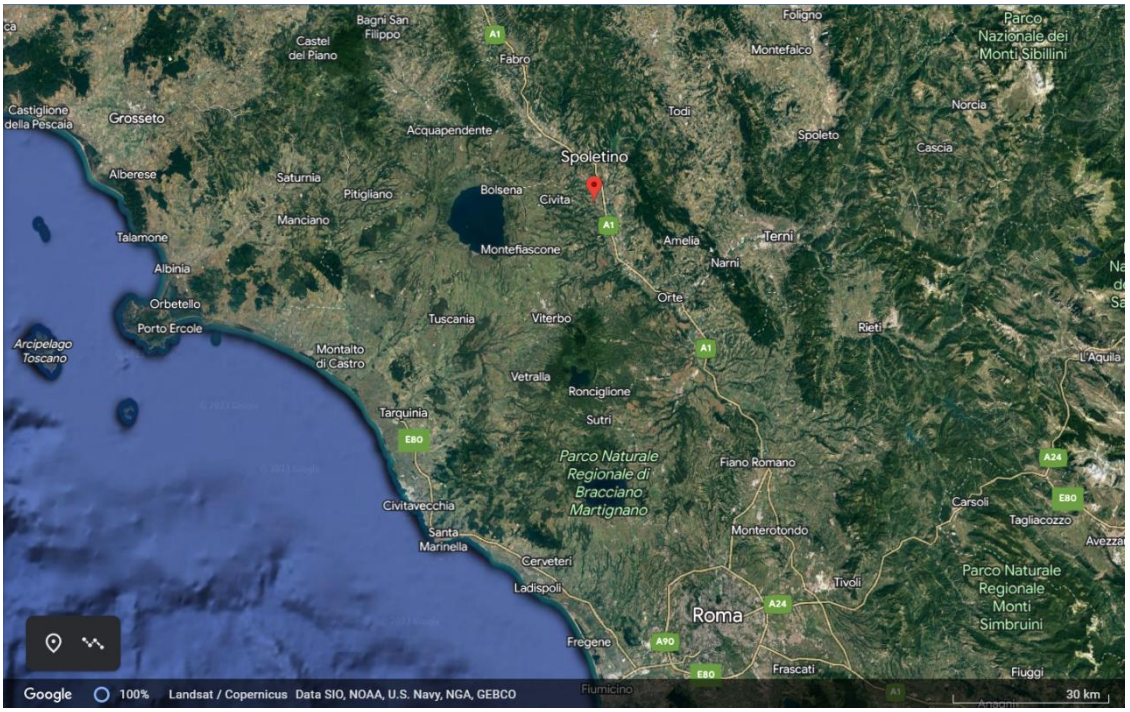

In 2004, an ancient structure had been spotted during agricultural activities in Spoletino, whose architecture and intended use were of archaeological interest. In 2014, during preliminary research, an initial topographic mesh was carried out with a total station. Continuous masonry structures came to light during a prospecting session with a georadar that circumscribed an area of about 40 x 15 m. In the southern sector, remnants of masonry structures, parallel and about 30 cm high, followed a lateral

alignment from east to west (Mayya, 2019).

Figure 2. Aerial photo of Spoletino cistern in 2015. © Spoletino archive, University of Roma Tre.

Excavations from 2014 to 2018 revealed that the structures were pertaining to a Roman cistern with a north-to-south orientation, whose dimensions are 42.10 x 14.20 m. (Figure 2). The cistern had a small staircase in the southwestern corner and a channel to take out the excessive water. The surviving walls were built in *opus signinum* and were 1.20 m high on average. The upper part of the masonry has been destroyed due to recent agricultural works; therefore, it is impossible to estimate the original height. The longer walls were supported by a pair of buttresses on each side. The cistern was largely underground and probably collected rainwater throughout the

year. The structure can be associated with a -not yet uncovered- Roman *villa* in the vicinity, of which only a small bath building had been unearthed about 500 m to the west during a rescue excavation in 1989.

In the mid-1st century AD, a transversal wall, about 0.70 m wide, divided the cistern into two parts (Figure 3). The wall was oriented from east to west and built in *opus caementicium* with facings in small stones. The northern section of the cistern, wider than the other, was filled in intentionally with soil and pottery, forming an extraordinary deposit of materials. Examination of the findings has shown that the materials were deposited in a short period of time, clearly within the middle of the 1st century AD. The cistern was also partially filled with water and mud; these conditions have allowed for an exceptional state of conservation for ceramics, many of which have been recovered whole or reassembled almost entirely (Spanu, 2021).

Figure 3. Plan of the Roman cistern at Spoletino (Spanu, 2021, p. 163, fig. 13).

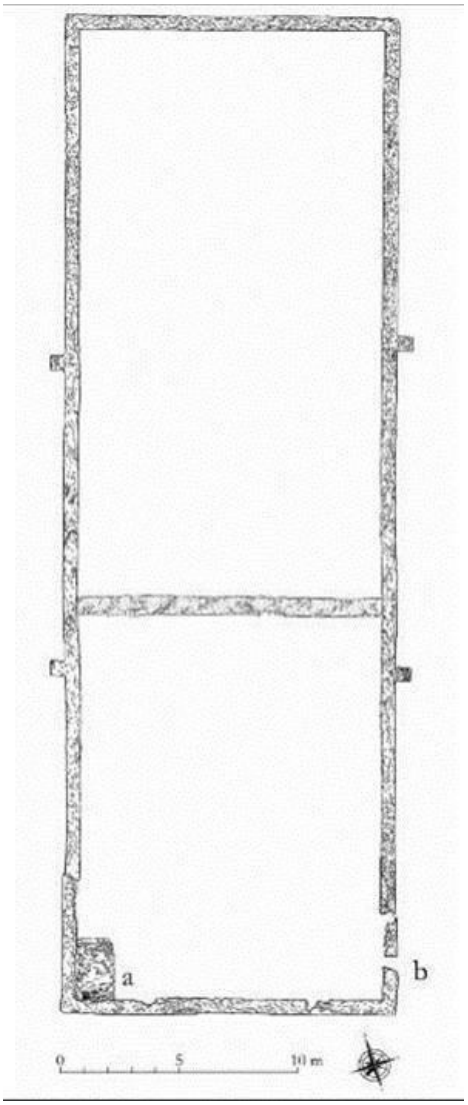

The southern part of the cistern remained in use as water storage until its abandonment at the beginning of the 4th century AD. Building materials (such as bricks, mortar, fragments of frescoes, and other materials) and in-filling of various objects were uncovered in this part and probably belonged to the final destruction phase of the nearby *villa*. The study of materials from the Roman cistern at Spoletino is coordinated by Prof. Emanuela Borgia, University of Sapienza, the director of the pottery laboratory.

The archaeological context offers a comprehensive overview of all types of pottery used in the Roman period, including local and imported productions, which were found through multiple sessions of field surveys. More than 100,000 fragments of pottery have been collected. A considerable percentage comprises *amphorae* attributed to Iberian, Gallic, African, and Aegean productions, along with a consistent percentage of *Spello amphorae* (Spanu, 2021).

In the mid-1st century AD (Neronian) context of the cistern, only Italian Sigillata and one single vessel of Eastern Sigillata B (ESB) have been found. Notably, items from different Italian workshops could be identified: the local middle Tiber Valley ware, terra sigillata from Scoppieto in the Baschi (TR) region, and imported sigillata from Arezzo and Pisa[1]. On the contrary, in the late context (mid-4th century AD), vessels belonging to Italian Sigillata, African red slip ware, and Eastern Sigillata have been identified (Borgia, 2022).

The purpose of this research is to analyze terra sigillata pottery from the Neronian filling of the cistern, as well as one sample from the mid-4th century AD context. Archaeometric analysis can determine the chemical and mineralogical composition of terra sigillata pottery from Spoletino. Through this process, it is possible to assess the production techniques and the firing conditions of Italian terra sigillata and draw conclusions regarding ancient potters' technological expertise. In addition, it can offer insights regarding the provenance of the analyzed pottery fragments, as well as the tangible differences between Italian terra sigillata workshops. Such information can supplement our knowledge of the ancient economy, trade routes, and exchange patterns in the middle Tiber Valley.

[1] Information was acquired by the courtesy of Prof. E. Borgia.

1.2 Geology of Spoletino (Civitella d' Agliano)

Locating pottery production sites based on mineral and rock fragments found in ceramic fabrics requires a knowledge of a region's local geology and topography, which can be obtained from maps and the geological literature. Geologic maps are helpful because they chart major rock formations and chronological units that cover a wide range of lithologies (Whitbread, 1995).

Spoletino is located within the middle Tiber Valley in a cultivated area surrounded by hills. In geological terms, the area is part of the Roman Comagmatic Region, which comprises the main line of volcanoes that extend from Lake Bolsena to the east to Vesuvius and the Phlegrean Fields to the west of Naples (Washington, 1906).

The Roman Comagmatic Region belongs to the Quaternary potassic volcanism of Central Italy, which developed along the Tyrrhenian Sea Margin. Two main magmatic series were distinguished: a potassic KS and a high potassic (HKS) (Nappi et al., 1998). Throughout the Pliocene and Upper Pleistocene, the Tyrrhenian Sea Margin of Latium had marine sedimentary basins resulting from extensional tectonics that formed at the end of the Apennine Orogenic Belt (Figure 4). In the late Lower Pleistocene, a regional uplift caused their gradual emersion, and a broad coastal plain developed due to the nonstop southwest coastline retreat, which turned those marine sedimentary basins into a fertile fluvial valley (Marra et al., 2018). Marine basin emergence shifted the volcano-tectonic processes associated with the uprising of magma through the crust, a fact that led to early, silicic Pliocene volcanism (Barberi et al., 1994b), as well as to the Middle Pleistocene potassium-rich volcanism of the Roman Comagmatic Region (Marra et al., 2019).

The substrate of this fluvial valley is primarily made up of a 200 km-long, 20 km-wide, variably incised volcanic plateau that formed during the middle-Upper Pleistocene because of the volcanic activity of the Roman Comagmatic Region. This substrate developed into a fertile stretch of land, oriented northwest-southeast between the coast and the Apennine Orogenic Belt. It harbors favorable environmental conditions that benefit faunal and human frequentation (Di Buduo et al., 2020).

Figure 4. Paleogeographic map that shows the evolution of the Tyrrhenian Sea margin from Pliocene to Pleistocene (Marra et al., 2018, p. 301, fig. 2).

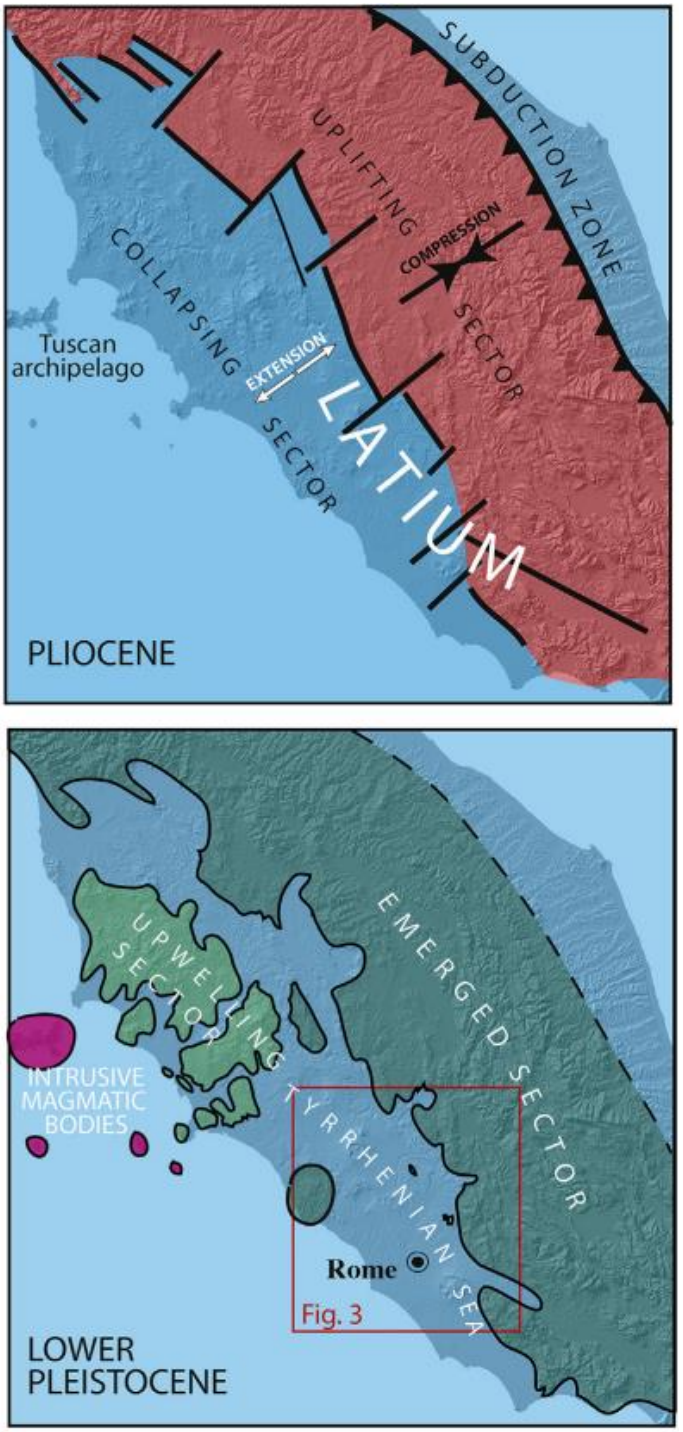

The Vulsini Volcanic District covers the northernmost part of the Roman Comagmatic Region and is spread over 2000 km^2 between Fiora and Tiber Rivers (Southern Tuscany - Northern Lazio). It is located along an averagely N155 °-trending system of grabens (the "Siena-Radicofani Graben" to the west and the "'Tiber Graben" to the east) interrupted by a nearly perpendicular system of faults. Volcanism seems to be significantly influenced by Lower Pliocene extensive tectonics, causing a folded and faulted substrate, primarily comprising Meso-Cenozoic carbonatic, silico-clastic, and pelitic units (Freda et al., 1990).

Three major volcanic complexes form the Vulsini Volcanic District: Bolsena (northeast), Latera (west), and Montefiascone (southeast). According to Varekamp (1979), the Bolsena Volcanic Zone and the Montefiascone Volcanic Zone represent the northern and southern boundaries of the Eastern Vulsini District, respectively. Their volcanism resulted in a complex network of almost 100 individual cones or craters (Freda et al., 1990). Spoletino is located at the eastern margin of the Vulsini District, consisting of a gently sloping volcanic plateau deeply incised by stream valleys (Fig. 5). These stream valleys constitute the hydrographic network of the Tiber River. Elevations vary from > 450 m above sea level along the eastern rim of the Bolsena caldera to < 100 m towards the Tiber Valley (Marra et al., 2019).

The volcanics of the Eastern Vulsini District rely on Upper Miocene - Pleistocene post-orogenic deposits, which outcrop the area's eastern boundary. The underlying sedimentary sequence is the following: Ligurian allochthonous flysch composed of shales, siltstones, and marls, with subordinate sandstone and limestone (Cretaceous-Eocene) and marly-arenaceous series together with thick Mesozoic carbonate sequences of the Tuscan and Umbrian domains (Mesozoic-Cenozoic) (Coltorti et al., 1991).

The Vulsini Volcanic District probably started its activity about 600 ka ago and remained active until 100 ka. Plinian-type activity can be linked to the oldest outcropping products, which resulted in pumice falls and the Civitella d'Agliano Formation, an ignimbrite-forming eruption of the whole District (505 ka). This volcanism can be attributed to the Palaeobolsena volcano, whose prominent explosive eruptions formed the Palaeobolsena caldera. The Paleobolsena caldera is probably located in the northern sector of the present Bolsena Lake. The eruptions in the Bolsena Volcanic Zone occurred between ca. 500 and 250 ka, whereas the activity in the Montefiascone Volcanic Zone ranged between ca. 350 and 200 ka. The activities of the Bolsena Volcanic Zone and Montefiascone Volcanic Zone were contemporary for at least 100 ka between ca. 350 and 250 ka. Surtseyan and sub-lacustrine eruptions within the Bolsena Lake, along with a series of volcanic events in the central Vulsini area, can be traced back to the final activity of the Bolsena caldera. The Bisentina island was formed about 127 ka ago (Nappi et al., 1998).

The widespread effusive activity of the Vulsini volcanics created lava flows and plateaus, resulting in a full array of potassic rock types, like K-basalts (trachybasalts, basanites, and tephrites) and K-foidites (phonolites, trachytes). Trachytes and phonolites are volumetrically prevalent, mainly indicating Plinian pumice-fall and ash–pumice flow deposits from major explosive eruptions (Marra et al., 2019). Dominant marine to brackish sediments, represented by Upper Pliocene–Lower Calabrian clays and sandy- clays, and Upper Calabrian clayey-sands with polygenic conglomerates, outcrop extensively in the Eastern Vulsini District (Nappi et al., 1998).

We should mention that the interaction between volcanism, tectonics, and glacio-eustasy propelled the geologic evolution of the Eastern Vulsini District. During the Middle and Upper Pleistocene, the sedimentary successions deposited by the Tiber River and its tributaries in fluvial and lacustrine environments were interposed with volcanic products, for the most part, pyroclastic-flow and air-fall deposits (Marra et al., 2019). When sea level fell, erosion occurred, while deposition occurred during sea level rise, filling formerly excavated incisions. However, this process was influenced by volcanic eruptions, which laid out large volumes of pyroclastic deposits and fault displacement (Luberti et al., 2017).

A study by Mara et al. (2019) has mapped a flight of 5 paleo-surfaces in Civitella d'Agliano at the top of terraced deposits, which include primary volcanic and sedimentary successions that six new $^{40}Ar/^{39}Ar$ dates have geochronologically set. The area is distinguished by a volcano-sedimentary succession related to the Paleovulsini and Bolsena-Orvieto complexes, which rest upon mainly marine silty clays deposited in the Paglia-Tiber Graben from the late Zanclean up to the Santernian or Sicilian (Figure 5).

The difference between the top of the marine deposits and the base of the volcano-sedimentary succession largely reduces in elevation from west to east towards the Tiber River valley. The Bolsena-Orvieto deposits are partially interposed with alluvial sequences caused by the combined glacio-eustatic and tectonic activity. The volcano-sedimentary succession is the following: primary (dominant fall deposits and pyroclastic flows), secondary volcanic deposits (occasionally carrying remains of vertebrates), and subordinate lava flows and rare diatomaceous layers, separated by paleosoils that alternate with the alluvial sequences. These successions are generally fining upward with gravel and sand at the base, accompanied by sandy-silt and silty

clay deposits and continental carbonates (travertines and calcareous tufa) in the upper part. Mainly gravelly-sandy, epiclastic volcanic lenticular layers are often interbedded with the fluvial-lacustrine deposits (Marra et al., 2019).

Figure 5. Geologic map of the surroundings of the archaeological site. $^{40}Ar/^{39}Ar$ dates on tephra layers interbedded within sedimentary successions allowed a close association with the glacio-eustatic cycles encompassing Marine Isotope Stage (MIS) 19 through MIS 5. 1) Recent alluvial deposits of the Tiber River and its hydrographic network. Terraced deposits: 2) MIS 5 Fluvial-lacustrine succession; 4) MIS 7 fluvial lacustrine (a) and travertine (b) deposits; 5) MIS 9 fluvial lacustrine (a) and travertine (b) deposits. Volcanic deposits: 3) Tufo Rosso a Scorie Nere Vicano; 6) Orvieto-Bagnoregio pyroclastic succession; 7) Orvieto-Bagnoregio lava flows; 8) Paleovulsini pyroclastic succession; 9) Plio-Pleistocene marine clay and sand. 10) Inferred structural lineaments (Marra et al., 2019, p. 2, fig. 1).

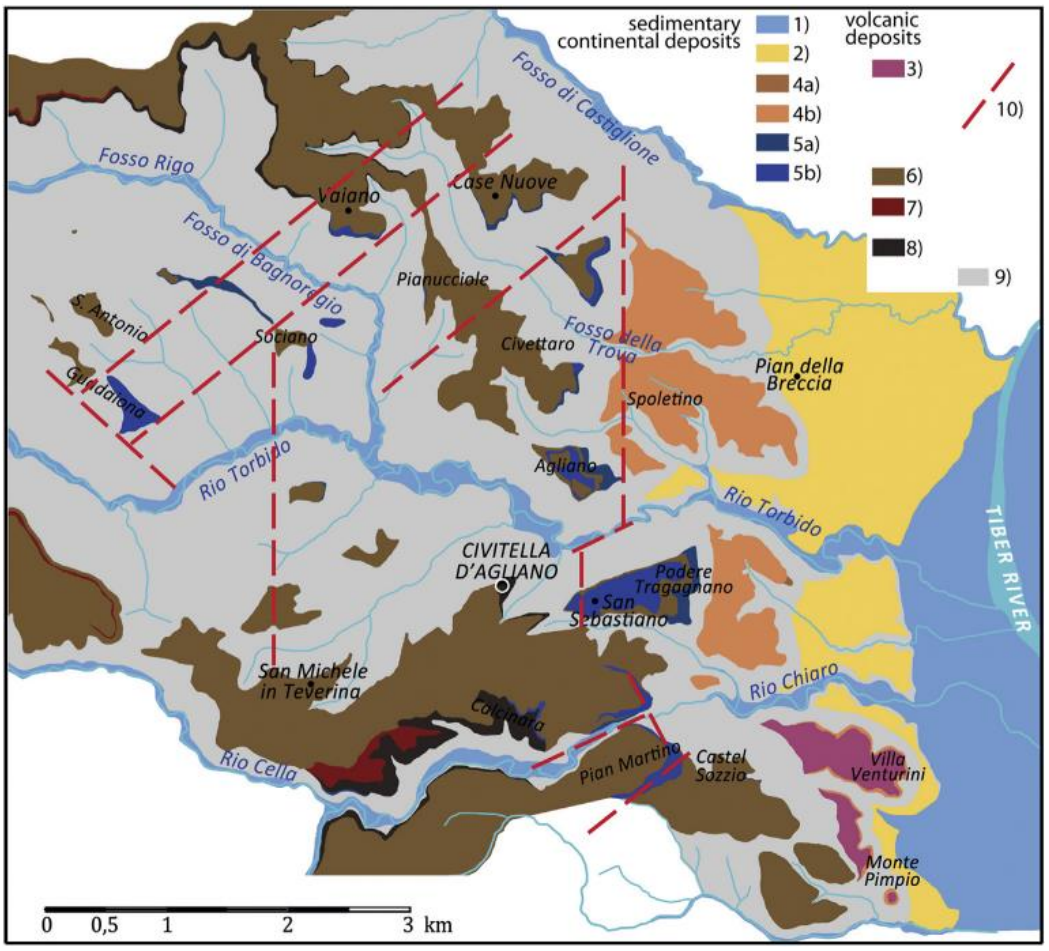

1.3 Pottery as an archaeological material

Archaeological ceramics are clay inorganic artifacts that were produced by past societies. They consist of some of the earliest synthetic materials intentionally crafted by humans, such as pottery, figurines, ceramic building materials, refractories, and many other items. They are widespread throughout the archaeological record due to their everyday use by ancient civilizations and their usually good state of preservation (Quinn, 2022).

The term ceramics stems from the Greek "keramos," which means "potter's clay" or "pottery." Its original Sanskrit meaning is "to burn." Therefore, it originally referred to products crafted by heating clay (Carter & Norton, 2007). In archaeological literature, there is a distinction between high-fired, vitrified, and usually glazed ceramics and common pottery, which consists of low-fired, unvitrified artifacts, cooking, and storage vessels. This distinction may be even more specific regarding glazed and vitrified ceramics that belong to a technologically intermediate level between low-fired pottery and high-fired translucent porcelain (Rice, 2015).

Pottery and ceramics are organized into "wares" based on their composition, firing, and surface treatment. Rice (2015) attempts a classification into terracottas, earthenwares, stonewares, and porcelains based on production technology (Table 1). Terracottas are relatively coarse, porous wares fired at low temperatures, usually 900 °C or less. They are typically not covered with a glaze but may undergo several surface treatments. Surfaces may be covered with slip or engobe, a liquid solution of fine clays and water that lowers the vessel porosity and permeability.

Earthenwares may incorporate porous, unvitrified clay bodies, but they are fired at a wide range of temperatures from 800/900 °C to 1100/1200 °C. They include products ranging from coarse (like bricks and tiles) to fine earthenwares. Stonewares are fired at temperatures of approximately 1200 to 1350 °C. Vitrification or partial fusion of the clay body is usually achieved, depending on the chemical composition. They may be unglazed or have a lead glaze or, in modern times, a salt glaze (Rice, 2015).

Even if it was not produced in the Roman period, which is the object of this work, it is worth mentioning porcelain, a thin, white, translucent vitrified ceramic fired at a temperature range from 1280 to 1400 °C or higher. Porcelain undergoes a profound transformation of materials in the initial paste due to extended firing at high

temperatures (Velde & Druc, 1999). Porcelains consist of kaolin clay, usually without impurities, mixed with quartz and ground feldspathic rock that acts as a flux. At high temperatures, the feldspar melts, causing the final product to be translucent and hard and exhibiting a melodious ring when tapped (Rice, 2015).

Pottery studies are an integral part of modern archaeology. Ceramics can be used to hypothesize about intangible aspects of past cultures, such as cultural identities, traditions, and beliefs. They are also a valuable tool in accurately dating archaeological sites (especially when evidence for absolute chronology is lacking). They can also be utilized in various research projects, including studying ritual activities, trade routes, cultural interaction between social groups, craftsmanship, and production organization or "chaîne opératoire" (Roux, 2017; Quinn, 2013).

Table 1. Ceramic Bodies and Their Characteristics (Rice, 2015, p. 5, t. 1.2)

Body Type	Porosity	Firing Range	Comment
Terra-cotta	High: 30% or more	Well below 1000 °C	Unglazed, coarse, and porous; often red-firing
Earthenware	Usually 10%–25%	900–1200 °C	Glazed or unglazed; body non-vitrified
Stoneware	0.5%–2.0%	1200–1350 °C	Glazed or unglazed; vitrified body
China	Low: usually less than 1%	1100–1200 °C	White, vitrified
Porcelain	Less than 1 %. Often nearly 0%	1300–1450 °C	Hard body; fine, white, translucent; "rings" when tapped

1.4 Italian terra sigillata: A Brief Introduction

Terra sigillata is the most important and influential fine ware of the Roman period. These vessels are characterized by a purified clay, whose color can range from beige to pink and orange to red, covered with a shiny red slip, and they are reserved for tableware. Tableware includes vessels, such as bowls, dishes, serving trays, cups, and jugs for serving and food consumption (Bes, 2015b).

Before firing, the clay body was immersed in a refined, liquid clay solution (slip) covering the vessel's surface. The slip covered the interior and exterior of the pots and made them impermeable (however, in a few cases, some portions of the vessel, such as the outer foot, were not slipped). This feature appealed to users and made terra sigillata especially suitable for serving (semi-)liquids (Van Oyen, 2016).

The term “Terra sigillata” was first used to indicate vessels decorated with relief motifs, called “sigilla” (meaning small figure), indicating the small decorations on the ceramic surface (Oswald & Pryce, 1920). Nevertheless, the term was used afterward to describe relief-decorated products and wheel-made plain vessels (the majority) with a shining, bright red slip (Bonfante et al., 2015).

Terra sigillata is a modern Latin term translated as “sealed earth,” it was devised by scholars working on Roman sites in Germany, France, and Britain. Gaulish terra sigillata had formerly been called “Samian Ware” based on a mistaken attribution in Pliny, while Italian sigillata was called “Arretine” after the first well-known production center of Arezzo. Today, the term “terra sigillata” refers to both Arretine and Samian wares (Van Oyen, 2016), but it can also be called Red Slip Ware.

For the purpose of this thesis, we will focus primarily on undecorated Italian terra sigillata. The starting points of reference for Italian terra sigillata in archaeology were the studies published by Dragendorff (1895) and Loeschcke (1909). Dragendorff (1895) introduced the first classification system for terra sigillata, using type numbers based on the varying forms of the vessels. He relied on recorded specimens from cemeteries (where coins are usually found) and on historically dated sites. Loeschcke (1909) classified the shapes of the Italian terra sigillata plain wares found at the Roman army camp of Haltern on the Lippe River. He divided his terra sigillata

typology into four “services” with distinctive rim morphology.

Two central reference works have been vital for this study in recent years. The forms of vessels in this thesis are classified according to the volume by Elisabeth Ettlinger (1990), *Conspectus formarum terrae sigillatae Italico modo confectae*, which contains forms of Italian-type terra sigillata, primarily the plain undecorated wares. The collection of terra sigillata stamps known as *Corpus Vasorum Arretinorum*, in its second edition, summarizes the work of August Oxé, Howard Comfort, and the editor of the second edition, Philip Kenrick (2000) (abbreviated OCK). This volume covers tens of thousands of potter stamps on terra sigillata items, of which 4.611 were found in Etruria.

Stone (2015) defines Early Italian terra sigillata as the fine red-gloss ware produced in Italy between ca. 20 BC and ca. 50/75 AD. Production of the ware probably began around 40-30 BC at Arretium (modern Arezzo) in northern Tuscany, where Italian black gloss pottery had previously been produced (Hayes, 1997, 41). Early Italian terra sigillata enjoyed immediate commercial success and quickly conquered markets throughout the Roman world and beyond, as fragments have been located in Britain, Scandinavia, India, and the Arabian Peninsula. The Italian production centers accomplished a significant homogeneity of fabric and slip, so much so that it is sometimes impossible to distinguish the origin of individual Italian terra sigillata vessels by visual examination only. Chemical analysis can provide a high degree of certainty for identifying specific workshops (Ettlinger, 1990, 1–2, 27–35; Hayes, 2008, 42–45; Stone, 2015, 209).

The Augustan and Tiberian periods were the peak of Italian sigillata production. Italy and the Western Mediterranean constituted the major markets with significant exports to the East. During this period, several high-quality vessels have been attributed to various workshops. Italian workshops provided pottery even in the most remote places of the Roman Empire, as high-ranking officials of the Roman troops would use terra sigillata pottery. Soon enough, other workshops started to emerge in Roman provinces to establish production centers closer to the main ports and to reduce transportation costs to Gallic and other provincial markets. By 10 AD, Italian workshops had lost a part of the Gallic and German markets to northern workshops, while in the Eastern Mediterranean, a group of wares imitating Italian terra sigillata shapes circulated after the first quarter of the 1st century AD (Stone, 2015, 209–210; Rizzo, 1998, 801–2; Tol

et al., 2021, 204).

According to Bes (2015b, 64–6), during the late Augustan-Tiberian period, the morphological influence of Early Italian Sigillata on Eastern Sigillata A is highly problematic, and it is not merely an imitation of Early Italian sigillata shapes by Eastern sigillata wares. He suggests that the inspiration for both Early Italian Sigillata and Eastern Sigillata A derives from metal prototypes. Society's elite used gold and silver vessels, so he proposed that terra sigillata forms would imitate metallic vessels to appeal to prospective buyers.

Eastern Sigillata B also shows remarkable influences by Italian Sigillata, based on morphological similarities, potter stamps, and trade routes. In the Middle Augustan period, Italian workshop owners such as Caius Sentius from Arezzo and Quintus Pompeius Serenus from Pozzuoli established subsidiary factories around Tralles and perhaps at Ephesos. Italian workshops may have been responsible for the launch of production of Eastern Sigillata B ware (Lund, 2003, 132).

Italian sigillata continued to be vastly popular in Italy and the Mediterranean during the late 1st century AD. Afterward, it progressively lost its share of the fine ware market to products from the Eastern Mediterranean and North Africa. The ware ceased to be produced altogether after the mid-2nd century AD. A notable shred from Cosa with the impression of a coin illustrating Hadrian's wife, empress Sabina, can be considered a terminus *post quem* of absolute chronology in the 140s AD for decorated Late Italian Sigillata (Hayes, 1997, 52; Moevs, 2006, 167–8; Tol et al., 2021, 204).

Quantified results from excavations at the Nuotatore's baths in Ostia show that between 70 and 100 AD, Italian sigillata prevails with c.80%, while South Gaulish is c.10%, and African is below 5%. Between 120 and 140 AD, Italian sigillata represented c.70%, South Gaulish c.10%, Hispanic less than 5%, and African c.20%. Between 160 and 190 AD, Italian decreases to 10–20%, South Gaulish and Hispanic are below 5%, while African sigillata is most found at 70% (Carandini & Panella, 1978; Quaresma, 2013, 388). North African sigillata became widely diffused after the mid-2nd century AD and remained in circulation in the Eastern Mediterranean until the 6th century and the second half of the 7th century AD (Constantinople, Aegean Sea, Black Sea, Cyprus, Near East). During the 4th and 5th centuries AD, the ware inspired a series of regional imitations in the Roman Empire, mainly in the Iberian Peninsula, Italy, and Egypt (Ballet et al., 2012, 87, 96; Bonifay, 2014, 81–83).

Italian terra sigillata predominantly bears stamps, which are marks pressed on the vessels during the production process. They were impressed after or during molding before the vessels were fired. This stamping tradition can be traced back to the emergence of the ware, and stamps contained either a name or a graphic symbol. The producer's name could be a longer or shorter version of a single person's name, indicating the *gens* (clan) or the *prenomen* of a slave (or freedman). In the case of short hands, the full names are assumptions based on other stamps with more extended versions of the names in a similar context or appearing on identical pots (Kiiskinen, 2013).

Pre-Augustan stamps are square in outline, applied radially on the vessel's floor (usually four or five times), and bear monograms composed of two or more letters. In a second phase, a single centrally placed stamp expanded into a larger rectangle, allowing space for two lines of text with the producer's name (sometimes along with the worker's name). During the middle and late Augustan period, other shapes of stamps appeared, where the name (or graphic symbol) was placed within a circular or rectangular frame. In the post-Augustan period, the most common stamp was in the shape of a footprint or "*planta pedis,"* and many Italian terra sigillata workshops adopted it. In late Italian workshops, we also find a crescent-shaped stamp (Ettlinger, 1990, 147–148). It is worthy of note that rectangular stamps continued to exist after the *planta pedis* stamp became the norm (Hayes, 2008).

There are many interpretations as to why terra sigillata was stamped. Stamps could indicate the kiln owner or the ceramic workshop, and they could identify items made within a specific contract. In addition, they could offer helpful information for the organization of production and sale, and they could also serve promotional purposes (Fülle, 1997). The production of Italian terra sigillata is highly standardized; therefore, it is commonly used for accurate dating and provenance based on form, decoration, and stamps. Sigillata typology allows researchers to map production, distribution, and consumption patterns and address problems concerning trade and the Roman economy (Van Oyen, 2015a).

Italian production centers were established during the last two decades BC in Campania, in northern Tuscany (the city of Pisa and its surroundings), in the Po Valley, Aquileia, and Central Italy, around Rome (Ettlinger, 1990; Sciau et al., 2020). "Classic" terra sigillata from Arezzo has a hard, smooth-textured orange-brown

(2.5YR 5/8) fabric with a conchoidal fracture. The slip is usually bright, glossy red (10R 4/8), and the matrix is homogeneous, including only a few white flecks (< 0.1 mm) and occasional voids. It can be dated from about 30 BC to the middle of the 1st century AD. Most arretine potters made mainly plain ware, and forms 1-37 from *Conspectus* are represented in their work (Ettlinger, 1990, 6, 52–166; Tyers, 1996, 111–2; see also Munsell Color Company, 1975).

Many workshops have been excavated under the medieval city of Arezzo during the 19th century AD. Some have come to light at Ponte a Buriano near the river Arno, where the potter C. Tellius was active. At Cincelli, 10 km from Arezzo, stamps of C. Cispius, P. Cornelius, and C. Tellius were detected, mostly on relief decorated ware. Sigillata production was widespread, as potters like Rasinus and M. Perennius seem to employ sixty and twenty slaves, respectively (Peacock, 1982, 115–122). Gnaeus Ateius was another significant producer at Arezzo, Pisa, and Val di Fine. He can also be linked to Gaulish productions, as stamps bearing his name were used in Lyon and La Graufesenque (Kiiskinen, 2013, 26–7). Excavations at Bolsena published by Goudineau (1968) provide a comparative typology of vessels from the beginnings of terra sigillata production into the third quarter of the 1st century AD, as all terra sigillata found there was made at Arezzo (Stone, 2015, 213).

After 75 AD, the main export center was the region of Pisa, where Late Italian Sigillata was produced until the mid-second century AD (Hayes, 1997, 52). Late Italian Sigillata was manufactured in the tradition of Arretine potters, but it is of poorer quality, and its repertoire is considerably reduced. Plain vessels that are more frequent are of forms *Consp*. 3, 20, and 34. Decorated vessels adopt the form Dragendorff 29 exclusively, while stamps are mostly in *planta pedis*. Late Italian Sigillata was produced in the broader area of central Italy, including the middle Tiber Valley and Campania, mainly at Pozzuoli. It was mostly distributed to Western Mediterranean markets but also reached some main cities in the East (Ettlinger, 1990, 13–6). L. Rasinius Pisanus, Sex. Murrius Festus, Sex. Murrius Pi(sanus ?) and Sex. Murrius Cl(adus) are some of the principal potters' names associated with this period (Pucci, 1980, 140).

Terra sigillata from Po Valley productions has been attested throughout the Po Valley and in Noricum, Pannonia, Moesia, Dalmatia, Aquileia, and Emona. Magdalensberg in Carinthia has yielded significant findings, which can be approximately dated from the

early 1st century until the middle of the 2nd century AD. In Magdalensberg, the ware could be differentiated from sigillata from Arezzo due to its altered proportions and blurred profile lines. However, past the middle of the 1st century AD, the forms copied much more successfully the arretine repertoire, especially in the case of the most well-known workshop of L. Mag ( ) Vir ( ) (Ettlinger, 1990, 8–10; OCK 1085).

In central Italy, workshops positively identified are Arezzo, Pisa (via S. Zeno and via S. Stefano), Poggio Fiori (Livorno), Isola di Migliarino (Pisa), Torrita di Siena (Siena), Marzuolo (Grosseto), Sesta (Siena), San Cassiano (Perugia), Scoppieto (Terni), Vasanello (Viterbo), Prima Porta (Rome). San Cassiano and Scoppieto, although isolated, had a strategic geographical position due to the proximity of the Tiber, which was navigable down to Rome (Figure 6). Rome consumed many of the Scoppieto products and those of the central Tiber Valley in general (Sternini, 2016, 2019).

The most important pottery workshop for this study is Scoppieto, located in the municipality of Baschi (TR) on the left bank of the Tiber River (Figure 7). The start of production can be placed in the Augustan period, with a subsequent phase in the second half of the 1st century AD. The workshop was abandoned at the end of the 1st/start of the 2nd century AD during the reign of Trajan. The sigillata repertoire in Scoppieto adopts common types of Italian productions with some local variations. The ceramic body is a hard, smooth-textured pink (2.5YR8/4, 5YR7/4, 5YR8/4, 7.5YR8/3, 7.5YR8/4) or light red (2.5YR6/8, 2.5YR7/6, 2.5YR7/8) fabric with conchoidal fracture. The slip is smooth, mostly opaque, or semi-glossy in shades of orange and red (Bergamini, 2016; see also Munsell Color Company, 1994).

Stamps of at least 95 potters have been found, but 48 are anepigraphic and challenging to interpret. Most of the potters probably worked as independent craftsmen who shared common facilities, many of whom were members of the *gens* Plotidia (Bergamini, 2013). Some of the best-represented potters are L. Plotidius Porsilius, L. Plotidius, and L. Plotidius Zosimus in the first half of the 1st century AD, and P. Avillius Gl ( ) in the second half (Bergamini, 2016). Three sampled items from this thesis have been attributed to the Scoppieto manufacture, as they bear stamps in *planta pedis* of L. Plotidius Zosimus (OCK 1488).

Figure 6. Production centers within the river network between the Arno and Tiber valleys (Sternini, 2019, p. 490, fig. 1).

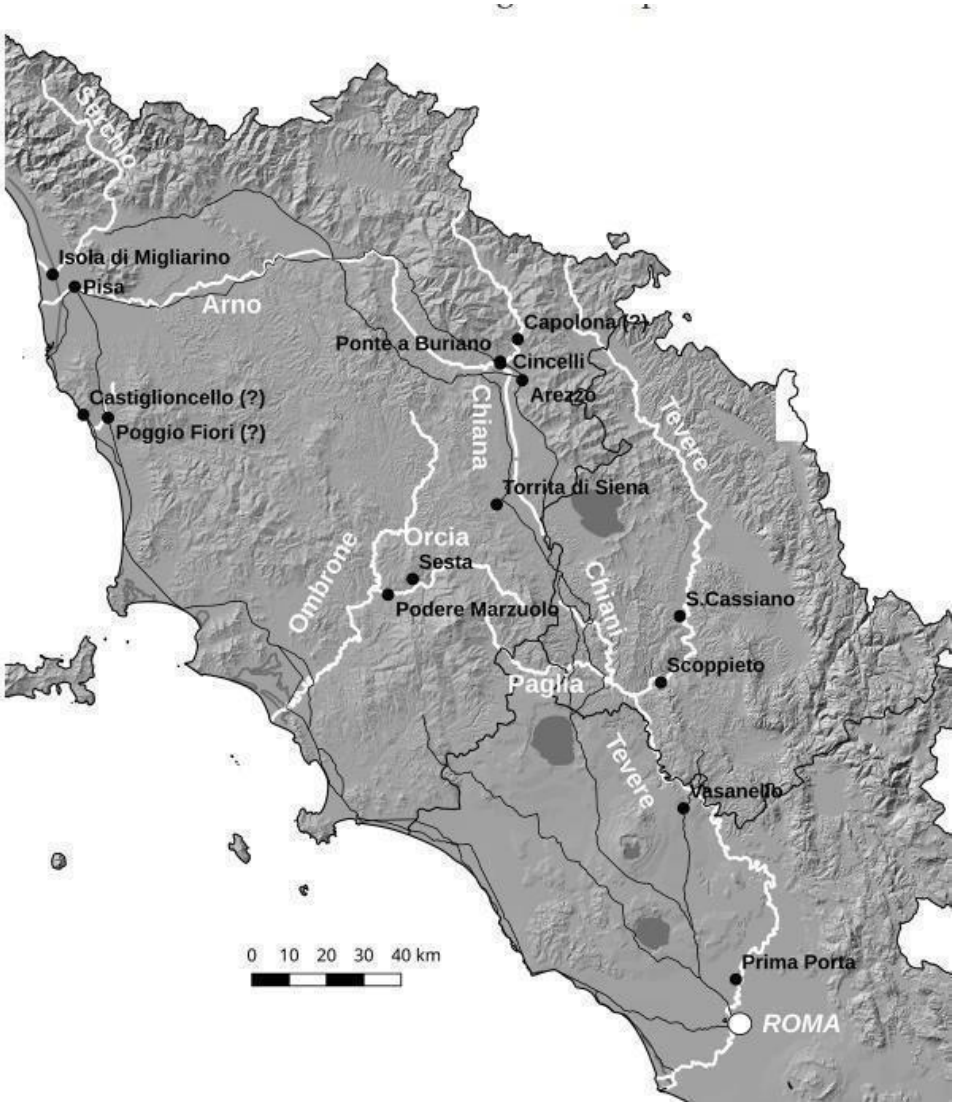

Poinçons and molds were also uncovered that, according to chemical analyses, were not manufactured locally. Some poinçons could have been made in other Italian workshops, while others probably come from Arezzo. As for the molds, out of 18 pieces, eight are locally made, while nine come from Arezzo - one is of uncertain origin (Bergamini, 2016). Among those from Arezzo, some are signed by C. Titius Nepos, whose plain vessels date back to the last two decades of the 1st century AD, while others are signed by M. Perennius Crescens, who was probably active from 30 AD until 60 AD (Bergamini, 2014; Bergamini & Thirion-Merle, 2003). Olcese (2004) notes two samples found in Rome that are stamped by L. Plotidius Zosimus (OCK 1488.7) and L. Plotidius Por( ) L. Plo(tius) Z(osimus) (OCK 1487.2). They seem not

to belong to the Scoppieto production but the so-called “OctPro-OctSal” group, whose chemical composition is similar to that of Scoppieto potters. This group was active in the first half of the 2nd century AD and could originate near Rome, in Etruria, or Umbria (Rizzo, 1998, 832).

There was a gradual increase in ceramic production at Scoppieto from the Tiberian-Claudian to the Neronian-Flavian period. It was not limited to terra sigillata but included common pottery, thin-walled cups, and lamps (Bergamini, 2007, 2015). Specifically, terra sigillata of Scoppieto origin has been found in Rome and all over Italy, Gaul, Germany, and North Africa. However, adjacent areas in the middle and upper Tiber Valley have not yielded many similar findings (as in the case of Spoletino). It should be noted that between the reign of Domitian and Trajan, when the workshop was finally abandoned, the amount and quality of sigillata production progressively declined (Bergamini, 2016).

Figure 7. Terra sigillata, lamps, and tools from Scoppieto (Bergamini, 2013, p. 73, fig. 3.1).

In Campania, there was a long-standing tradition of black gloss wares that imitated metallic vessels. The black gloss “Campanian” ware was traded and widely copied in the western Mediterranean in the last three centuries BC, just as terra sigillata was in the first three centuries AD (Peacock, 1982, 115–6).

Terra sigillata workshops can be traced in Pozzuoli, Cales, and Cumae (Figure 8). Campanian sigillata has been documented in small quantities in Berenice, Odoba, and

Haltern (Ettlinger, 1990, 11–3). Other locations where Campanian sigillata has been found are Sicily (Iaitas, Morgantina), Pompei, Ordona (Puglia), and North Africa (Berenice, Sabatha). The ware has a soft orange fabric, and it was initially called "Tripolitanian" by P. Kenrick because he believed it was manufactured in North Africa. However, archaeometric studies showed that it originated from the Bay of Naples. The beginning of its production can be traced to the middle of the 1st century BC, as findings from excavations in Pompei have been dated to around 40 BC. Its end could probably be placed in the third quarter of the 1st century AD. Potter stamps in Greek and Latin letters further support a Campanian origin of the ware (Soricelli, 1994, 2004).

The most essential workshop seems to be that of L. Pullius Caprus, who employed at least two workers, Demetrius and Tertius. Stamps in *planta pedis* are rare, but the repertoire follows that of most common forms of Italian terra sigillata with some regional variations. In this case, for form identification, reference is made to the typology drawn by Kenrick (1985) on "Production A" specimens found in Berenice (Assenti, 2018). Stone (2015, 224) prefers the term proposed by Kendrick, "Campanian Orange Sigillata," to characterize "Tripolitanian" or "Production A" ware. Campanian Orange Sigillata appears to have been exported to southern Italy, Sicily, and North Africa in the late 1st century BC and throughout the 1st century AD. The raw materials used for these products differ from the black gloss "Campanian Ware," either because potters employed different techniques or used other clay sources.

Sigillata from Cales has been found in Pompei, Rome, Ordona, and Spain (Tarragona, Ampurias). The beginning of Calenian production could be dated to the middle of the 1st century BC when it coexisted with black gloss wares. The fabric of Calenian sigillata shares some characteristics with those previous and contemporary black-gloss wares. If made with calcareous clay, the fabric varies in color from beige to pink (5 YR 6/6-5 YR 7/6), and it is compact, with mica and sometimes calcareous inclusions. The slip is generally thick, homogeneous, glossy orange-red/brick red (2.5 YR 4/8-5/8). The typology is closely related to Italian sigillata but borrows elements from sigillata productions at the Bay of Naples. Well-known potter stamps in Cales include those of Antiochus, Calad ( ), Pamphilus, and Secundus, with the most important workshop being that of M. Lollius (Pedroni & Soricelli, 1996; Soricelli, 2004; see also Munsell Color Company, 1975).

The production in Pozzuoli can be dated from 15–10 BC into the third quarter of the 1st century AD (Ettlinger, 1990, 11–2). It mainly involves plain ware, the shapes of which were the same as in the Arezzo repertoire, apart from some local variations in forms *Consp*. 22 and 31. Potter stamps were generally round, with the name horizontally placed within a garland. Puteolan sigillata is circulated in small amounts in Pompei, Sicily, Apulia (Ordona), Berenice, and the Iberian Peninsula (Assenti, 2018; Soricelli, 2004).

Figure 8. Known production sites of Italian and Gaulish terra sigillata (Kiiskinen, 2013, p. 32, fig. 1.3).

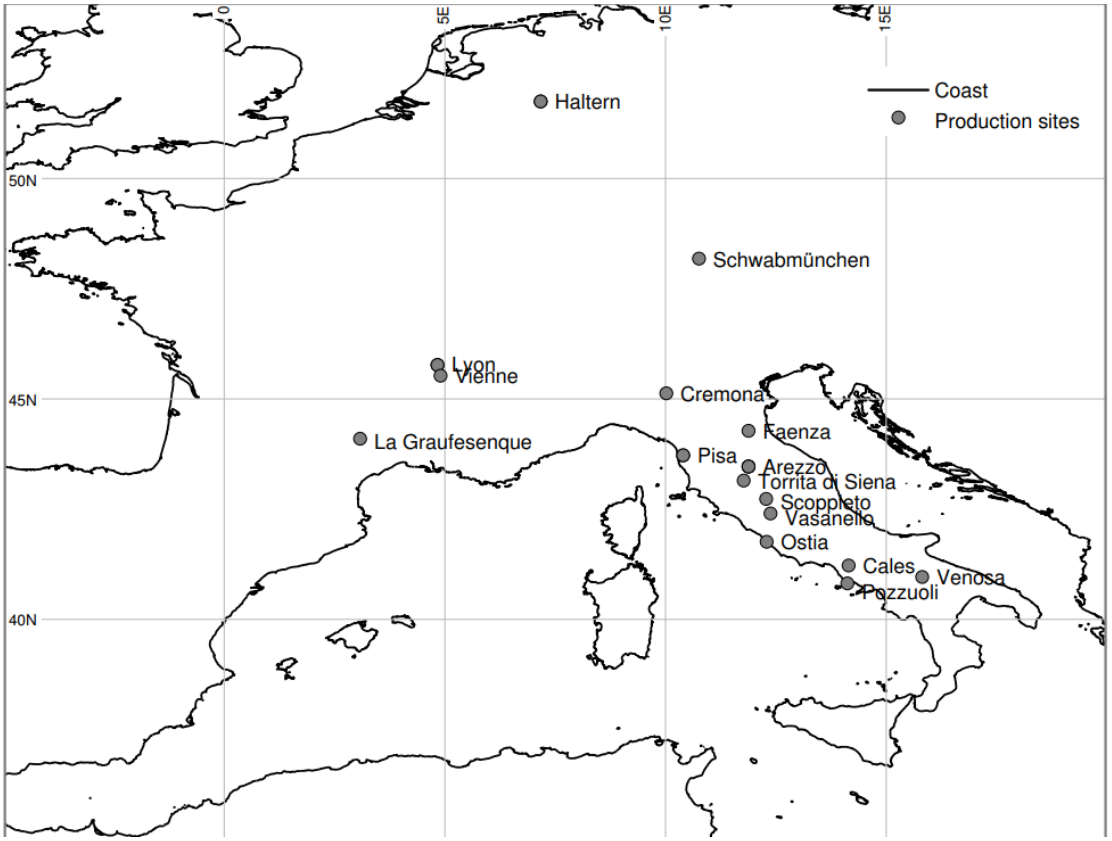

The following observations can be drawn regarding the forms from Conspectus that some of the sampled items in this study are attributed to. *Consp*. 3 (Figure 9) is a dish with a sloping wall and bead rim. Along with the bowl *Consp*. 34, it is one of the most long-lasting shapes in the Italian sigillata repertoire, dated from the first half of the 1st century AD to the 2nd century AD. It was produced in Etruria, Campania, and the Po Valley and distributed throughout Italy (Ettlinger, 1990, 56). In early examples of *Consp*. 3 the wall is steep and short, slightly convex in profile. The floor usually bears a band of rouletting between grooves; the rim is thickened or everted, often with a flat top, and regularly marked off by fine grooves. The standard version of *Consp*. 3 was

established during the Flavian period, when the wall was straighter but less steep, usually with a small, everted rim. The proportions are deeper, the floor has a smaller diameter, and the rouletting on it disappears (Kendrick, 1985, 180).

Figure 9. *Conspectus* Form 3 (Ettlinger, 1990, p. 57, fig. 3.1.1).

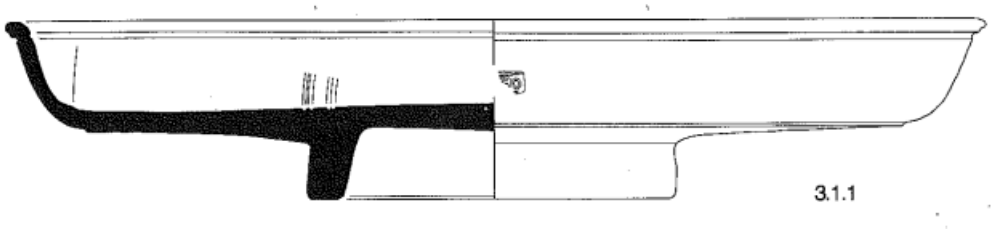

Consp. 27 (Figure 10) is a cup with a small flat lip and the occasional rouletting on top of it. The wall is usually straight and slopes outwards. It can be dated to the Tiberian-Neronian period, and it was produced in central and northern Italy (Ettlinger, 1990, 100).

Figure 10. *Conspectus* Form 27 (Ettlinger, 1990, p. 101, fig. 27.1.1).

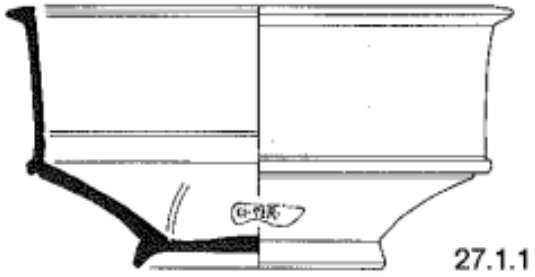

Consp. 32 (Figure 11) is a bowl with a restricted wall and variously articulated rim. Sub-from 32.2 is attested in the Po valley and is somewhat coarser, without spiral decoration. It can be placed in the 1st century AD (Ettlinger, 1990, 108).

Figure 11. *Conspectus* Form 32.2 (Ettlinger, 1990, p. 109, fig. 32.2.1).

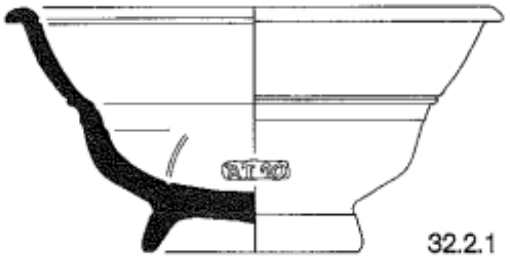

Consp. 33 (Figure 12) is a hemispherical bowl with a narrow flange on the wall. It was produced in Etruria and Campania from the 1st to the early 2nd century AD (Ettlinger, 1990, 110).

Figure 12. *Conspectus* Form 33 (Ettlinger, 1990, p. 111, fig. 33.3.1).

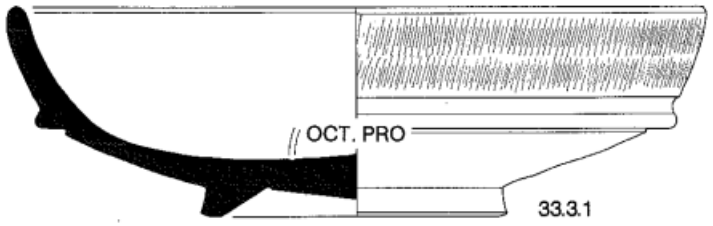

Consp. 34 (Figure 13) is a hemispherical bowl with a vertical rim and pronounced flange on the wall. It was prevalent from the late Tiberian to the Flavian period and can be associated with Etrurian, Late Italian, and Po Valley productions (Ettlinger, 1990, 112).

Figure 13. *Conspectus* Form 34 (Ettlinger, 1990, p. 113, fig. 34.1.1).

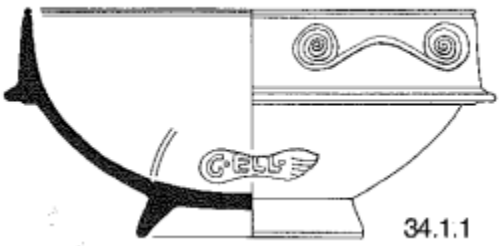

Consp. 36 (Figure 14) is a hemispherical bowl that encapsulates many sub-forms, which can be placed from the early Augustan era to the end of the 1st century AD. *Consp*. 36.4 is mainly stamped in *planta pedis*, and its known production centers are in Etruria and the Po Valley (Ettlinger, 1990, 114).

Figure 14. *Conspectus* Form 36 (Ettlinger, 1990, p. 115, fig. 36.4.3).

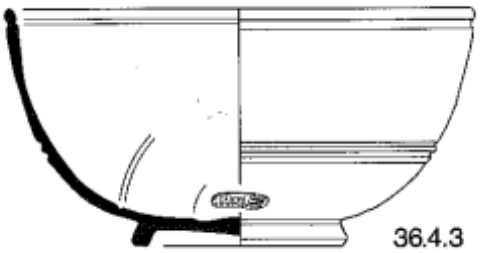

Consp. 39 (Figure 15) is a dish with a curving wall and drooping rim, which can be traced to late Po Valley productions and, more rarely, to the Late Italian ones. It is dated from the second half of the 1st century to the first half of the 2nd century AD (Ettlinger, 1990, 120).

Figure 15. *Conspectus* Form 39 (Ettlinger, 1990, p. 121, fig. 39.1.2).

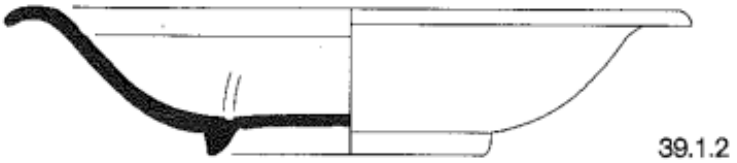

1.5 Review of pottery studies and archaeological science

Scientific literature and archaeometric studies provide insights regarding Italian terra sigillata manufacturing technology. The manufacturing technique includes the clay raw materials and tempers, the shaping of the vessel, the decoration, the slip, and the firing technique. For terra sigillata, illite-rich clays with an increased and relatively constant calcium content between 6 and 20% CaO were used in each workshop. Fine quartz sand was necessary for production; therefore, it was either contained in the clay raw material or (like the calcium content) it was optimized by mixing clays from different layers of a deposit. Regarding the calcium content, in the case of Italic and southern Gaulish sigillata, CaO is about 8 and 14%, while other later sigillata wares mostly have CaO content below 8%.

The slip is a thin overlay prepared from a fine slurry of an illite-rich clay (high in potassium, aluminum, and iron). This coating is not a glaze but a heavily sintered engobe. Experimental reconstructions showed that the best luster was found at around 15-20% calcium levels and at firing temperatures around 1000 °C. To determine the

provenance of very fine ceramics such as terra sigillata, the mineralogical-petrographic examination under a polarizing microscope is usually less informative than determining the chemical composition. The matrix is frequently microscopically indissoluble, so it sometimes does not permit reliable conclusions. Non-plastic inclusions always consist of fine-grained quartz with other minerals, mainly feldspar (Ettlinger, 1990, 33–34).

Central Italian sigillata shows exceptional uniformity in composition, leading to the conclusion that Roman potters probably exploited the same sedimentary outcrops to manufacture calcareous clay products. Such outcrops -even in different locations- include the clayey layers of the Marine Pliocene (and of the Lower Pleistocene), which appear at Rome, in the Monte Mario area, and the Tiber Valley. These layers are found on the volcanic massif of Monte Vico, around which the Tiber turns north, between Capena and Orte. They extend towards Orvieto, Chiusi, and the Val di Chiana and further east towards Terni and Perugia. To the west of Rome, such formations appear along the Tyrrhenian coast near Cerveteri and further north towards Tarquinia. Consequently, the Tiber Valley could be considered the main supplier of Rome with calcareous and non-calcareous ceramics, a fact which, along with the navigability of the Tiber, allowed many ceramic workshops to develop (Olcese, 2004).

The firing occurred in a carefully controlled, oxidizing atmosphere to achieve a bright red, shiny appearance. Terra sigillata pots were never exposed to fumes or gases containing CO_2. The slip's high gloss and very homogeneous red color resulted from ceramic pieces being isolated from wood combustion products, such as smoke, soot, and other unburned hydrocarbons (Leon et al., 2015; Rice, 2015). In Padua (via Montona), indirect-flame kilns are attested from the mid-1st century AD to the second half of the 2nd century AD. They bear fireboxes that separate their firing chambers by solid, unslotted platforms. In this type of kiln, heating takes place by radiation, while combustion gases are ejected through vertical trunks fixed to the kiln walls (Maritan et al., 2018).

In Gaul, potters would build ceramic tubes (tubuli) that led the hot gasses from the heat source through the firing chamber in a similar process, heating the pots without coming into direct contact with them. Different types of kiln spacers and ceramic supports were used to maintain the piles of plates, cups, and other vessels straight and separate and to prevent fusing between individual pots stacked on top of one another

(Van Oyen, 2016). In North Africa, the technique is called “à casettes” and allows different ways to position these ceramic supports inside the kiln. They could be stacked base-upwards, in which case the kiln had to be filled with pottery beforehand, or they could be stacked base-downwards, as in modern kilns (Barraud et al., 1998).

The oxidizing firing at temperatures between 850 and 1050 °C resulted in the red color of the slip due to the red iron oxide hematite (Ettlinger, 1990, 35). The main goal was for the slip to become ‘sintered,’ meaning some of the material fused. Firing had to maintain higher and more consistent temperatures for extended periods to achieve this. Therefore, the sigillata firing process relied on expert skills and high fuel input, such as wood (Van Oyen, 2016).

1.6 Introduction to Ceramic Compositional Analysis

Ceramics can be studied on various levels with numerous techniques. Simple visual observations of their form, surface decoration, and typology can be carried out within the archaeological context. However, sophisticated analytical equipment can also analyze their compositional signatures and microscopic structures. This method is defined as “ceramic compositional analysis” and can be sectioned into geochemical and mineralogical approaches. Geochemical and mineralogical techniques share similar goals and are thus mostly complementary. They aim to detect compositional patterns within ancient ceramic assemblages that could answer meaningful archaeological questions and test hypotheses (Quinn, 2013).

Geochemical techniques such as instrumental neutron activation analysis (INAA), Raman spectroscopy, X-ray fluorescence (XRF), inductively coupled plasma mass spectrometry (ICP-MS), and synchrotron radiation are used to characterize the elemental signatures of ancient pottery, down to the level of parts per trillion (0.0000000001%). Mineralogical techniques like X-ray diffraction (XRD) characterize archaeological ceramics regarding the types of minerals they contain and their abundances (Quinn, 2013, 2022).

Technological features of ceramic production can be inferred using thin section petrography and scanning electron microscopy (SEM). Compositional analysis can also be employed to pinpoint the provenance of pottery, consequently providing evidence for its distribution through trade and exchange of goods. Other applications

allow us to determine raw materials and recipes, design conservation strategies, and detect forgeries (Quinn, 2022).

Thin sections of ceramic materials are slices taken from a sherd. They are uniformly 30 µm thick, fixed onto a glass microscope slide. Ceramic petrography applies the techniques of optical mineralogy, thin section petrography, and soil micromorphology to identify the types of minerals and rock inclusions and to define the matrix and the "voids" that occur in the ceramic body. Thin sections are observed with a "polarizing light microscope" or "petrographic microscope" under plane-polarized light (PPL) or crossed-polarized light (XPL) (Rice, 2015).

To conclude, ceramic compositional analysis can collect valuable data from ceramic ethnography, historical records, and experimental archaeology, contributing to the broader understanding of pottery manufacture (Quinn, 2022). Archaeometric studies can address various archaeological questions, such as the intended use of pottery, functionality, provenance, absolute dating, and post-depositional processes. A multidisciplinary approach is required to create successful research strategies (Gliozzo, 2020a).

CHAPTER 2: MATERIALS AND METHODS

2.1 Sample description

In March 2023, 15 representative samples were taken from terra sigillata vessels at the pottery laboratory in Civitella d'Agliano. The selected fragments of terra sigillata have varying provenance and quality, but all belong to the same consumption center, the Roman *villa* at Spoletino. The samples come from the Neronian filling of the cistern, apart from sample SP.05.2023, which comes from the mid-4th century AD context. Photographs of the sampled fragments that bear stamps are listed in the Appendix.

Figure 16. Macroscopic photograph of sample SP.01.2023.

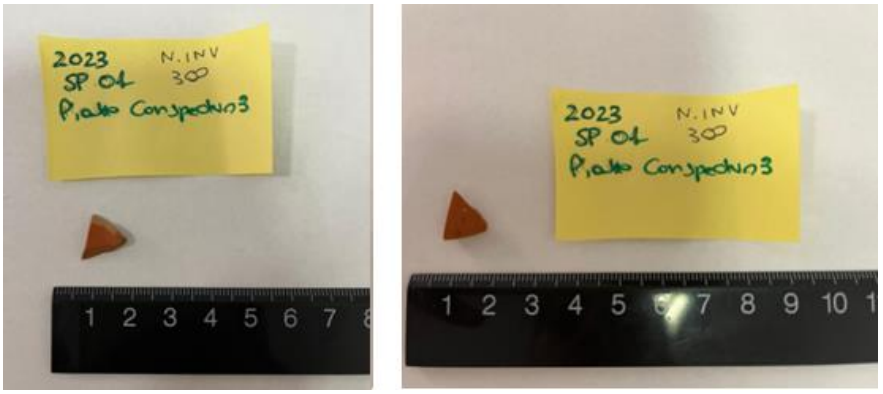

Sample SP.01.2023 (Figure 16) belongs to a dish of *Conspectus* Form 3. It is restored from 10 fragments; it bears a stamp in *planta pedis* of L. Plotidius Zosimus (OCK 1488.8). It could be attributed with certitude to the Scoppieto production, and it could be approximately dated in the 2nd/3rd quarter of the 1st century AD (see Appendix, Figure 1).

Figure 17. Macroscopic photograph of sample SP.02.2023.

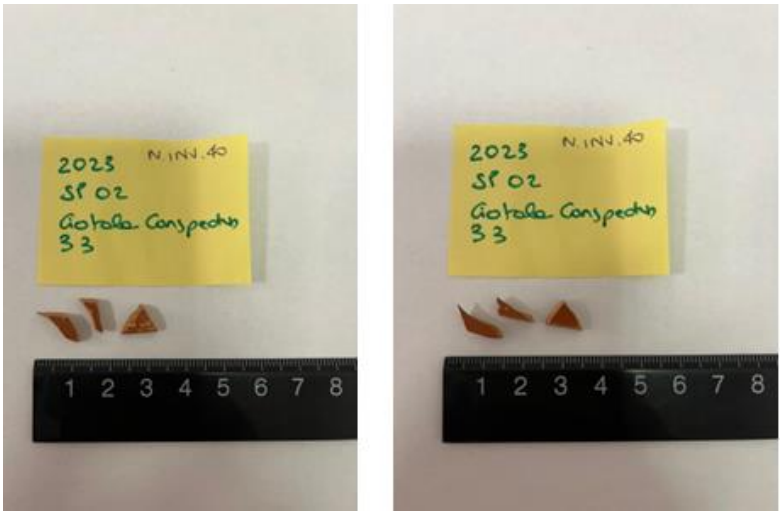

Sample SP.02.2023 (Figure 17) belongs to a bowl of *Conspectus* Form 33, and it is restored from 13 fragments. It bears a stamp in *planta pedis*, which is too worn to be identified. As a mere suggestion, we can infer that it again refers to L. Plotidius (OCK 1484.8?) and thence again from Scoppieto (see Appendix, Figure 2).

Figure 18. Macroscopic photograph of sample SP.03.2023.

Sample SP.03.2023 (Figure 18) belongs to a bowl of *Conspectus* Form 36. It bears a stamp in *planta pedis* of L. Plotidius Zosimus (OCK 1488.6). It could be attributed to the Scoppieto workshop, approximately dated in the 2nd/3rd quarter of the 1st century AD (see Appendix, Figure 3).

Figure 19. Macroscopic photograph of sample SP.04.2023.

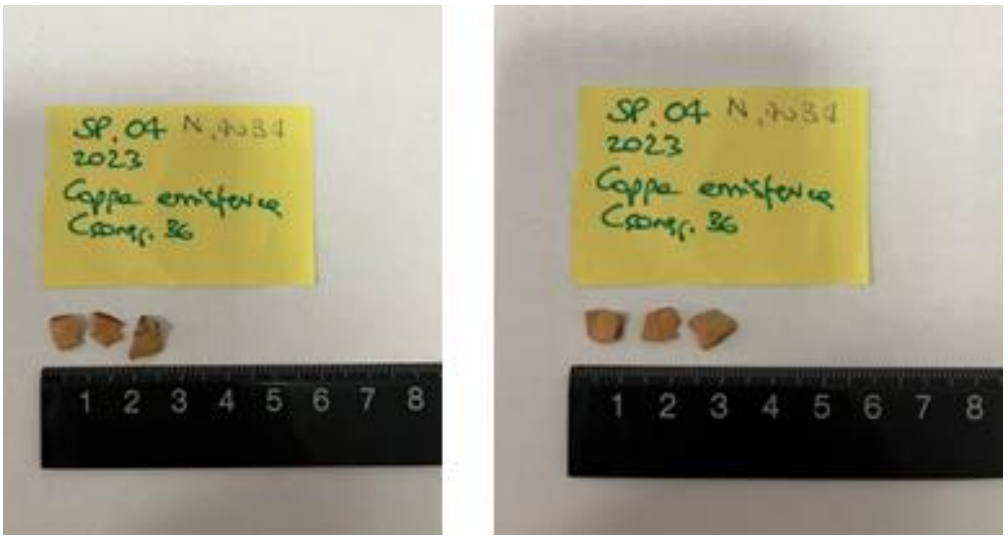

Sample SP.04.2023 (Figure 19) belongs to a bowl of *Conspectus* Form 36. It bears a stamp in *planta pedis* (see Appendix, Figure 4), which is very worn but can be tentatively attributed to Scoppieto (OCK 1488.33?).

Figure 20. Macroscopic photograph of sample SP.05.2023.

Sample SP.05.2023 (Figure 20) belongs to a large plate decorated with a scene of Gigantomachy, a *unicum*. It is the only sample from the mid-4th century AD context, but its production center is unidentified. One possible origin could be the middle Tiber Valley.

Figure 21. Macroscopic photograph of sample SP.06.2023.

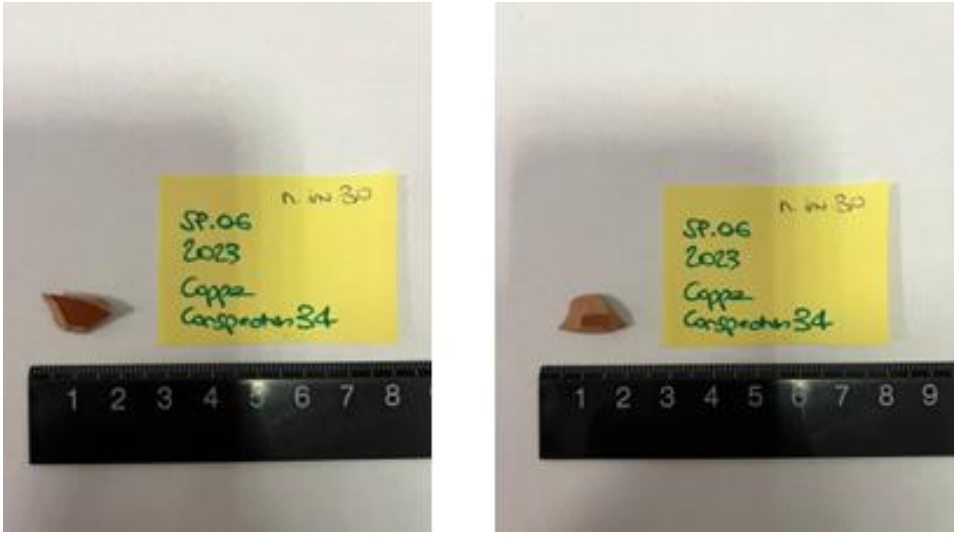

Sample SP.06.2023 (Figure 21) belongs to a bowl of *Conspectus* Form 34, but its production center is unidentified.

Figure 22. Macroscopic photograph of sample SP.07.2023.

Sample SP.07.2023 (Figure 22) belongs to a dish similar to form *Conspectus* 39. It is restored from 9 fragments, and its production site is uncertain, maybe the Po Valley or Central Italy (see Appendix, Figure 5).

Figure 23. Macroscopic photograph of sample SP.08.2023.

Sample SP.08.2023 (Figure 23) also comes from a vessel of unique form, a small jug that is not included in the classification by Ettlinger (1990). Its production remains unidentified.

Figure 24. Macroscopic photograph of sample SP.09.2023.

Sample SP.09.2023 (Figure 24) belongs to a dish of *Conspectus* Form 3. It is restored from 8 fragments; it bears a stamp in *planta pedis* of L. Plotidius Zosimus (OCK 1488.39). It could be attributed with a high degree of certainty to the Scoppieto workshop, and it could be approximately dated in the 2nd/3rd quarter of the 1st century AD. Based on macroscopic observations, this item was not fired well (see Appendix, Figure 6).

Figure 25. Macroscopic photograph of sample SP.10.2023.

Sample SP.10.2023 (Figure 25) belongs to a dish of *Conspectus* Form 3. It is restored from 19 fragments; it bears a stamp of Cornelius in *planta pedis* (OCK 612). These stamps are mainly attributable to P. Cornelius from Arezzo (OCK 624), active between 10-50 AD. However, some examples in Po Valley fabric and other examples from northern findspots may be products of A. Cornelius, who could be approximately dated after 15 AD (OCK 614). Therefore, the production site of SP.10.2023 could be Arezzo (see Appendix, Figure 7).

Figure 26. Macroscopic photograph of sample SP.11.2023.

Sample SP.11.2023 (Figure 26) belongs to a cup of *Conspectus* Form 27. It is restored from 3 fragments; its production center has not been identified.

Figure 27. Macroscopic photograph of sample SP.12.2023.

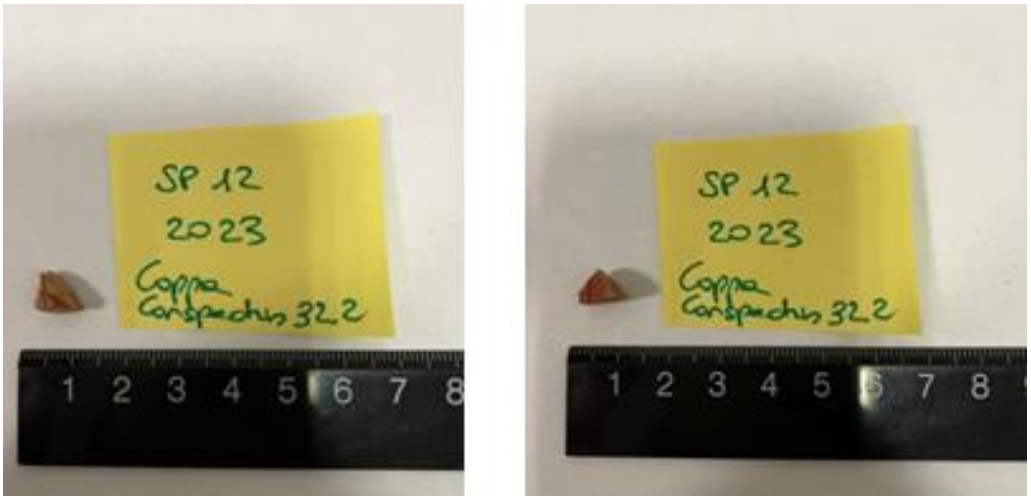

Sample SP.12.2023 (Figure 27) belongs to a bowl of Conspectus form 32.2 (Ettlinger, 1990). It is restored from 5 fragments; its production center has not been identified.

Figure 28. Macroscopic photograph of sample SP.13.2023.

Sample SP.13.2023 (Figure 28) belongs to an undecorated bowl of *Conspectus* Form 36. It is restored from 3 fragments; it bears a stamp in *planta pedis* of P. AV( ) GL ( ) (OCK 362.1), an unidentified potter who was active in the second half of the 1st century AD in central Italy, possibly at or near Scoppieto (see Appendix, Figure 8).

Figure 29. Macroscopic photograph of sample SP.14.2023.

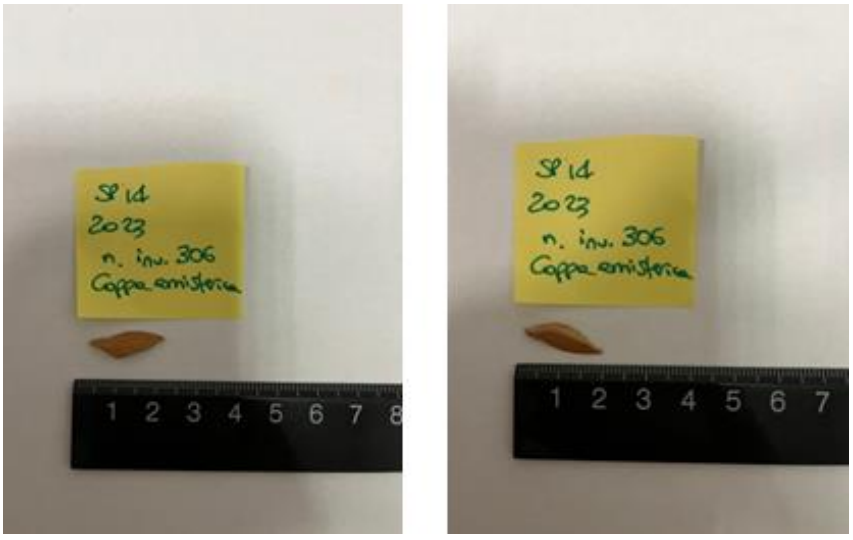

Sample SP.14.2023 (Figure 29) belongs to a bowl of *Conspectus* Form 36. It is restored from 5 fragments; it has a characteristic orange color, but its production has not been identified.

Figure 30. Macroscopic photograph of sample SP.15.2023.

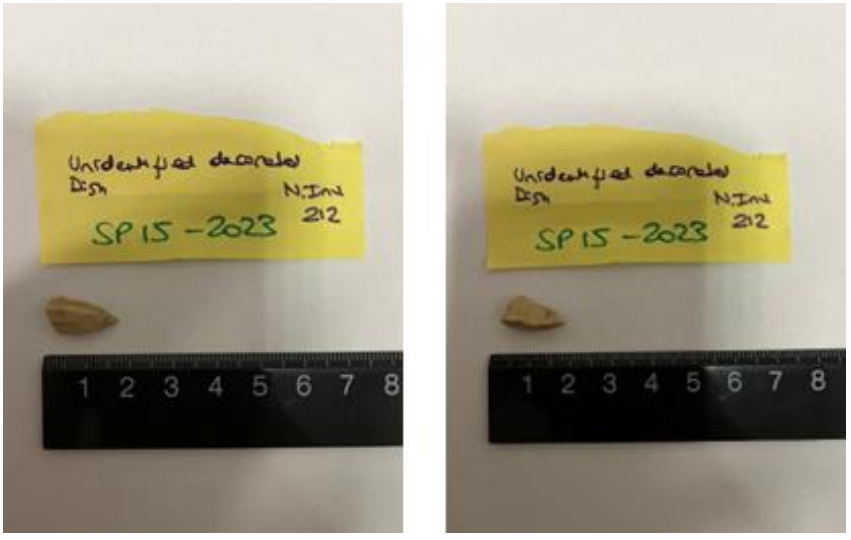

Sample SP.15.2023 (Figure 30) belongs to a dish with a horizontal decorated rim of unknown form. Its production center has not been identified.

Table 2. Information related to the samples includes the inventory number of the documented item, the date of excavation, the stratigraphic layer of origin, the form according to Ettlinger (1990), the overall number of preserved fragments, and its provenance (if attributed).

Sample	Inventory Number	Date	Stratigraphic Unity	Form	Number of fragments	Production
SP.01.2023	300	2016	401;402	Dish Consp. 3	10	Scoppieto
SP.02.2023	40	2015	200; 201	Bowl *Consp.*33	13	Unknown (Possibly Scoppieto?)
SP.03.2023	38	2015	202	Bowl *Consp.*36		Scoppieto
SP.04.2023	34	2015	203	Bowl *Consp.*36		Scoppieto?
SP.05.2023	301		11; 501; 503; 602; 604; 700	Large plate with a Gigantomachy scene		Unknown (Possibly middle Tiber Valley?)
SP.06.2023	30	2016	401	Bowl *Consp.*34		Unknown
SP.07.2023	302	2016		Dish *Consp.* 39 *similis*	9	Uncertain. Maybe Padanian or Central Italy
SP.08.2023	71		107	Small Jug of unique form		Unknown
SP.09.2023	303	2015; 2016	201; 401	Dish *Consp.* 3	8	Scoppieto
SP.10.2023	304	2015	201	Dish *Consp.* 3	19	Arezzo
SP.11.2023	60	2015	300	Cup *Consp.* 27	3	Unknown
SP.12.2023	305	2016	402	Bowl *Consp.* 32.2	5	Unknown
SP.13.2023	44	2015	201	Bowl *Consp.* 36 (undecorated)	3	Central Italy (possibly near Scoppieto)
SP.14.2023	306	2014	104; 105	Bowl *Consp.* 36	5	Unknown
SP.15.2023	212=307		700	Dish with horizontal decorated rim		Unknown

2.2 Analytical techniques

An integrated analytical approach based on non-destructive techniques was performed to acquire petrographic, mineralogical, and compositional characterization of terra sigillata pottery from Spoletino. The following techniques were utilized: Optical Microscopy in thin section, Scanning Electron Microscopy – Energy Dispersive X-ray Spectroscopy (SEM-EDS), and Fourier-transform infrared spectroscopy (FTIR).

2.2.1 Optical Microscopy in thin section

Optical Microscopy in thin section, performed using a polarized light microscope, is an invasive technique that allows the identification of minerals according to their optical properties, such as the shape, the color, and the cleavages of inclusions (Velde & Druc, 1999).

As mentioned above, sample preparation requires making a thin section, a ceramic slab of 0.03 mm thickness fixed to a glass slide (see Chapter 1.6). Before cutting and polishing, the section should be impregnated with epoxy resin to consolidate the sample. Epoxy resin is vital for friable ceramic materials or specimens with pores and cracks that often need to be impregnated in a vacuum. Ceramic sherds are usually cut transverse to the plane of the sherd within a few millimeters of an edge, allowing examination of both inner and outer surfaces and surface decorations. Other sections cut in different orientations may be more helpful for addressing specific research questions (Reedy, 2008).

Polishing can be done by manually rotating the sample on a glass plate in a mixture of fine grit and water or on a horizontal rotating lapping device with grit slurry or grinding/polishing paper. Silicon carbide (SiC) powder or “carborundum” with a diameter of 10–16 μm (600–800 grit), calcinated aluminum oxide, and industrial diamond paste are generally applied as abrasives in thin section preparation (Quinn, 2022).

Epoxy resin or a similar polymer is used to mount the ceramic slab onto the glass slide (a typical size of glass slides can be 46 x 27 mm). The epoxy or the polymer should have a refractive index like that of quartz, the most common mineral in ceramics. Quartz is very resistant to weathering; therefore, most clay deposits and archaeological ceramics contain quartz clasts/inclusions. The correct thickness is reached when quartz

grains are transparent under cross-polarized light (XPL) (Velde & Druc, 1999). A glass cover slip is sometimes fixed on top of the sample to protect the thin section and reduce light scattering. When observed under a petrographic microscope, minerals in thin sections of uniform thickness can be identified due to their optical properties, usually at magnifications ranging from 10x to 500x (Reedy, 2008).

Three main components comprise the ceramic paste (or fabric) in thin section: clay matrix, inclusions, and voids. The clay matrix is the prevalent, relatively fine-grained material in which coarser particles are inserted (Whitbread, 1995). It is usually translucent at 30 μm and typically has brown absorption and interference colors in PPL and XPL, respectively. Inclusions are the isolated particles within the matrix, and voids are holes where no matrix or inclusions appear. The clay and all particles <10 μm in size, such tiny mineral inclusions, are described as the "clay matrix." The clay matrix, inclusions, and pores hold essential information for pottery manufacture and use, as potters intentionally controlled their composition and abundance to suit specific purposes (Quinn, 2022).

Ceramic inclusions can be aplastic, usually consisting of mineral and rock fragments, or plastic, which were malleable or plastic when the artifact was formed (Quinn, 2013). "Temper" refers to material purposely added by the potter (Whitbread, 1995). Many valuable observations can be carried out regarding granulometry: description of the size, sorting, shape, and percentage of inclusions of different kinds in the fabric and their distribution and alignment. Roundness (smoothness of the outline) and sphericity (surface area) distinguish different inclusions, typically by comparing them with visual charts. The fabric's inclusion percentage is usually determined by point counting, modal analysis, or comparative charts (Rice, 2015).

Other practical observations of minerals under the microscope include absorption colors, pleochroism, relief, and cleavage in PPL. In XPL, common mineral properties that can be evaluated are opacity, interference colors and birefringence, extinction angle, and twinning (Braekmans & Degryse, 2017). The relative difference in refraction index between adjacent mineral phases using Becke lines can be estimated. Even absolute measurement of the refraction index can be achieved by reference oils and by assessing the crystal symmetry (by measuring the allowed vibration directions of light in the crystals) (Reedy, 2008). All the above yield important data regarding the raw materials and their processing, pottery production techniques and firing

conditions, and post-depositional alterations of the ceramic samples (Whitbread, 1995).

To sum up, thin section petrography is a fast and inexpensive analytical technique for the preliminary investigation of pottery that produces a comprehensive qualitative overview of the phase composition and texture. Many qualitative observations regarding the statistical analysis of minerals' size, shape, and space distribution can be quantified using specific analytical software. CCD cameras can be attached to petrographic microscopes and computers to systematically record and analyze digital images. Image analysis software packages are available that can process digital photomicrographs of thin sections and collect quantitative data from them (Artioli & Angelini, 2010). For this study, a Leica DM750 P microscope was used, with a video camera Leica MC190 HD and LAS V4 4.12 software for image acquisition (Figure 31).

Figure 31. Leica DM750 P microscope mounted with a digital camera and a computer for image capture (Department of Earth Sciences, Sapienza University of Rome).

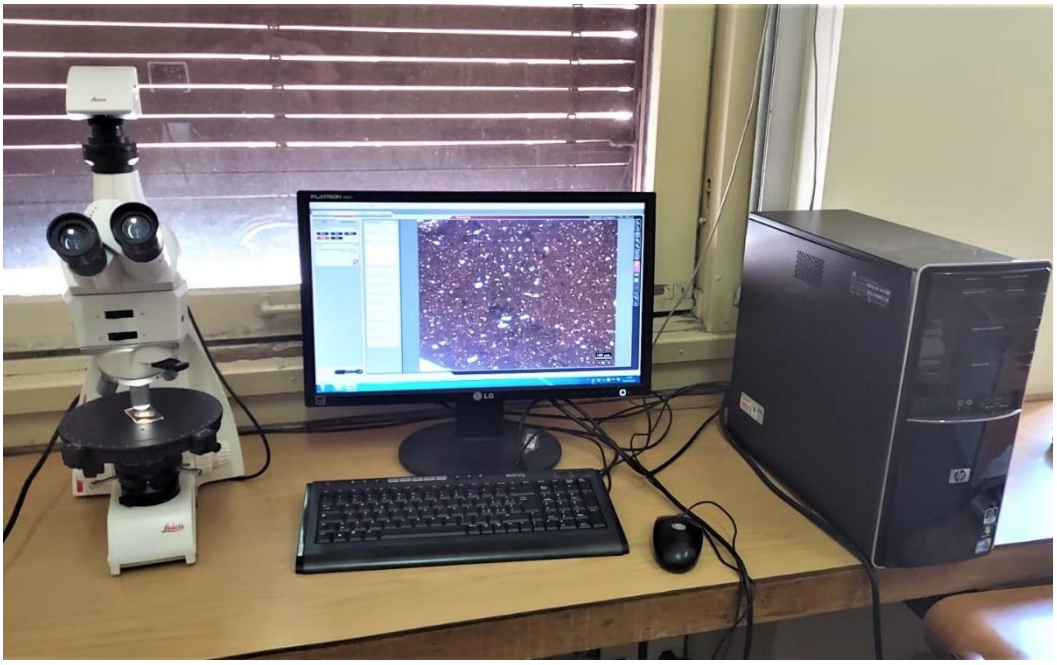

2.2.2 Scanning Electron Microscopy – Energy Dispersive X-ray Spectroscopy (SEM-EDS)

The microstructure, morphology, and composition of archaeological ceramics can be studied at high magnification using a scanning electron microscope. SEM has a greater field depth than the optical microscope, meaning features can be viewed in three dimensions. It has higher magnification (at 50,000x or more) and excellent resolution (down to 0.5 nm); therefore, it can discern between structures several nanometers in size (Quinn, 2022). Most importantly, SEM can be a non-invasive technique, as both thin sections and fresh fractures of ceramic sherds can be analyzed (Rice, 2015).

In general, scanning electron microscopes (SEM) feature electron beams accelerated between 102−104 eV, corresponding to wavelengths of 0.123–0.012 nm. SEM utilizes electrostatic and electromagnetic lenses to manipulate the direction and divergence of the electron beam. The electron beam that bombards the specimen is scanned horizontally across the surface in two perpendicular (x and y) directions. This process is called raster scanning and forces the beam to cover a rectangular area on the sample. The detector is connected to a display device, such as a cathode-ray tube (CRT), on which the SEM image will be displayed. The electron beam in the CRT is synchronized with the beam in the SEM, so for every point on the specimen (within the raster-scanned area), there is an equal point on the display screen simultaneously (Egerton, 2006).

At each point, the detector collects the signal from atoms' interactions with the electron beam at or near the sample's surface (Figure 32). A very thin layer of gold, carbon, or platinum should be applied as a coating to render the ceramic samples conductive. Backscattered electrons, secondary electrons, and characteristic X-rays may form the SEM image. All these types of signals demand specialized detectors for their detection (Artioli & Angelini, 2010).

Accelerated electrons are scattered elastically (by electrostatic interaction with atomic nuclei) and inelastically (by interaction with atomic electrons) when they encounter a solid material. High energy backscattered electrons are “deflected” or backscattered from the sample's surface. At deflection angles of less than 90° degrees, this interaction is called “forward” scattering. However, some electrons leave the target due to their high kinetic energy, having been deflected through an angle of more than 90° degrees. They re-enter the surrounding vacuum and can be collected as a

backscattered-electron (BSE) signal by the detector (Egerton, 2006).

Figure 32. Schematic diagram of a scanning electron microscope with a CRT display (Egerton, 2006, p. 126, fig. 5-1).

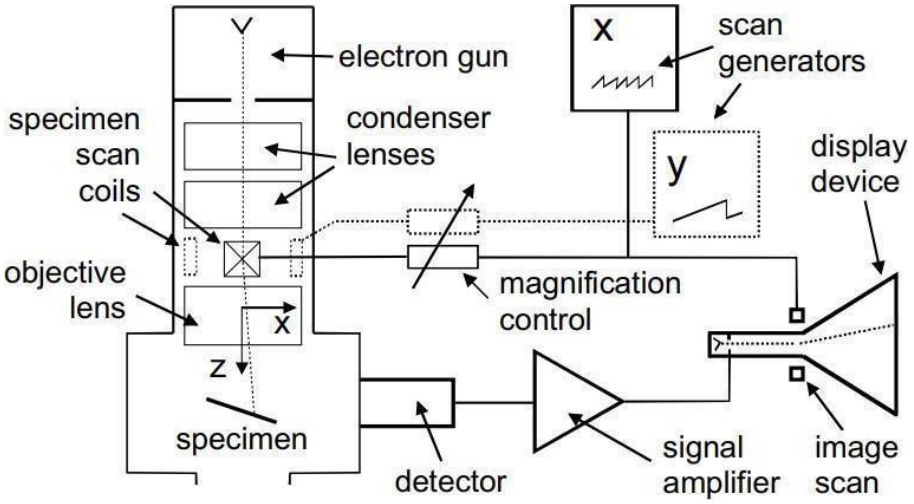

Due to their larger atomic nuclei, heavier elements backscatter more electrons than lighter elements. They appear brighter in the BSE image and can reveal compositional differences within samples regarding the average atomic weight of specific regions. For this reason, backscattered electrons detect the contrast between areas with different chemical compositions, which emerge as different shades of grayscale in a BSE image (Quinn, 2022).

Secondary electrons are low-energy electrons (< 50 eV) emitted by the atoms in the sample following ionization processes due to the interaction with the electron beam. According to the principle of energy conservation, any energy lost by a primary electron will seem like an increase in energy of the atomic electrons that cause the inelastic scattering. The weakly bound outer-shell (valence) electrons use only a fraction of this additional energy as potential energy to free themselves from a specific atom. The rest will be retained as kinetic energy, which allows the escaping electrons to pass through the solid as secondary (SE) electrons. Secondary electrons interact with other atomic electrons and are scattered inelastically, progressively losing their kinetic energy. The final SE image collected by the detector originates within a few nanometers from the surface and displays the surface structure or topography of the sample (Egerton, 2006).

An energy dispersive X-ray spectrometer (EDS) can significantly enhance the chemical information we acquire from different phases coupled with the SEM system.

SEM-EDS can also record the intensity of the characteristic X-ray lines of specific elements at each raster point to produce maps of elemental distribution. Ionization processes produce fluorescence X-rays due to the interaction of the primary electron beam with the specimen (Artioli & Angelini, 2010).

When an inner-shell electron transitions from a higher to a lower energy level, an X-ray photon is emitted, whose energy is equal to the difference in the two quantum levels (Figure 33). The primary electrons in an SEM-EDS system bombard the sample and excite inner-shell electrons to a higher energy. In the de-excitation process, characteristic X-rays are produced, and by identifying the wavelengths or photon energies present, we can perform elemental analysis (Egerton, 2006).

Elemental maps are extremely useful in interpreting element distributions in complex polyphasic materials, such as ceramics. SEM analysis can discern clay minerals that comprise the matrix, which are too small (< 2μm) to be discerned in thin section and help us interpret the types and sources of raw materials used in ceramic production (Velde & Druc, 1999).

SEM imaging can also provide important information regarding the maximum firing temperature, the firing atmosphere, and the abundance of calcite in the ceramic body. The higher the firing temperature is, the more vitrified the clay fabric appears like a smooth, continuous, glassy structure. Finally, the EDS signal recorded from ceramics can also be used for mineralogical characterization, allowing the semi-automated identification of inclusions and clay minerals. The EDS spectrum is recorded from a raster point in the sample and is characteristic of the mineral excited by the electron beam. Mineral maps can also be generated compared to electronic databases (Quinn, 2022).

Figure 33. Scanning electron microscopy. When the electron beam interacts with atoms in the sample, they emit secondary electrons, but some are reflected or backscattered. The ejection of secondary electrons also causes the generation of characteristic X-rays (Quinn, 2022, p. 794, fig. 9.2).

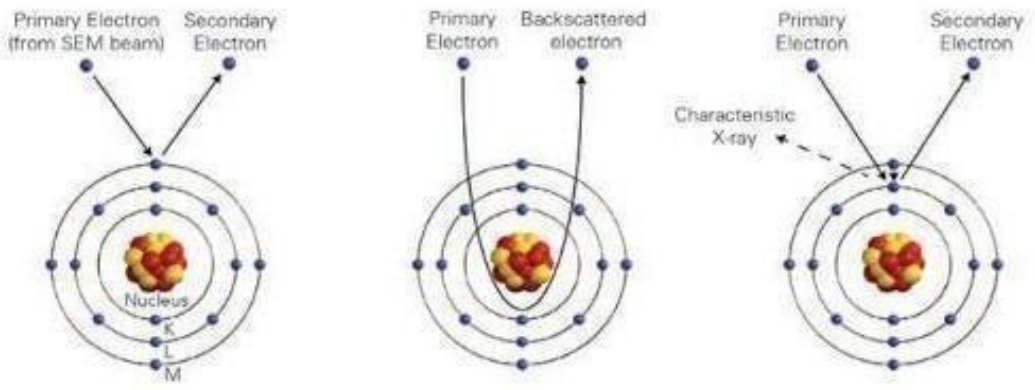

For this project, Scanning Electron Microscopy coupled with Energy Dispersive X-ray Spectroscopy (SEM-EDS) was performed for the micro-morphological characterization and the micro-chemical analyses of ceramic samples. Thin sections were previously metalized with graphite to be electrically conductive.

A FEI Quanta 400 scanning electron microscope was used with an attached EDS detector operated in high vacuum conditions and with an accelerating voltage of 20 keV (Figure 34). Morphological features of the slip (with particular emphasis on thickness and sintering degree) can be observed and compared with those of the underlying body, examining the interface between the slip and ceramic paste. Secondary and backscattered electron images were acquired for surface topography and structural information (Pollard & Heron, 2008).

Figure 34. FEI Quanta 400 scanning electron microscope with attached EDS detector (Department of Earth Sciences, Sapienza University of Rome).

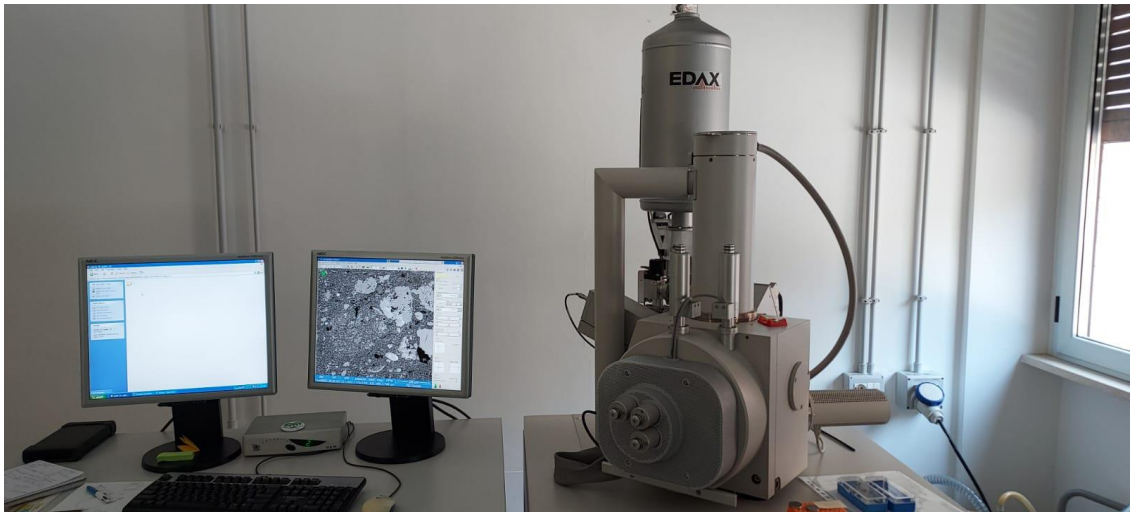

2.2.3 Fourier-transform infrared spectroscopy (FTIR)

Vibrational spectroscopy is a method that analyzes molecular structure by examining the interaction between electromagnetic radiation and nuclear vibrations in molecules. One of the most common vibrational spectroscopy techniques for material characterization is Fourier transform infrared spectroscopy (FTIR). The type of electromagnetic radiation in FTIR is infrared light in a wavelength range longer than visible light: ≤0.7 μm. The term wavenumber (ν) is used for the characterization of electromagnetic waves, which is defined as the reciprocal of wavelength (λ) in the unit of cm^{-1}.

$$\nu = 1/\lambda.$$

FTIR is an infrared spectroscopy in which the Fourier transform method simultaneously obtains an infrared spectrum in a range of wavenumbers (Leng, 2009). The Infrared spectrum consists of the Near Infrared (NIRS between 14000–4000 cm^{-1}), Mid Infrared (MIRS between 4000–400 cm^{-1}), and Far Infrared (FIRS between 400–10 cm^{-1}). The NIRS region is indicative of overtones and harmonic or combination vibrations; the MIRS region helps us study the fundamental vibrations and the rotation-vibration structure of small molecules, while the FIRS region is meant for the low heavy atom vibrations (Theophanides, 2012).

Both simple molecules and organic compounds display many possible vibrational modes corresponding to molecular bond stretching and bending (Pollard & Heron, 2015). Some types of bonds present in a sample are symmetric and asymmetric stretching vibrations, in-planar bending vibrations, out-of-planar bending vibrations, and torsion vibrations. A vibration mode must initiate a net change in the dipole moment of a molecule to be infrared active. A molecule has a center of positive charge and a center of negative charge. If these two centers are parted by a distance (l), the dipole moment (μ) is defined, and it stands for the amount of electrical charge at the charge center of the molecule.

$$\mu = el$$

The dipole moment can also be caused by the electric field of an electromagnetic wave, so the molecule does not need a permanent dipole moment. This vibrating dipole moment creates a dipolar electric field that absorbs a discrete amount of IR energy. This phenomenon is called infrared absorption and is the foundation of

infrared spectroscopy. When a molecule is excited by infrared electromagnetic waves, one particular frequency will correspond to the vibrational frequency of the molecule (ν_{vib}). Therefore, waves with the frequency $\nu_{ph} = \nu_{vib}$ will excite the molecular vibration, and the molecule will absorb the electromagnetic radiation with this specific frequency ν_{ph}. This excitation will cause the energy of molecular vibration to increase, usually by $\Delta\nu = +1$. The fundamental transition from $\nu = 0$ to $\nu = 1$ is most common during infrared absorption, although other transitions may be possible.

Absorption of radiation does not take place when vibrations are infrared inactive. For example, the stretching vibrations of completely symmetrical double and triple bonds do not change the dipole moment because the positive and negative charge centers stay symmetrical, and the dipole moment is always equal to zero during vibration (Leng, 2009).

Since molecules have many possible vibrational modes, different compounds may have very similar IR spectra. For this reason, FTIR does not provide a precise chemical characterization of a sample, but it should be viewed as a "chemical fingerprinting" technique. Infrared spectra are usually interpreted using a correlation chart or a database (Figure 35). The region of the IR spectrum that is most efficient for analyzing organic compounds is 2.5–15 μm (wave numbers 4000–650 cm^{-1}), where organic compounds emit a characteristic absorption spectrum, and it is called the "fingerprint region" (Pollard & Heron, 2015). For studying ceramic materials, the most beneficial area is the spectral region between 400 and 1500 cm^{-1}, which considers the influence of the fingerprints of the carbonate absorption band (~1400 cm^{-1}) and inorganic compounds (below 1000 cm^{-1}) (Medeghini et al., 2016).

Fourier Transform IR spectrometers include an infrared light source and a detector. They also rely on a Michelson Interferometer comprising one beam-splitter and two mirrors. The infrared radiation from the source passes through the Michelson interferometer, and the beam-splitter transmits half of the infrared (IR) beam and reflects the other half. The two split beams hit a fixed mirror and a moving mirror simultaneously. After being reflected by the mirrors, the two split beams join at the beam-splitter again to excite the sample before they reach the detector. The moving mirror changes the optical path to cause light interference between the two split beams. The two split beams display constructive and destructive interference periodically, with constant changes in optical path difference (δ).

Figure 35. Infrared correlation chart showing approximate wavenumber ranges of common bond vibrations in organic molecules (Pollard & Heron, 2015, p. 67, fig. 2.19).

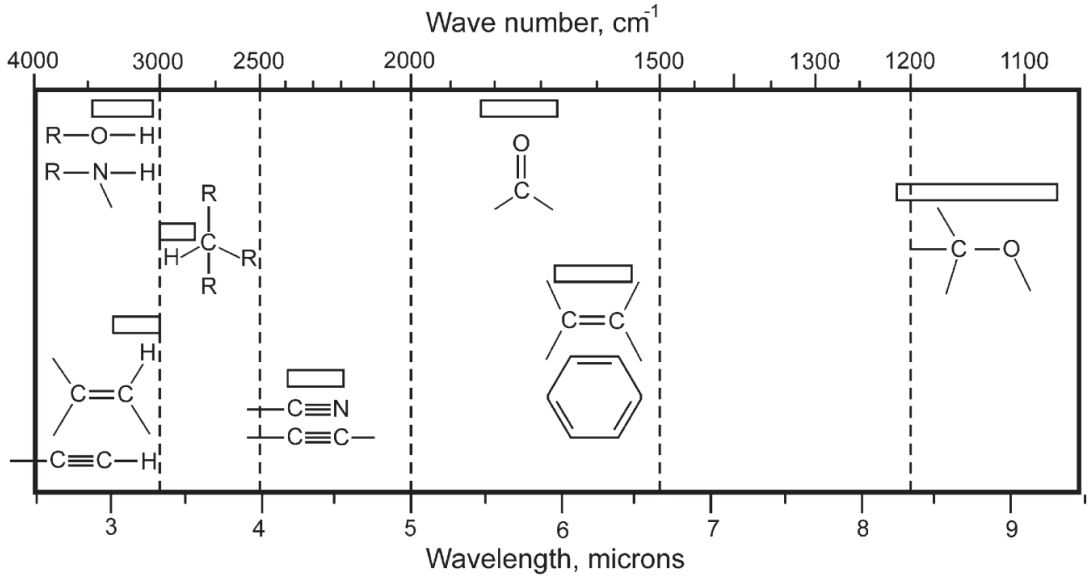

A change in the position of the moving mirror causes a change in δ value. The final interferogram is the plot of light interference intensity as a function of optical path difference. Fourier transformation is essential to transform an interferogram into an infrared spectrum, a plot of the light intensity versus wavenumber (Leng, 2009).

The FTIR detector receives interferogram signals transmitted to or reflected from a sample (Figure 36). A computer equipped with FTIR constructs the infrared spectrum using a fast Fourier transform (FFT) algorithm, which converts the intensity versus optical path difference to the intensity versus wavenumber. Lasers also provide a precise method of monitoring displacements of a moving mirror in the interferometer, so the absorption spectra are defined more precisely (Theophanides, 2012).

An infrared spectrum converted from an interferogram by Fourier transform is called a single beam spectrum. It contains both spectra from the sample and background. The background spectrum has only the information from the instrument and atmosphere, not from the analyzed sample. The background spectrum relays the instrument's impact from the detector, the beam-splitter, the mirrors, and the IR source. The atmospheric influence is mainly from water vapor and carbon dioxide. The ratio of the single beam spectrum of a sample with the background spectrum should be performed to minimize the background influence. This process leads to a transmittance spectrum, which occurs when an IR beam passes through the sample (Leng, 2009).

Figure 36. Schematic illustration of an FTIR Spectrometer (Theophanides, 2012, p. 7, fig. 5B).

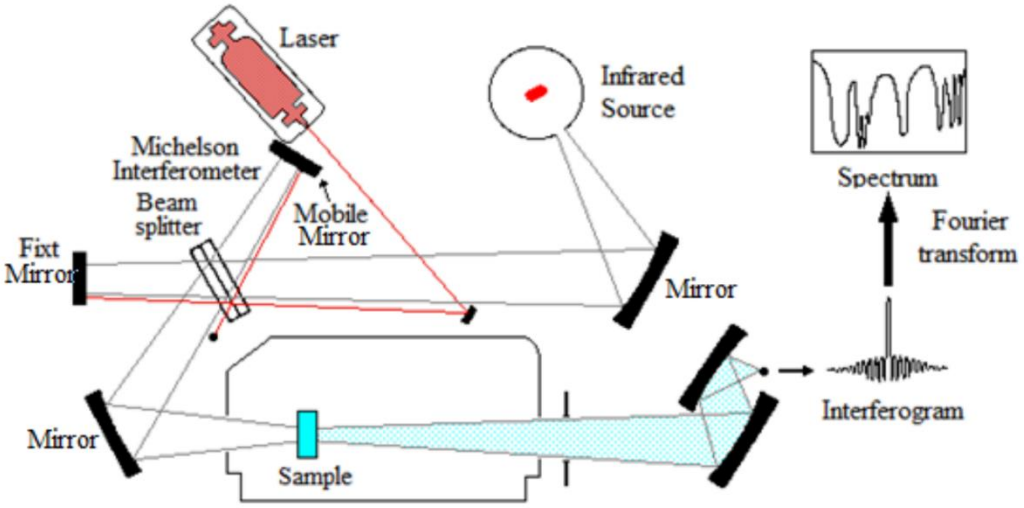

Transmittance (T) is described as the ratio of intensities. I is the intensity measured in a single beam spectrum of the sample, and Io is the intensity measured in the background spectrum.

$$T = I/Io$$

Transmittance is often expressed as %T, which forms the scale of the vertical axis and causes vibration band peaks to point downward. The spectrum can also be presented as absorbance (A) versus wavenumber when vibration band peaks point upward. The absorbance is calculated from the transmittance.

$$A = -\log T$$

FTIR spectra in reflectance mode obtain an infrared spectrum by reflecting IR radiation from a solid or liquid sample. For this study, two types of FTIR spectroscopy were performed: FTIR Microscopy in transmission mode and Attenuated Total Reflection (ATR) (Leng, 2009).

The FTIR microscope has an optical system combining visible optical and infrared light spectroscopy. Also, it can be operated in either transmittance or reflectance with minimal sample preparation, either transparent or opaque to light. The microscope also has an infrared detector and video camera or eyepieces. The infrared spectrum is obtained from a microscopic area even in the order of 10 × 10 μm. Mapping or FTIR imaging can be accomplished by scanning a sample using a motorized sample stage. FTIR microscopes have only one system of condenser and objective lens. The lenses

used in FTIR microscopy belong to the Cassegrain type and are made of curved mirrors. They reflect light using a larger mirror with a parabolic shape to collect the beam and a smaller mirror with a hyperbolic shape to focus it. The Cassegrain lens neither absorbs the energy of infrared light nor possesses chromatic aberration as a conventional optical lens does. Their magnifying power is relatively low, generally less than 10× (Leng, 2009).

A Nicolet Continuum Infrared Microscope from Thermo Scientific in transmission mode was used for the FTIR point analysis of all 15 samples. It is coupled with a video camera and OMNIC software for Windows 10. A minimal amount of sample was placed on a diamond cell and crushed on it. The spectra were collected by coaddition of 40 running scans at a resolution of 8 cm^{-1} and covered the 4000–650 cm^{-1} spectral range.

In an ATR mode, we measure the alterations that take place in an internally reflected IR beam when it encounters a sample. The IR beam passes through an optically dense diamond crystal with a high refractive index at an angle of typically 45° (relative to the crystal surface). When the angle of incidence is greater than the critical angle θc (function of refractive index of two media), all incident radiations are entirely reflected at the interface of the crystal and the sample, resulting in total internal reflectance (Artioli & Angelini, 2010).

This internal reflectance causes an exponentially decaying evanescent wave that extends into the sample, typically by a few micrometers (0.5-5 μm). The evanescent wave will be attenuated or altered when the sample absorbs energy in a specific infrared spectrum region. A detector then collects the beam as it escapes the crystal. The detector registers the attenuated IR beam as an interferogram signal, which can then be converted into an IR spectrum (Theophanides, 2012).

A Nicolet iS50 FTIR Spectrometer from Thermo Scientific in ATR mode with OMNIC software for Windows 10 was used for bulk analysis of the 15 ceramic samples (Figure 37). Minimal sample preparation was required, as the ceramic samples were placed directly onto the diamond crystal area. Just enough amount of sample was used to cover the crystal completely. Then, the pressure arm was positioned over the diamond cell and locked into a precise position. Force was applied to the sample, leveling it onto the diamond surface. The spectra were collected by coaddition of 32 running scans at a resolution of 4 cm^{-1} and covered the 4000–400

cm^{-1} spectral range.

Figure 37. Nicolet iS50 FTIR Spectrometer paired with Nicolet Continuum IR Microscope from Thermo Scientific and OMNIC software for Windows 10 (Department of Earth Sciences, Sapienza University of Rome).

CHAPTER 3: RESULTS

The following chapter lists the results from all applied analytical techniques: Optical Microscopy in thin section, Scanning Electron Microscopy – Energy Dispersive X-ray Spectroscopy (SEM-EDS), and Fourier-transform infrared spectroscopy (FTIR).

3.1 Optical Microscopy in thin section

After all the fifteen ceramic samples were observed under the optical microscope, the following two groups could be distinguished. A less micaceous fabric group 1 consists of samples SP.04.2023, SP.06.2023, SP.08.2023, SP.10.2023. It can be characterized by a relatively lesser amount of mica and a more compact matrix. Fabric group 2 is more micaceous compared to group 1, and it includes samples SP.01.2023, SP.02.2023, SP.03.2023, SP.05.2023, SP.09.2023, SP.11.2023, SP.12.2023, SP.13.2023, SP.14.2023. Samples SP.07.2023 and SP.15.2023 are loners. SP.07.2023 has fewer and finer inclusions, while SP.15.2023 is more calcareous with coarser inclusions than the other samples.

Less micaceous fabric group 1

Figure 38. Sample SP.04.2023 in PPL (left) and XPL (right), 2.5x magnification.

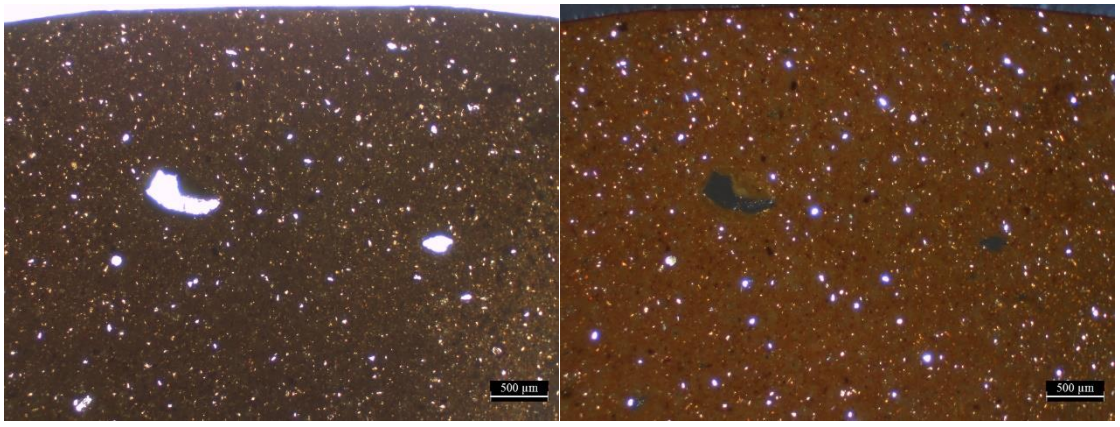

Sample SP.04.2023 has a 15% of inclusions with unimodal grain size distribution, equant and elongate, from sub-angular to rounded, from single to open spaced, and their maximum size is around 0.1 mm (Figure 38). Alignment to the margins of the sections cannot be spotted. Quartz is dominant, equant and elongate, from sub-angular to rounded, 0.02 mm to 0.1 mm in size. Micas are frequent, elongate, from angular to sub-rounded, 0.02 mm to 0.1 mm. Nodules of iron oxides are common, equant and elongate, sub-rounded to rounded, 0.02 mm to 0.05 mm. Voids are 3%, micro- to

meso- vesicles, and micro- to macro-vughs. Neither alignment to the margins of the section nor secondary calcite could be detected. The matrix is 82% in total, calcareous, and heterogeneous in color. It ranges from light brown to dark brown in plain polarized light (PPL) and golden orange to brown in XPL. It has weak optical activity. The slip appears as a dark brown margin in PPL and ranges from dark red to brown in XPL. It is optically active, and it bears secondary calcite.

Figure 39. Sample SP.06.2023 in PPL (left) and XPL (right), 2.5x magnification.

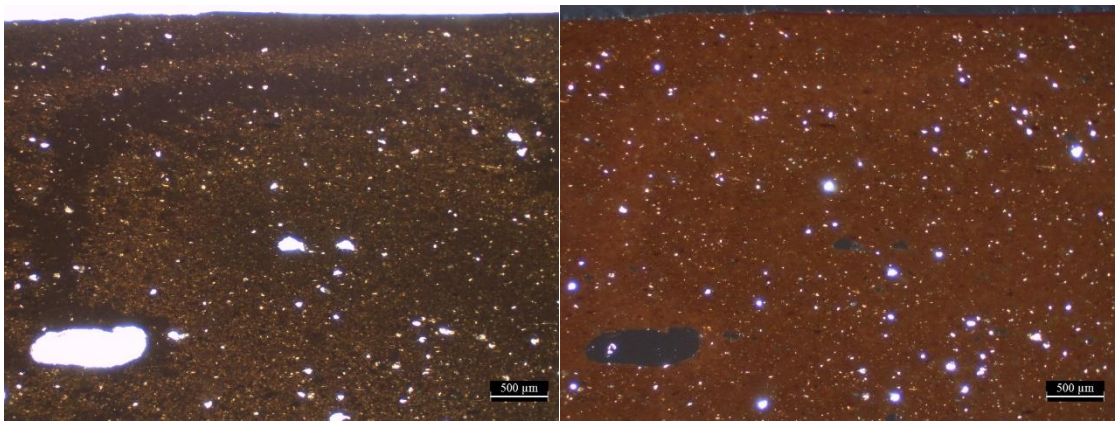

Sample SP.06.2023 has a 20% of inclusions, equant and elongate, from sub-angular to rounded, from single to open spaced, with unimodal grain size distribution (Figure 39). Inclusions are aligned to the margins of the section, and their maximum size is around 0.2 mm. Quartz is dominant, equant and elongate, from sub-angular to sub-rounded, 0.02 mm to 0.2 mm in size. Frequent inclusions are micas, elongate, from sub-angular to rounded, 0.02 mm to 0.1 mm. Nodules of iron oxides are common, equant and elongate, sub-rounded to rounded, 0.05 mm to 0.2 mm. Voids are 3%, micro- to meso- vesicles, and micro- to macro-vughs. They are aligned to the margins of the sections. Secondary calcite can be found in pores close to the margin. The matrix is 77% in total, calcareous, and heterogeneous in color. It ranges from light brown to dark brown in PPL, golden orange to dark brown in XPL, and shows weak optical activity.

The slip can be described as dark brown to orange-brown in PPL and dark red to orange in XPL. It is optically active, and it appears as a narrow margin.

Figure 40. Sample SP.08.2023 in PPL (left) and XPL (right), 2.5x magnification.

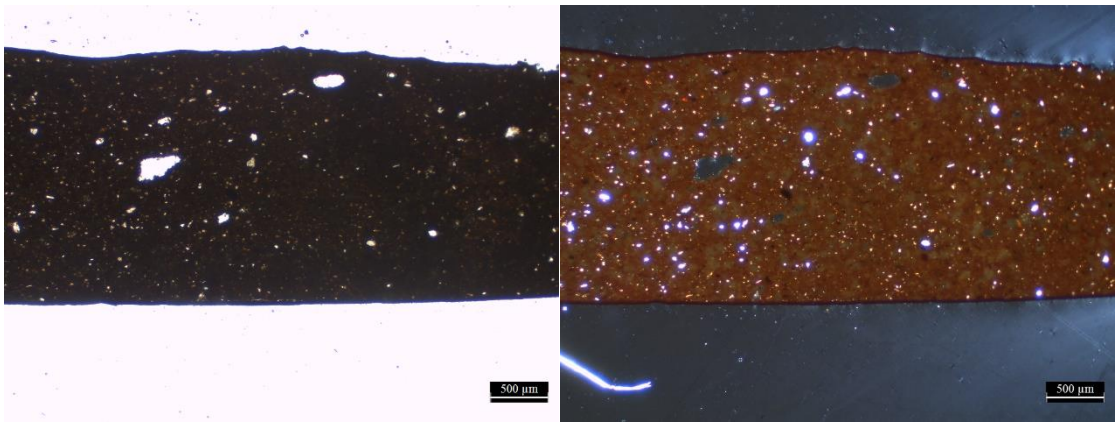

Sample SP.08.2023 has a 20% of inclusions, equant and elongate, from sub-angular to rounded, single to double spaced with unimodal grain size distribution (Figure 40). Inclusions are not aligned to the margins of the section, and their maximum size is around 0.1 mm. Quartz is dominant, equant and elongate, from sub-angular to rounded, 0.02 mm to 0.1 mm. Frequent inclusions are micas, elongate, sub-angular to sub-rounded, 0.02 mm to 0.06 mm. Common inclusions are nodules of iron oxides, equant and elongate, sub-rounded to rounded, 0.02 mm to 0.05 mm. Voids are 3%, micro- to meso-vesicles, and micro- to macro- vughs. They are not aligned to the margins of the section, and they do not contain any secondary calcite. The matrix is 77% in total, calcareous, and heterogeneous in color, from light brown to dark brown in PPL and golden orange to dark brown in XPL.

As for the slip, two margins are discernible: dark brown in PPL and dark red to brown in XPL. Both the matrix and the slip show weak optical activity.

Figure 41. Sample SP.10.2023 in PPL (left) and XPL (right), 2.5x magnification.

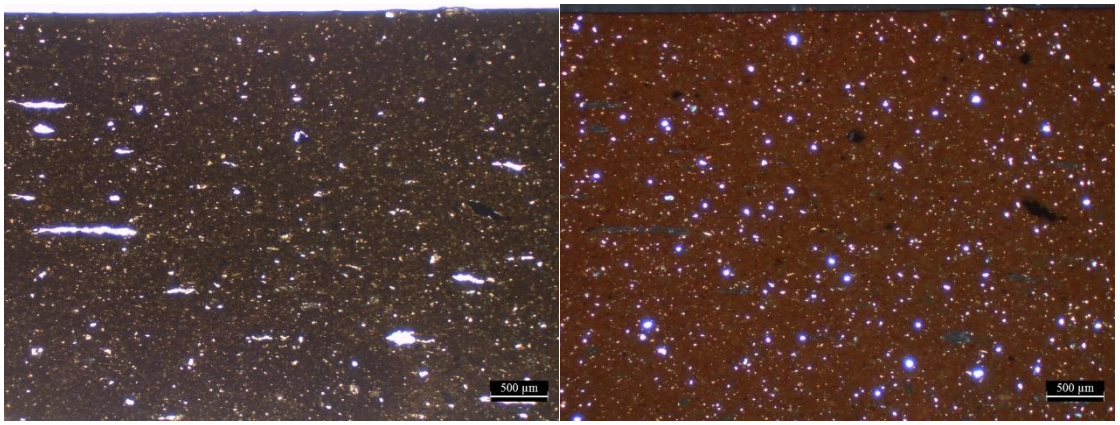

Sample SP.10.2023 has a 20% of inclusions, equant and elongate, from sub-angular to

rounded, single to open spaced with unimodal grain size distribution (Figure 41). Inclusions are not aligned to the margins of the section, and their maximum size is around 0.4 mm. Quartz is dominant, equant and elongate, from sub-angular to rounded, 0.02 mm to 0.1 mm. Frequent inclusions are micas, elongate, sub-angular to sub-rounded, 0.02 mm to 0.2 mm. Nodules of iron oxides are common, equant and elongate, sub-rounded to rounded, 0.02 mm to 0.4 mm. Voids are 5%, micro- to meso-vesicles, and micro- to macro-vughs. They are aligned to the margins of the section. The matrix is 75% in total, calcareous, and heterogeneous in color. It appears as light brown to dark brown in PPL, golden orange to dark brown in XPL, and shows weak optical activity.

Regarding the slip, two margins are visible with very weak optical activity, dark brown in PPL and from dark red to brown in XPL.

More micaceous fabric group 2

Figure 42. Sample SP.01.2023 in PPL (left) and XPL (right), 2.5x magnification.

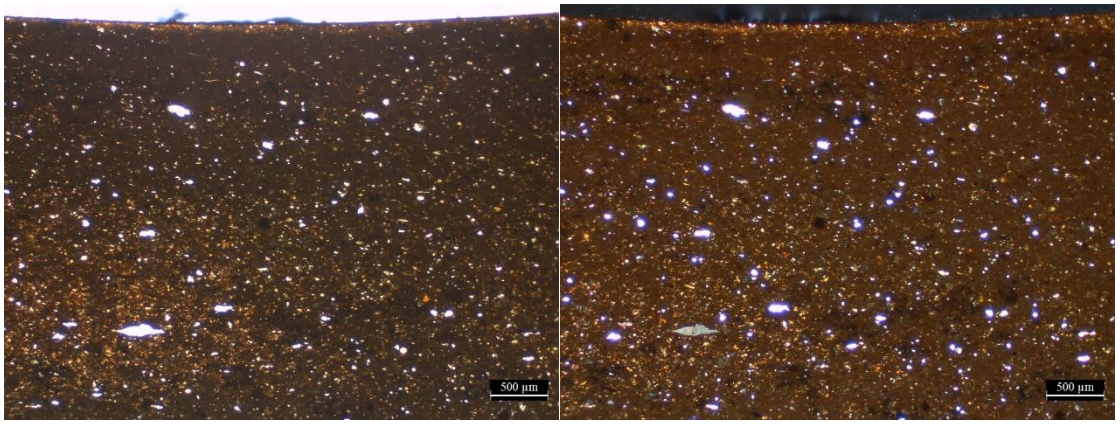

Sample SP.01.2023 has a 20% of inclusions, equant and elongate, from angular to rounded, from single to open spaced, with an unimodal grain size distribution and maximum inclusion size around 0.5 mm (Figure 42). The inclusions are aligned to the margins of the section. Quartz is dominant, equant and elongate, from angular to sub-rounded, 0.02 mm to 0.5 mm in size. Frequent inclusions are micas, elongate, from sub-angular to sub-rounded, 0.02 mm to 0.1 mm. Nodules of iron oxides are common, equant and elongate, sub-rounded to rounded, 0.02 mm to 0.3 mm. There are few calcite crystals, elongate, sub-angular to sub-rounded, 0.02 mm to 0.05 mm. Voids are 3%, mainly micro-vesicles and micro-vughs, in which secondary calcite was undetected. The matrix is 77% in total, calcareous, and heterogenous in color. It ranges from light brown to dark brown in PPL and golden orange to brown in XPL.

There is weak optical activity.

Regarding the slip, a dark brown margin can be spotted in PPL with a preparation layer underneath in a lighter yellow color (polishing). The same margin is yellow-red in XPL, and it is optically active.

Figure 43. Sample SP.02.2023 in PPL (left) and XPL (right), 2.5x magnification.

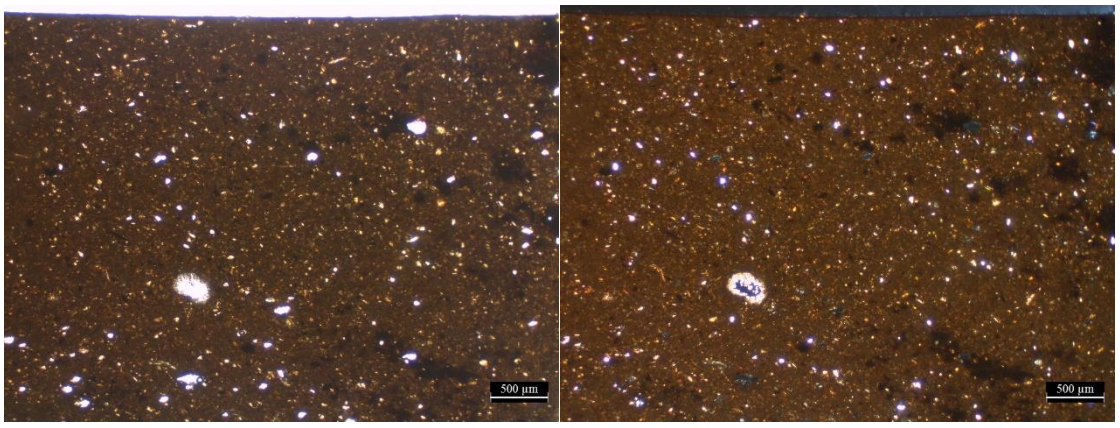

Sample SP.02.2023 has a 20% of inclusions, equant and elongate, from sub-angular to rounded, from single to open spaced (Figure 43). Inclusions have an unimodal grain size distribution; they are slightly aligned to the margins of the section, and their maximum size is around 0.5 mm. Quartz is dominant, equant and elongate, from sub-angular to sub-rounded, 0.02 mm to 0.2 mm in size. Micas are frequent inclusions, elongate, from sub-angular to sub-rounded, 0.02 mm to 0.1 mm. Nodules of iron oxides are common, equant and elongate, sub-rounded to rounded, 0.02 mm to 0.5 mm. Voids are 3%; they mainly consist of micro- to meso-vesicles and a few micro- to meso-vughs. They are not aligned to the margins of the section. Secondary calcite coating can be detected within two voids. The matrix is 77% in total, calcareous, and heterogeneous in color. It ranges from light brown to dark brown in PPL and golden orange to brown in XPL. It has moderate optical activity.

As for the slip, a dark brown margin is visible in PPL, which varies from orange-red to brown in XPL and bears a layer of secondary calcite.

Figure 44. Sample SP.03.2023 in PPL (left) and XPL (right), 2.5x magnification.

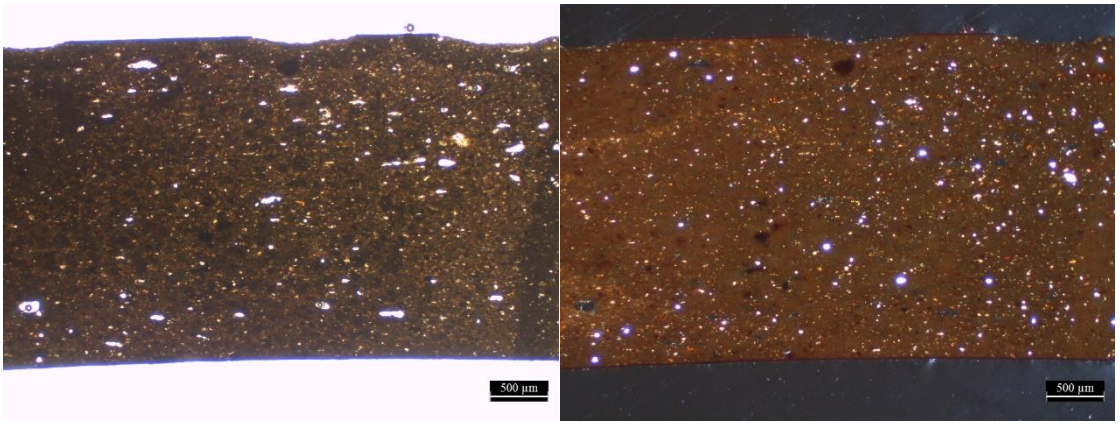

Sample SP.03.2023 has a 20% of inclusions, equant and elongate, from sub-angular to rounded, from single to open spaced with unimodal grain size distribution (Figure 44). Inclusions are aligned to the margins of the section, and their maximum size is about 0.2 mm. Quartz is dominant, equant and elongate, from sub-angular to rounded, 0.02 mm to 0.1 mm. Frequent inclusions are micas, elongate, from sub-angular to sub-rounded, 0.02 mm to 0.1 mm. Common inclusions are nodules of iron oxides, equant and elongate, sub-rounded to rounded, 0.02 mm to 0.2 mm. Very few calcite crystals are present, equant and elongate, sub-angular to sub-rounded, 0.02 mm to 0.2 mm. Voids are 3%, micro- to meso-vesicles, and few micro- to meso-vughs. They are aligned to the margins. Secondary calcite cannot be observed. The matrix is 77% in total, calcareous, and heterogeneous in color. It ranges from light brown to dark brown in PPL and golden orange to brown in XPL. There is moderate optical activity.

Regarding the slip, a dark brown margin is visible in PPL and ranges from dark red to brown in XPL. It is optically active. Secondary calcite is found in one of the margins.

Figure 45. Sample SP.05.2023 in PPL (left) and XPL (right), 2.5x magnification.

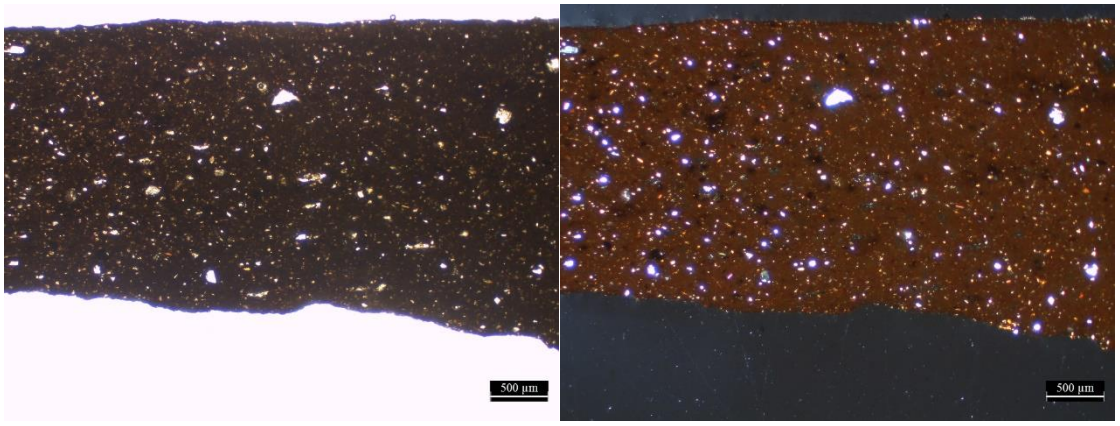

Sample SP.05.2023 has a 30% of inclusions, equant and elongate, from sub-angular to rounded, from single to open spaced with unimodal grain size distribution (Figure 45).

Inclusions are not aligned to the margins of the section, but their maximum size is approximately 0.2 mm. Quartz is dominant, equant and elongate, from sub-angular to sub-rounded, 0.02 mm to 0.2 mm in size. Frequent inclusions are micas, elongate, from sub-angular to rounded, 0.02 mm to 0.1 mm. Common inclusions are nodules of iron oxides, equant and elongate, sub-rounded to rounded, 0.02 mm to 0.1 mm. Very few inclusions of microcline are present, elongate, sub-rounded, 0.1 mm in size. Voids are 3%, microvesicles, and micro- to meso-vughs. Neither alignment to the margins of the section nor secondary calcite cannot be detected. The matrix is 67% in total, calcareous, and heterogeneous in color. Its color ranges from light brown to dark brown in PPL and golden orange to dark brown in XPL, with weak optical activity.

The color of the slip can be described as dark brown to orange-brown in PPL and from dark red to golden orange in XPL. The slip is optically active, and it has secondary calcite.

Figure 46. Sample SP.09.2023 in PPL (left) and XPL (right), 2.5x magnification.

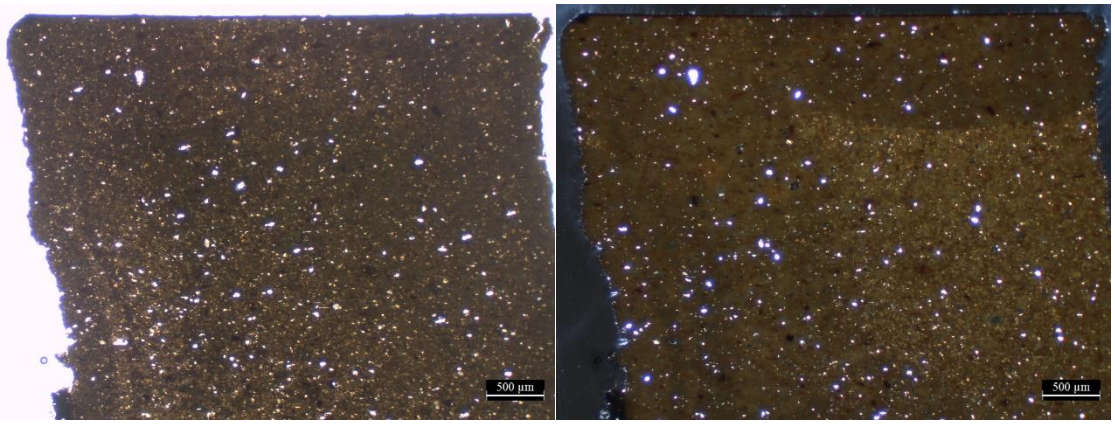

Sample SP.09.2023 has a 20% of inclusions, equant and elongate, from sub-angular to rounded, single to open spaced with unimodal grain size distribution (Figure 46). Inclusions are not aligned to the margins of the section, and their maximum size is around 0.2 mm. Dominant is quartz, equant, and elongate, from sub-angular to rounded, 0.02 mm to 0.1 mm. Frequent inclusions are micas, elongate, sub-angular to sub-rounded, 0.02 mm to 0.2 mm. Common inclusions are nodules of iron oxides, equant and elongate, sub-rounded to rounded, 0.02 mm to 0.2 mm. Voids are 3% micro- to meso-vesicles and micro- to meso-vughs. The matrix is 77% in total, calcareous, and heterogeneous in color. It ranges from light brown to dark brown in PPL and golden orange to dark brown in XPL with weak optical activity. There is also a dark area on the margin of the section.

Regarding the slip, two margins are discernible: dark brown in PPL and dark red to

brown in XPL. They have secondary calcite, and they show weak optical activity.

Figure 47. Sample SP.11.2023 in PPL (left) and XPL (right), 2.5x magnification.

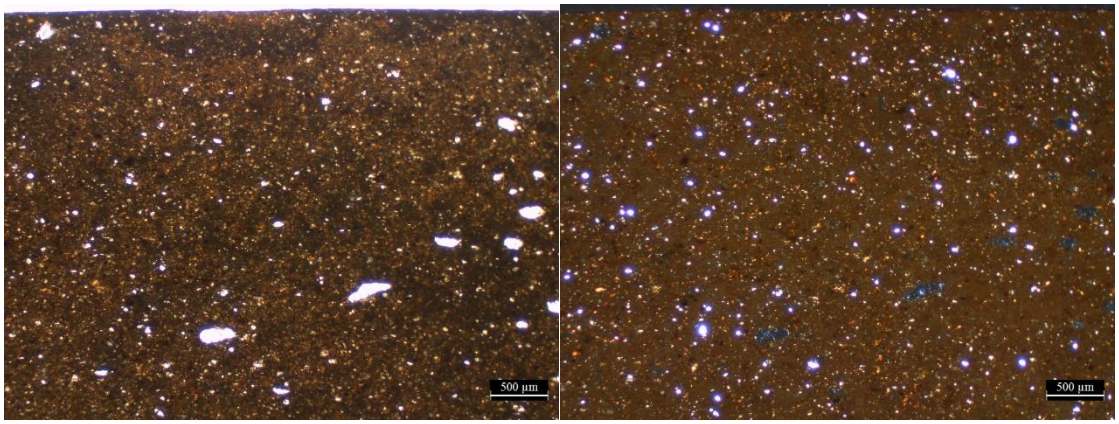

Sample SP.11.2023 has a 30% of inclusions, equant and elongate, from sub-angular to rounded, single to open spaced with unimodal grain size distribution (Figure 47). Inclusions are not aligned to the margins of the section, and their maximum size is around 0.3 mm. Dominant is quartz, equant and elongate, from sub-angular to rounded, 0.02 mm to 0.1 mm. Frequent inclusions are micas, elongate, sub-angular to sub-rounded, 0.02 mm to 0.3 mm. Common inclusions are nodules of iron oxides, equant and elongate, sub-rounded to rounded, 0.02 mm to 0.1 mm. A rare inclusion is micritic calcite, equant, rounded, 0.02 mm to 0.2 mm. Voids are 5%, micro- to meso-vesicles, and micro- to meso- vughs. Secondary calcite can be found along the margins of the voids. The voids are also aligned to the margins of the section. The matrix is 65% in total, calcareous, and heterogeneous in color. It ranges from light brown to dark brown in PPL and golden orange to dark brown in XPL with weak optical activity.

Regarding the slip, two margins are visible: dark brown in PPL and ranging from dark red to vivid orange in XPL. The slip shows moderate optical activity.

Figure 48. Sample SP.12.2023 in PPL (left) and XPL (right), 2.5x magnification.

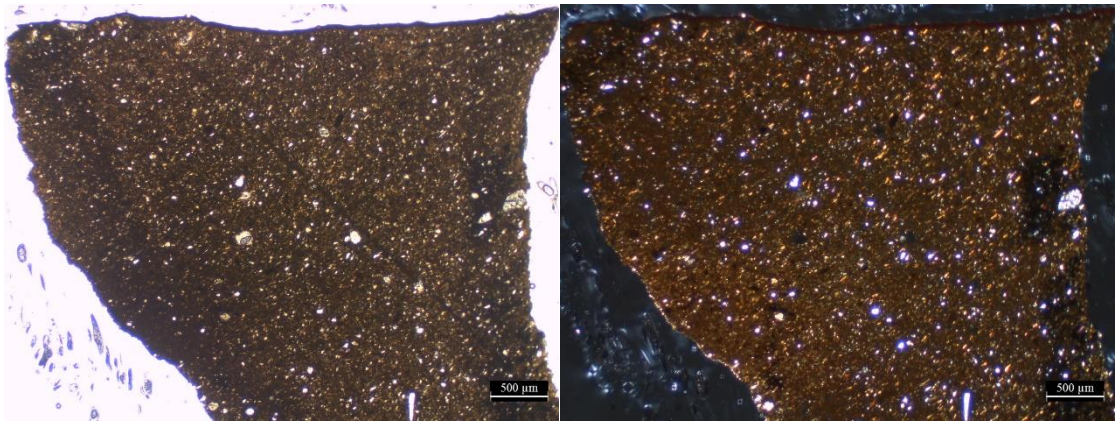

Sample SP.12.2023 has a 30% of inclusions, equant and elongate, from sub-angular to rounded, single to open spaced with unimodal grain size distribution (Figure 48). They are not aligned to the margins of the section, and their maximum size is around 0.3 mm. Quartz is dominant, equant and elongate, from sub-angular to rounded, 0.02 mm to 0.3 mm in size. Dominant inclusions are micas, elongate, sub-angular to sub-rounded, 0.02 mm to 0.1 mm. Common inclusions are nodules of iron oxides, equant and elongate, sub-rounded to rounded, 0.02 mm to 0.2 mm. A very rare inclusion is microcline, elongate, sub-rounded, 0.3 mm. Voids are 3%, micro- to meso- vesicles, and micro- to meso- vughs. Micritic calcite has partially infilled some voids. They are not aligned to the margins of the section. The matrix is 67% calcareous and heterogeneous in color. It ranges from light brown to dark brown in PPL and golden orange to dark brown in XPL, while some areas are darker grey-black. The matrix demonstrates weak optical activity.

The slip consists of two margins, dark brown in PPL and dark red to red-orange in XPL, with moderate optical activity.

Figure 49. Sample SP.13.2023 in PPL (left) and XPL (right), 2.5x magnification.

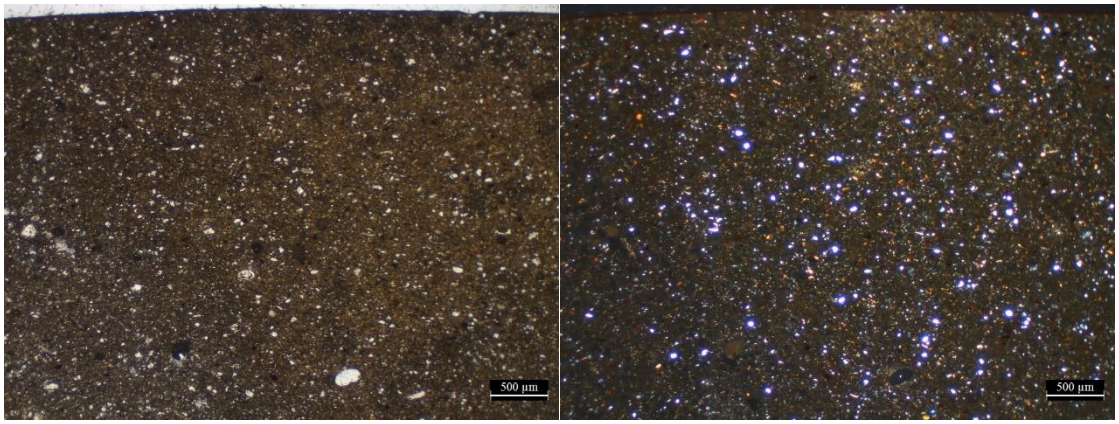

Sample SP.13.2023 has a 20% of inclusions, equant and elongate, from sub-angular to rounded, single to open spaced with unimodal grain size distribution (Figure 49). They are not aligned to the margins of the section, and their maximum size is about 0.2 mm. Quartz is dominant, equant and elongate, from sub-angular to rounded, 0.02 mm to 0.1 mm in size. Frequent inclusions are micas, elongate, sub-angular to sub-rounded, 0.02 mm to 0.2 mm. Common inclusions are nodules of iron oxides, equant and elongate, sub-rounded to rounded, 0.02 mm to 0.1 mm. Feldspars are rare, elongate, rounded, 0.2 mm. Voids are 3%, micro- to meso-vesicles, and micro- to meso-vughs. They are not aligned to the margins of the section, and they do not exhibit any secondary calcite. The matrix is 77% in total, calcareous, and heterogeneous in color. It ranges

from light brown to dark brown in PPL and XPL with very weak optical activity.

The slip comprises two margins, dark brown in PPL and dark red to vivid orange in XPL, with moderate optical activity.

Figure 50. Sample SP.14.2023 in PPL (left) and XPL (right), 2.5x magnification.

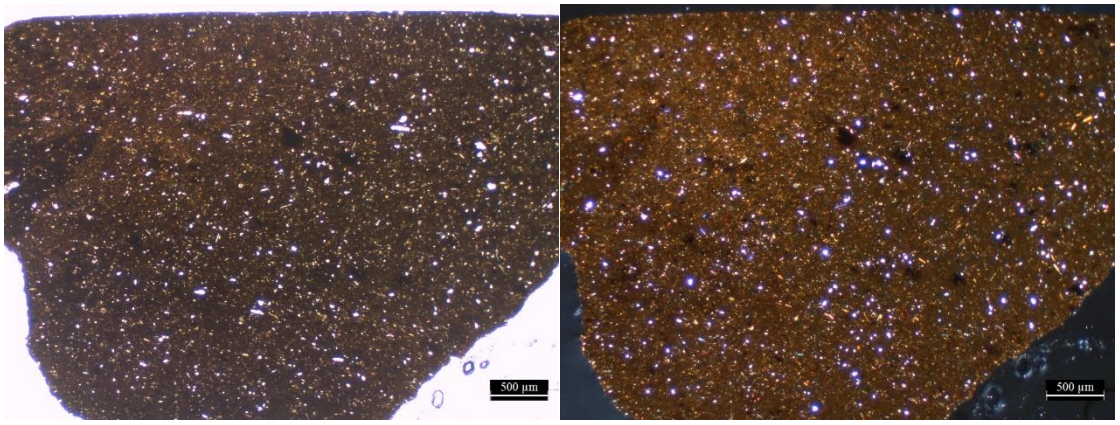

Sample SP.14.2023 has a 20% of inclusions, equant and elongate, from sub-angular to rounded, single to open spaced with unimodal grain size distribution (Figure 50). They are not aligned to the margins of the section, and their maximum size is around 0.2 mm. Quartz is dominant, equant and elongate, from sub-angular to rounded, 0.02 mm to 0.1 mm in size. Frequent inclusions are micas, elongate, sub-angular to sub-rounded, 0.02 mm to 0.1 mm. Common inclusions are nodules of iron oxides, equant and elongate, sub-rounded to rounded, 0.02 mm to 0.2 mm. Voids are 3%, micro- to meso- vesicles, and micro- to meso- vughs. They are aligned to the section's margins but do not contain secondary calcite. The matrix is 77% in total, calcareous, and heterogeneous in color. It ranges from light brown to dark brown in PPL and XPL with very weak optical activity.

The margins that compose the slip are not so well defined. They range from dark brown in PPL to orange-brown in XPL with weak optical activity.

Loners

Figure 51. Sample SP.07.2023 in PPL (left) and XPL(right), 2.5x magnification.

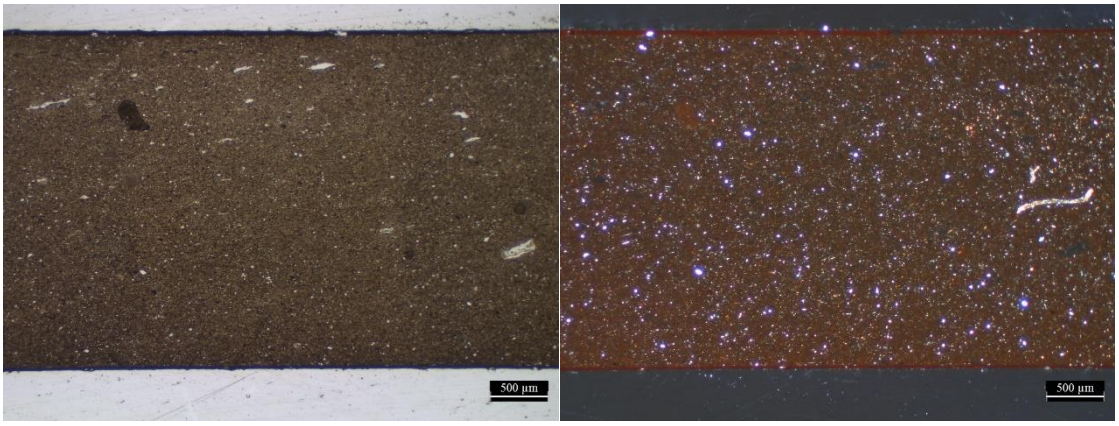

Sample SP.07.2023 has a 10% of inclusions, equant and elongate, from sub-angular to rounded, open spaced with unimodal grain size distribution (Figure 51). They are not aligned to the margins of the section, and their maximum size is 0.1 mm. Quartz is dominant, equant and elongate, from sub-angular to rounded, 0.02 mm to 0.1 mm in size. Frequent inclusions are micas, elongate, from sub-angular to rounded, 0.02 mm to 0.1 mm. Common inclusions are nodules of iron oxides, equant and elongate, sub-rounded to rounded, 0.02 mm to 0.1 mm. Voids are 3%, micro- to meso-vesicles, and micro- to macro-vughs. They are aligned to the margins, but they do not have any secondary calcite. The matrix is 87% in total, calcareous and homogeneous, light brown in PPL, and deep orange to brown in XPL with weak optical activity.

The slip consists of two margins, dark brown in PPL and ranging from brown to orange-brown in XPL, with weak optical activity.

Figure 52. Sample SP.15.2023 in PPL (left) and XPL (right), 2.5x magnification.

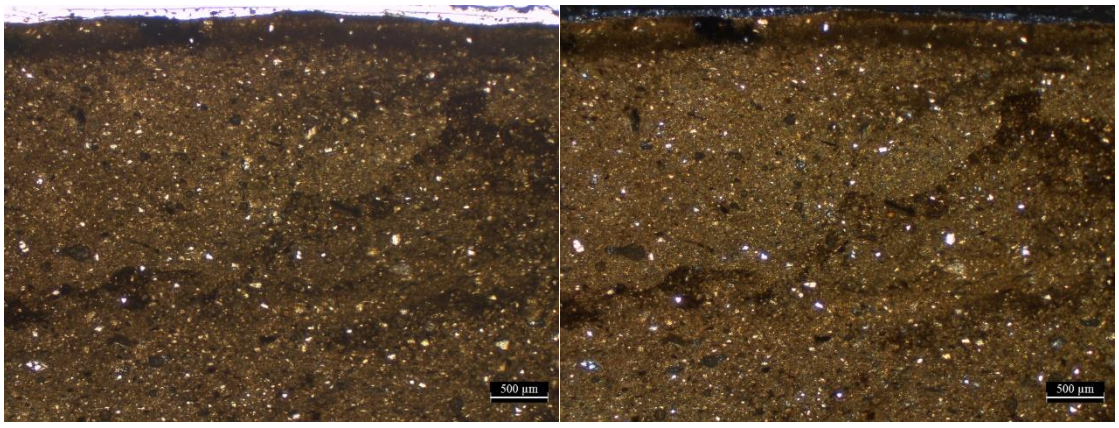

Sample SP.15.2023 has a 20% of inclusions, equant and elongate, from sub-angular to rounded, double to open spaced with unimodal grain size distribution (Figure 52).

They are not aligned to the margins of the section, and their maximum size is around 0.6 mm. Quartz is dominant, equant and elongate, from sub-angular to rounded, 0.02 mm to 0.1 mm in size. Frequent inclusions are micas, elongate, sub-angular to sub-rounded, 0.02 mm to 0.1 mm. Common inclusions are nodules of iron oxides, equant and elongate, sub-rounded to rounded, 0.02 mm to 0.6 mm. Voids are 3%, micro- to meso- vesicles, and micro- to meso- vughs. Secondary calcite can be traced along their margins. The voids are not aligned to the margins of the section. The matrix is 77% in total, calcareous, and heterogeneous in color, ranging from light brown to dark brown in PPL and golden orange to dark brown in XPL. Some areas are darker grey-black with weak optical activity.

Regarding the slip, the margins of the slip are not well defined. They range from dark to light brown in PPL and XPL and do not showcase optical activity. The following table (Table 3) summarizes OM observations.

Table 3. Summary of optical microscopy.

Fabric groups	Samples	Inclusions		Voids	Matrix	Slip
Less micaceous fabric group 1	SP.04.2023	15% unimodal grain size distribution, equant and elongate, from sub-angular to rounded.	Dominant: quartz, equant and elongate, from sub-angular to rounded, 0.02-0.1 mm. Frequent: mica, elongate, from angular to sub-rounded, 0.02-0.1 mm Common: nodules of iron oxides, equant and elongate, sub-rounded to rounded, 0.02-0.05 mm	3%, micro- to meso- vesicles, and micro- to macro-vughs.	82% calcareous, heterogeneous from light brown to dark brown in PPL and golden orange to brown in XPL. Weak optical activity.	A dark brown margin is visible in PPL and ranges from dark red to brown in XPL. It is optically active. Secondary calcite.
	SP.06.2023	20% unimodal grain size distribution, equant and elongate, from sub-angular to rounded. Aligned to the margins of the section.	Dominant: quartz, equant and elongate, from sub-angular to sub-rounded, 0.02-0.2 mm Frequent: mica, elongate, from sub-angular to rounded, 0.02-0.1 mm Common: nodules of iron oxides, equant and elongate, sub-rounded to rounded, 0.05 - 0.2 mm	3%, micro- to meso- vesicles, and micro- to macro-vughs. Aligned to the margins of the sections. Secondary calcite in pores close to the margin.	77% calcareous, heterogeneous from light brown to dark brown in PPL and golden orange to dark brown in XPL. Weak optical activity.	A visible margin ranges from dark brown to orange-brown in PPL and dark red to orange in XPL. It is optically active.
	SP.08.2023	20% unimodal grain size distribution, equant and elongate, from sub-angular to rounded.	Dominant: quartz, equant and elongate, from sub-angular to rounded, 0.02-0.1 mm Frequent: mica, elongate, sub-angular to sub-rounded, 0.02-0.06 mm Common: nodules of iron oxides, equant and elongate, sub-rounded to rounded, 0.02 - 0.05 mm	3%, micro- to meso- vesicles, and micro- to macro-vughs.	77% calcareous, heterogeneous from light brown to dark brown in PPL and golden orange to dark brown in XPL. Weak optical activity.	Two margins are visible: dark brown in PPL and ranging from dark red to brown in XPL. Weak optical activity.

	SP.10.2023	20% unimodal grain size distribution, equant and elongate, from sub-angular to rounded.	Dominant: quartz, equant and elongate, from sub-angular to rounded, 0.02-0.1 mm Frequent: mica, elongate, sub-angular to sub-rounded, 0.02-0.2 mm Common: nodules of iron oxides, equant and elongate, sub-rounded to rounded, 0.02 -0.4 mm	5%, micro- to meso- vesicles, and micro- to macro-vughs. Aligned to the margins of the section.	75% calcareous, heterogeneous from light brown to dark brown in PPL and golden orange to dark brown in XPL. Weak optical activity.	Two margins are visible: dark brown in PPL and ranging from dark red to brown in XPL. Very weak optical activity.
More micaceous fabric group 2	SP.01.2023	20%, unimodal grain size distribution, equant and elongate, from angular to rounded. Aligned to the margins of the section.	Dominant: quartz, equant and elongate, from angular to sub-rounded, 0.02-0.5 mm Frequent: mica, elongate, from sub-angular to sub-rounded, 0.02-0.1 mm Common: nodules of iron oxides, equant and elongate, sub-rounded to rounded, 0.02-0.3 mm Few: calcite crystals, elongate, sub-angular to sub-rounded, 0.02-0.05 mm	3%, mainly micro-vesicles and micro-vughs.	77% calcareous, heterogenous from light brown to dark brown in PPL and golden orange to brown in XPL. Weak optical activity.	A dark brown margin is visible in PPL, with a preparation layer underneath in a lighter yellow color (polishing). The same margin is yellow-red in XPL and is optically active.
	SP.02.2023	20%, unimodal grain size distribution, equant and elongate, from sub-angular to rounded. Slightly aligned to the margins of the section	Dominant: quartz, equant and elongate, from sub-angular to sub-rounded, 0.02-0.2 mm Frequent: mica, elongate, from sub-angular to sub-rounded, 0.02-0.1 mm Common: nodules of iron oxides, equant and elongate, sub-rounded to rounded, 0.02-0.5 mm	3%, micro- to meso-vesicles, and few micro- to meso-vughs. Secondary calcite.	77% calcareous, heterogeneous from light brown to dark brown in PPL and golden orange to brown in XPL. Moderate optical activity.	A dark brown margin is visible in PPL, and orange-red to brown in XPL. It is optically active. Secondary calcite.
	SP.03.2023	20% unimodal grain size distribution,	Dominant: quartz, equant and elongate, from sub-angular to rounded, 0.02-0.1 mm Frequent: mica, elongate, from sub-angular	3%, micro- to meso- vesicles, and micro- to meso-	77% calcareous, heterogeneous from light brown to dark	A dark brown margin is visible in PPL and ranges from dark red

		equant and elongate, from sub-angular to rounded. Aligned to the margins of the section.	to sub-rounded, 0.02-0.1 mm Common: nodules of iron oxides, equant and elongate, sub-rounded to rounded, 0.02-0.2 mm Very few: calcite crystals, equant and elongate, sub-angular to sub-rounded, 0.02-0.2 mm	vughs. Aligned to the margins of the section.	brown in PPL and golden orange to brown in XPL. Moderate optical activity.	to brown in XPL. It is optically active. Secondary calcite in one of the margins.
	SP.05.2023	30%, unimodal grain size distribution, equant and elongate, from sub-angular to rounded.	Dominant: quartz, equant and elongate, from sub-angular to sub-rounded, 0.02-0.2 mm. Frequent: mica, elongate, from sub-angular to rounded, 0.02-0.1 mm Common: nodules of iron oxides, equant and elongate, sub-rounded to rounded, 0.02-0.1 mm Very few: microcline, elongate, sub-rounded, 0.1 mm	3%, micro vesicles and micro- to meso-vughs.	67% calcareous, heterogeneous from light brown to dark brown in PPL and golden orange to dark brown in XPL. Weak optical activity.	A visible margin ranges from dark brown to orange-brown in PPL and from dark red to golden orange in XPL. It is optically active. Secondary calcite.
	SP.09.2023	20% unimodal grain size distribution, equant and elongate, from sub-angular to rounded.	Dominant: quartz, equant and elongate, from sub-angular to rounded, 0.02-0.1 mm Frequent: mica, elongate, sub-angular to sub-rounded, 0.02-0.2 mm Common: nodules of iron oxides, equant and elongate, sub-rounded to rounded, 0.02-0.2 mm	3%, micro- to meso- vesicles, and micro- to meso-vughs.	77% calcareous, heterogeneous from light brown to dark brown in PPL and golden orange to dark brown in XPL. Weak optical activity. Dark area on the margin of the section.	Two margins are visible: dark brown in PPL and ranging from dark red to brown in XPL. Secondary calcite. Weak optical activity.
	SP.11.2023	30% unimodal grain size distribution,	Dominant: quartz, equant and elongate, from sub-angular to rounded, 0.02-0.1 mm Frequent: mica, elongate, sub-angular to	5% micro- to meso- vesicles and micro- to meso-	65% calcareous, heterogeneous from light brown to dark	Two margins are visible, dark brown in PPL and ranging from

		equant and elongate, from sub-angular to rounded.	sub-rounded, 0.02-0.3 mm Common: nodules of iron oxides, equant and elongate, sub-rounded to rounded, 0.02-0.1 mm Rare: micritic calcite, equant, rounded, 0.02 -0.2 mm	vughs. Secondary calcite along the margins of the voids. Aligned to margins of the section.	brown in PPL and golden orange to dark brown in XPL. Weak optical activity.	dark red to vivid orange in XPL. Moderate optical activity.
	SP.12.2023	30% unimodal grain size distribution, equant and elongate, from sub-angular to rounded.	Dominant: quartz, equant and elongate, from sub-angular to rounded, 0.02-0.3 mm Dominant: mica, elongate, sub-angular to sub-rounded, 0.02-0.1 mm Common: nodules of iron oxides, equant and elongate, sub-rounded to rounded, 0.02 - 0.2 mm Very rare: microcline, elongate, sub-rounded, 0.3 mm	3%, micro- to meso- vesicles, and micro- to meso-vughs. Micritic calcite has partially infilled some voids.	67% calcareous, heterogeneous from light brown to dark brown in PPL and golden orange to dark brown in XPL. Some areas are darker grey-black. Weak optical activity.	Two margins are visible: dark brown in PPL and dark red to red-orange in XPL. Moderate optical activity.
	SP.13.2023	20% unimodal grain size distribution, equant and elongate, from sub-angular to rounded.	Dominant: quartz, equant and elongate, from sub-angular to rounded, 0.02-0.1 mm Frequent: mica, elongate, sub-angular to sub-rounded, 0.02-0.2 mm Common: nodules of iron oxides, equant and elongate, sub-rounded to rounded, 0.02 -0.1 mm Rare: feldspars, elongate, rounded, 0.2 mm.	3%, micro- to meso- vesicles, and micro- to meso-vughs.	77% calcareous, heterogeneous from light brown to dark brown in PPL and XPL. Very weak optical activity.	Two margins are visible, dark brown in PPL and ranging from dark red to vivid orange in XPL. Moderate optical activity

	SP.14.2023	20% unimodal grain size distribution, equant and elongate, from sub-angular to rounded.	Dominant: quartz, equant and elongate, from sub-angular to rounded, 0.02-0.1 mm Frequent: mica, elongate, sub-angular to sub-rounded, 0.02-0.1 mm Common: nodules of iron oxides, equant and elongate, sub-rounded to rounded, 0.02-0.2 mm	3%, micro- to meso- vesicles, and micro- to meso-vughs. Aligned to the margins of the section.	77% calcareous, heterogeneous from light brown to dark brown in PPL and XPL. Very weak optical activity.	The margins that compose the slip are not so well defined. They range from dark brown in PPL to orange-brown in XPL. Weak optical activity.
Loners	SP.07.2023	10% unimodal grain size distribution, equant and elongate, from sub-angular to rounded.	Dominant: quartz, equant and elongate, from sub-angular to rounded, 0.02-0.1 mm Frequent: mica, elongate, from sub-angular to rounded, 0.02-0.1 mm Common: nodules of iron oxides, equant and elongate, sub-rounded to rounded, 0.02-0.1 mm	3%, micro- to meso- vesicles, and micro- to macro-vughs. Aligned to the margins of the section.	87% calcareous, homogeneous, light brown in PPL and from deep orange to brown in XPL. Weak optical activity.	Two margins are visible, dark brown in PPL and ranging from brown to orange-brown in XPL. Weak optical activity.
	SP.15.2023	20% unimodal grain size distribution, equant and elongate, from sub-angular to rounded.	Dominant: quartz, equant and elongate, from sub-angular to rounded, 0.02-0.1 mm Frequent: mica, elongate, sub-angular to sub-rounded, 0.02-0.1 mm Common: nodules of iron oxides, equant and elongate, sub-rounded to rounded, 0.02-0.6 mm	3%, micro- to meso- vesicles, and micro- to meso-vughs. Secondary calcite along the margins.	77% calcareous, heterogeneous from light brown to dark brown in PPL and golden orange to dark brown in XPL. Some areas are darker grey-black. Weak optical activity	The margins of the slip are not well defined; they range from dark to light brown in PPL and XPL. No optical activity.

3.2 Scanning Electron Microscopy – Energy Dispersive X-ray Spectroscopy (SEM-EDS)

Representative samples of the groups identified by OM have been analyzed by SEM-EDS to obtain qualitative information regarding their chemical composition and surface topography. SEM-EDS analysis largely confirmed OM investigations.

Less micaceous fabric group 1

Sample SP.04.2023 belongs to the less micaceous fabric group 1. Figure 53 shows that the inclusions are quartz, biotite, and K-feldspar. In addition, the matrix consists of high amounts of Si, minor amounts of C, Ca, Al, O, and traces of Na, Mg, Fe, F, and K. Finally, the slip is composed of one layer with high amounts of Si, Al, O, minor of K, Mg, Fe, and traces of C, Na, and F.

Figure 53. Backscattered electron image of sample SP.04.2023 and EDS spectra collected on various inclusions and on the slip.

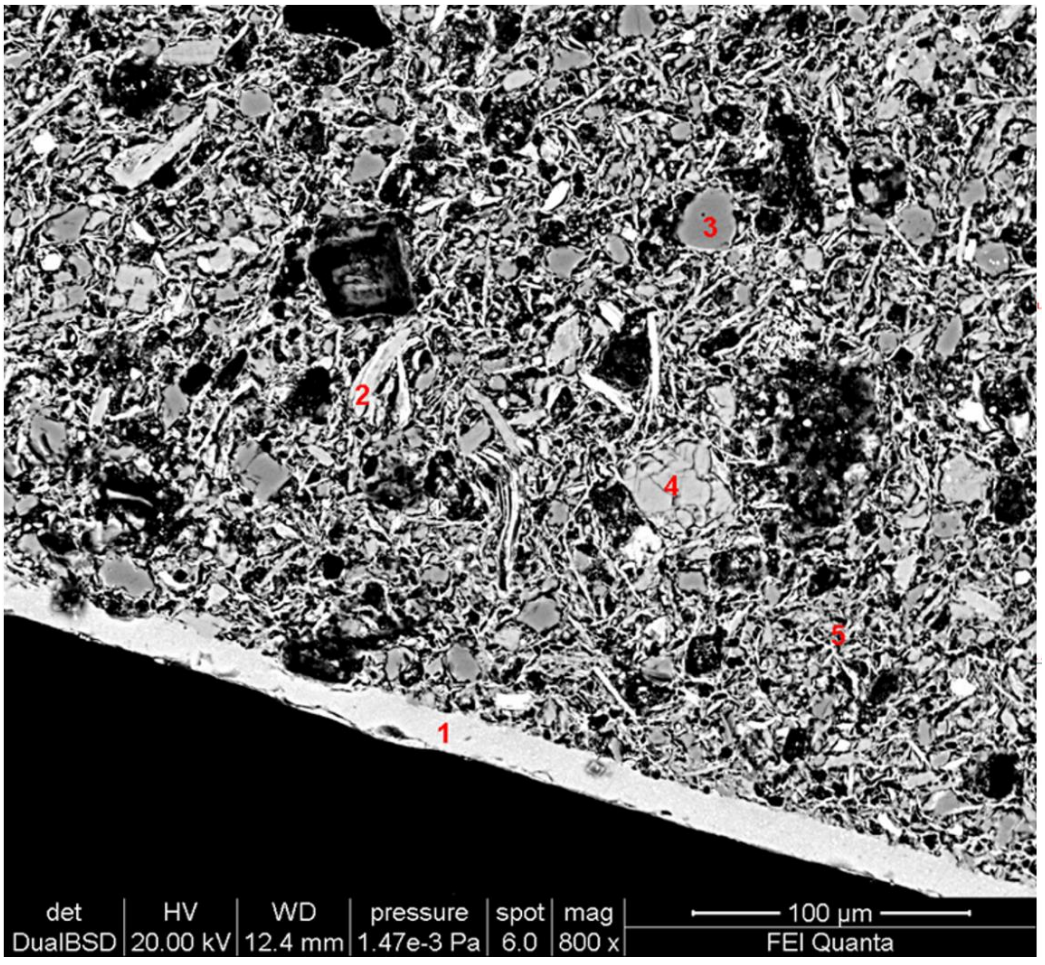

Point 1 - Slip

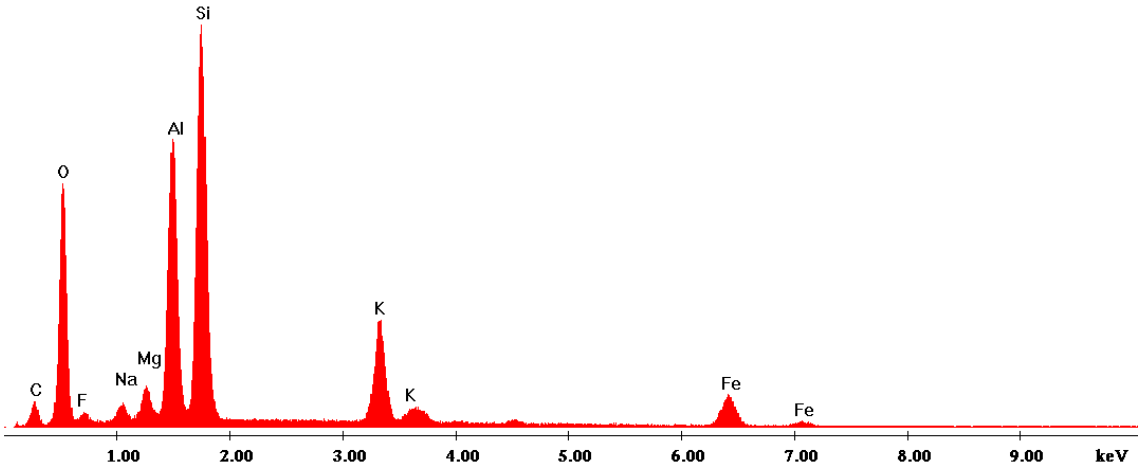

Point 2 - Biotite

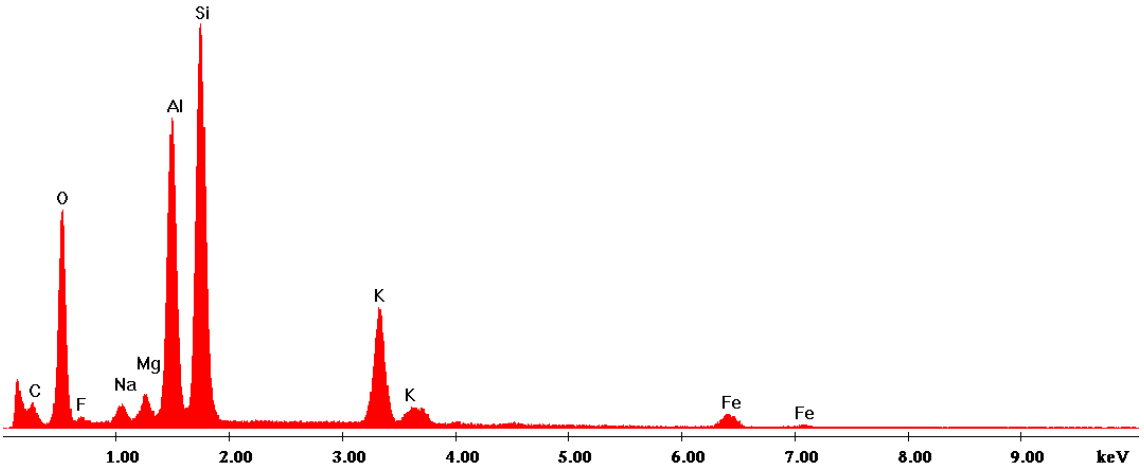

Point 3 - Quartz

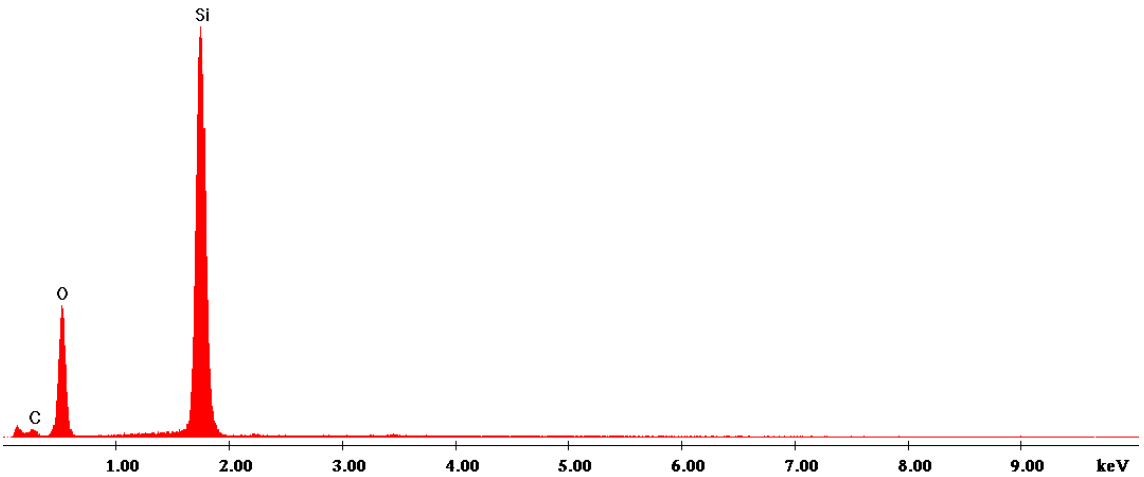

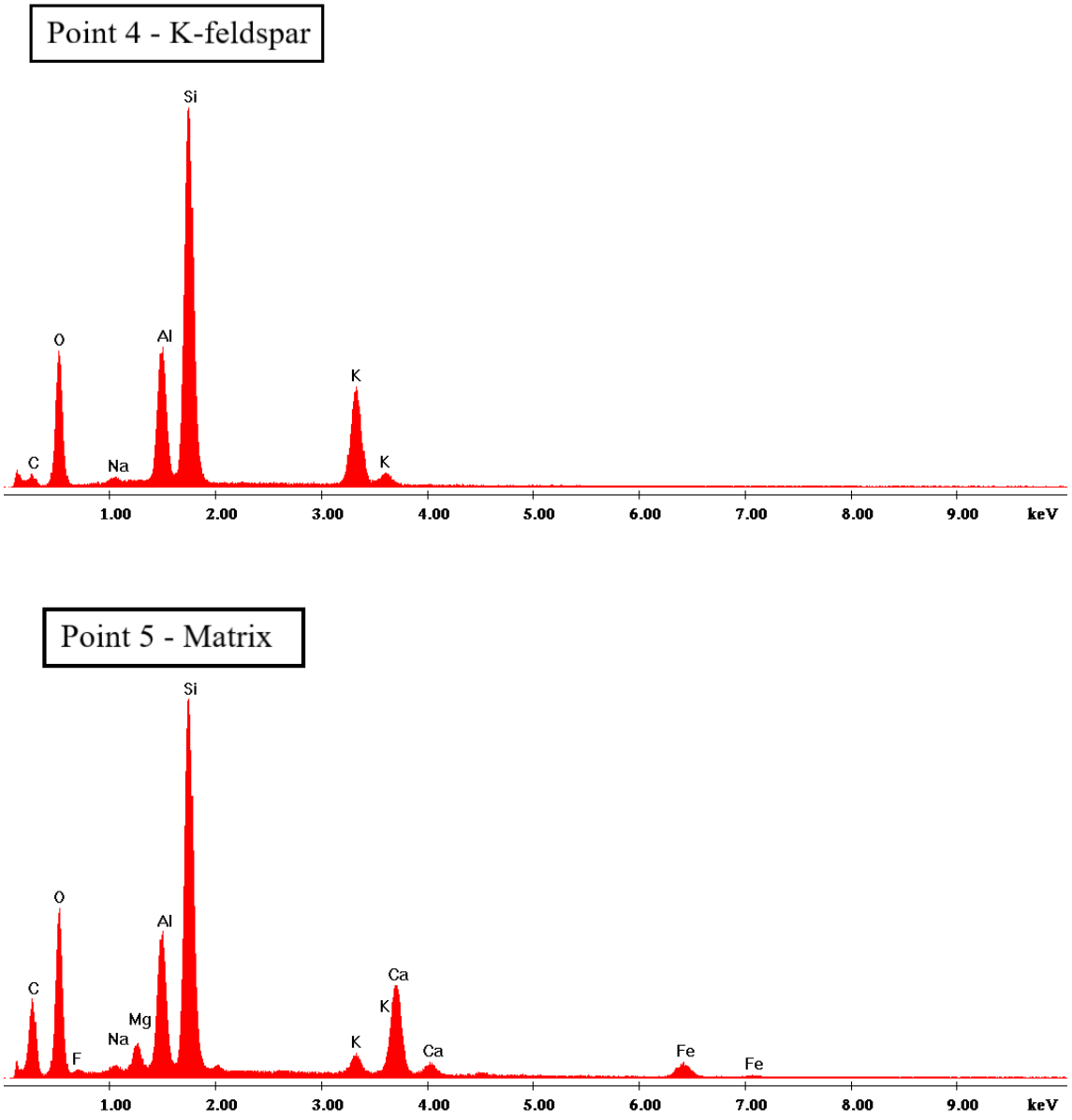

More micaceous fabric group 2

Sample SP.01.2023 belongs to the more micaceous fabric group 2. Figures 54 and 55 show that the inclusions are calcite, quartz, plagioclase, biotite, and clay pellets. Additionally, the matrix is mainly composed of Si and O, minor of Al, Ca, and C, and traces of Na, Mg, K, and Fe. Lastly, the slip is composed of one layer with a high amount of Si, Al, O, minor of C, Mg, K, Fe, and traces of Na and F.

Figure 54. Backscattered electron image of the sample SP.01.2023 EDS spectra collected on various inclusions.

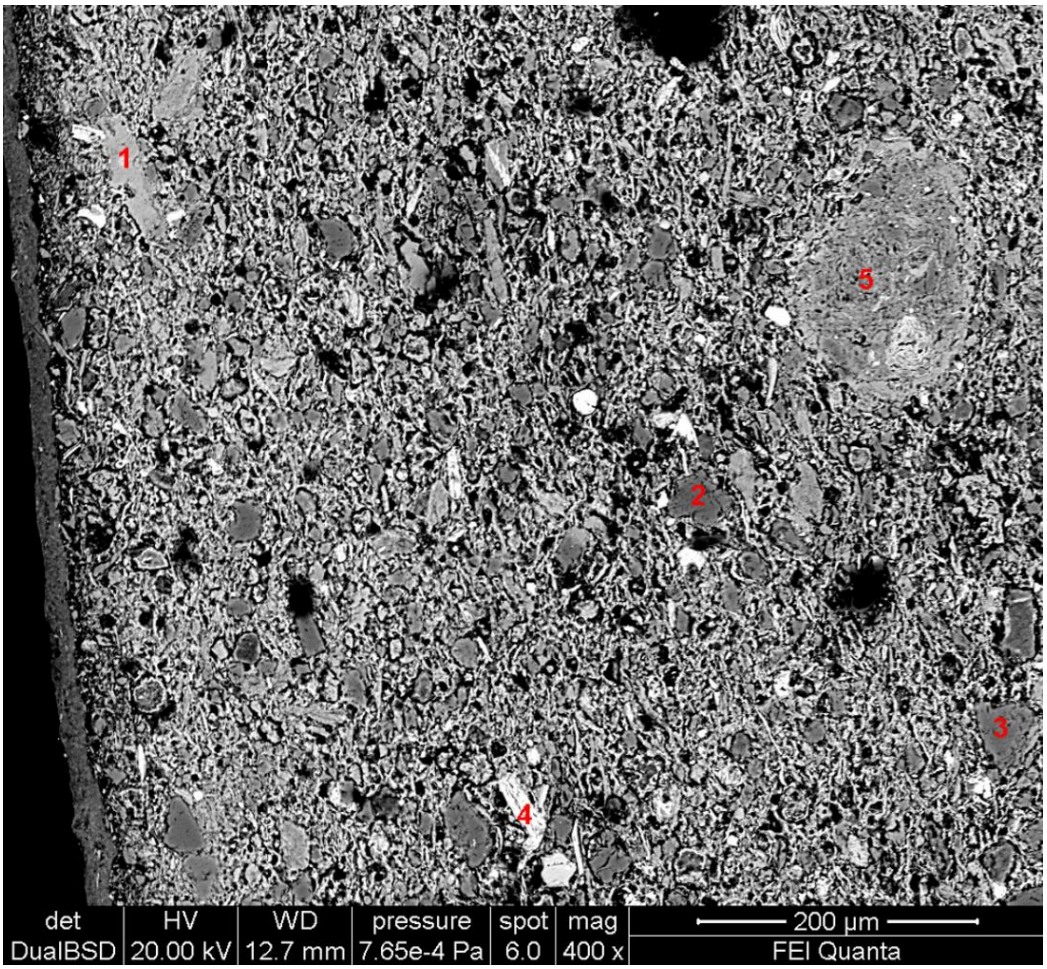
1
2
3
4
5
det
DualBSD
HV
20.00 kV
WD
12.7 mm
pressure
7.65e-4 Pa
spot
6.0
mag
400 x
200 µm
FEI Quanta

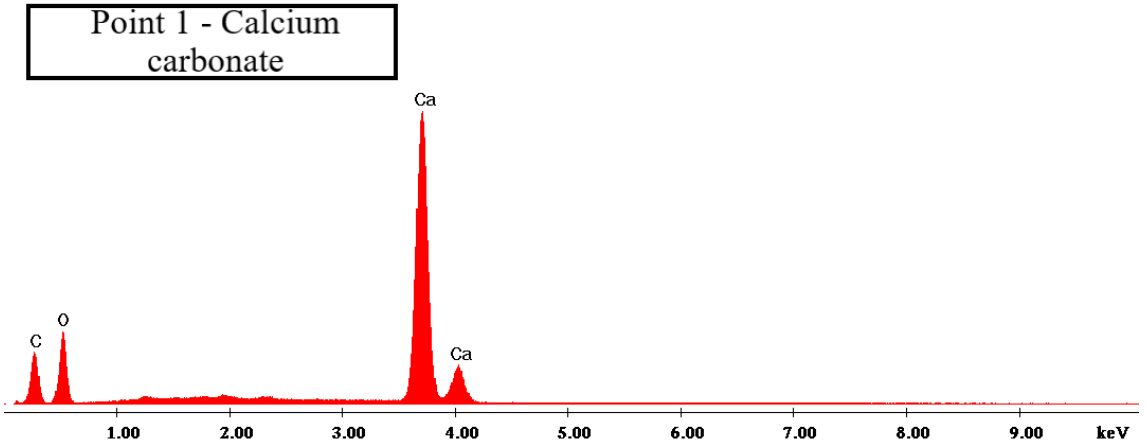
Point 1 - Calcium carbonate
Ca
O
C
Ca
1.00
2.00
3.00
4.00
5.00
6.00
7.00
8.00
9.00
keV

Point 2 - Quartz

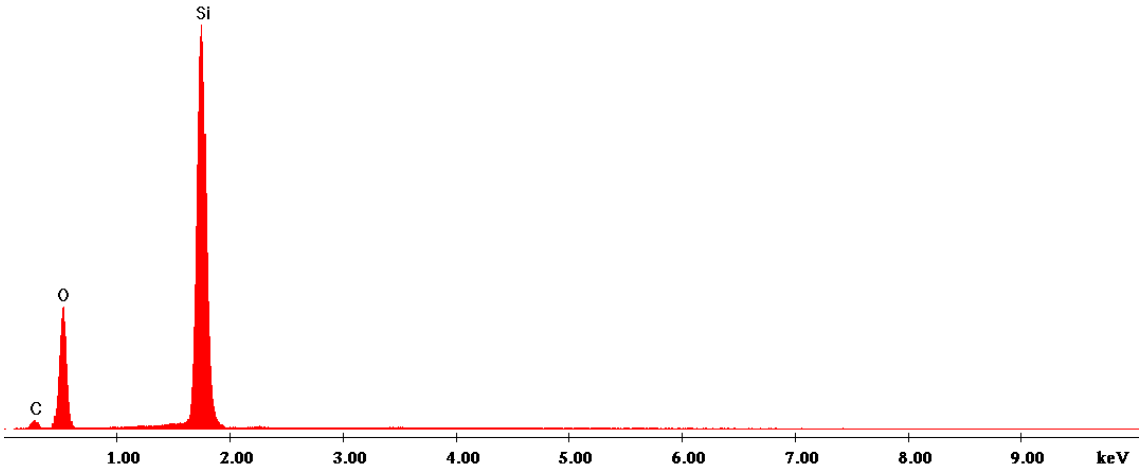

Point 3 - Plagioclase

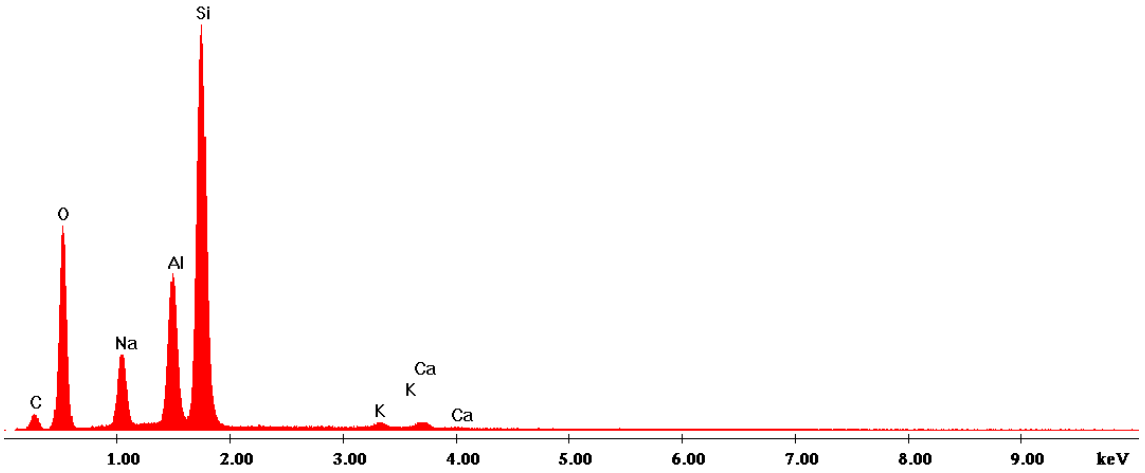

Point 4 - Biotite

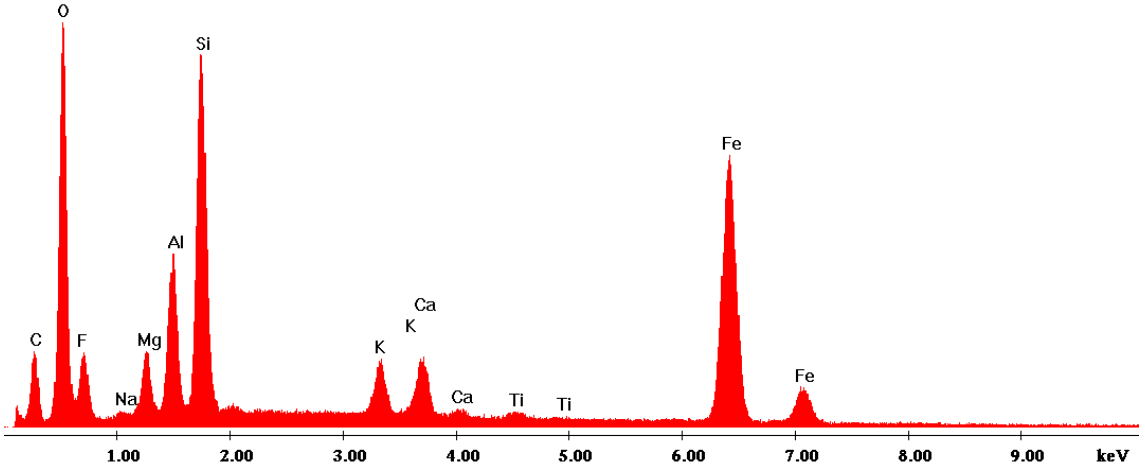

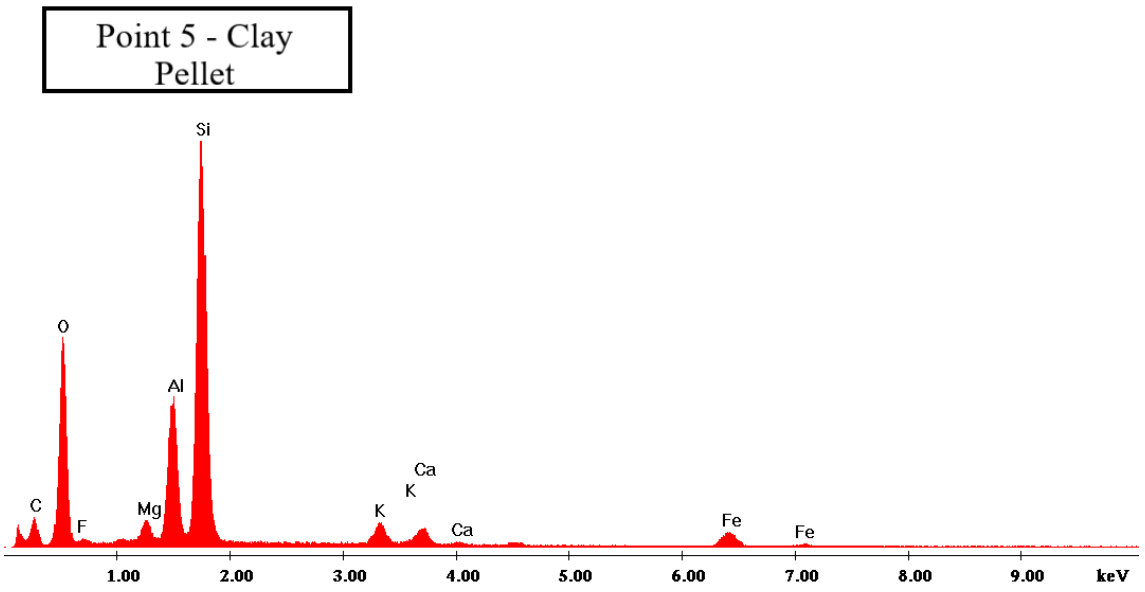

Figure 55. Backscattered electron image of the sample SP.01.2023 and EDS spectra collected on various inclusions and on the slip.

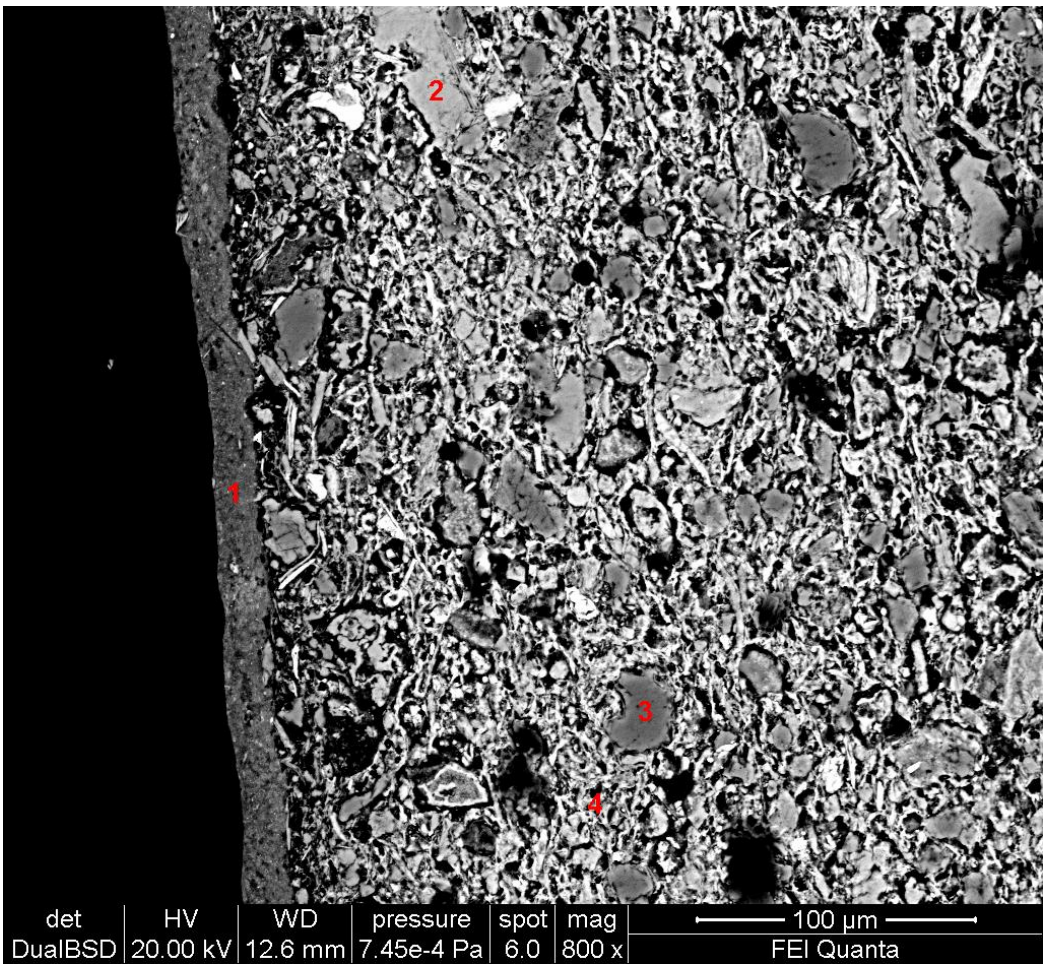

Point 1- Slip

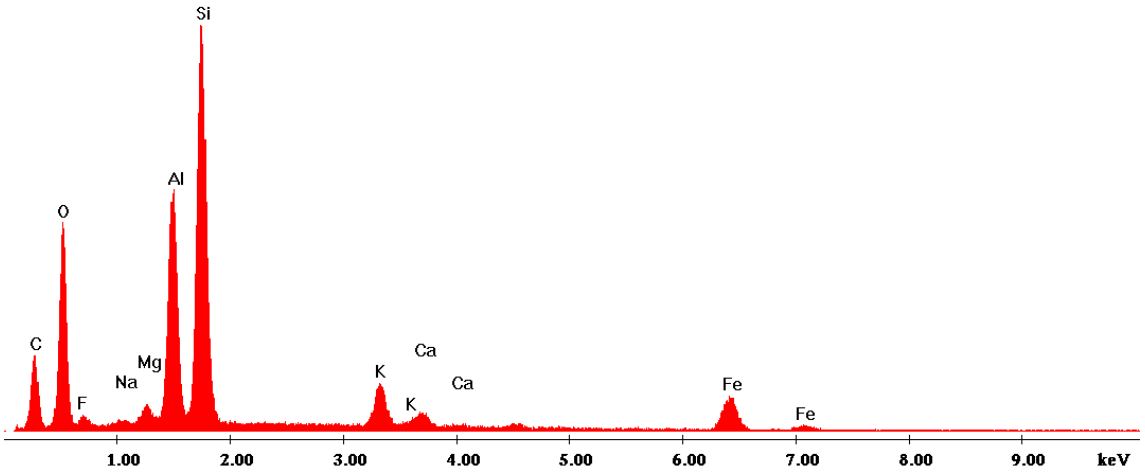

Point 2 - Calcite

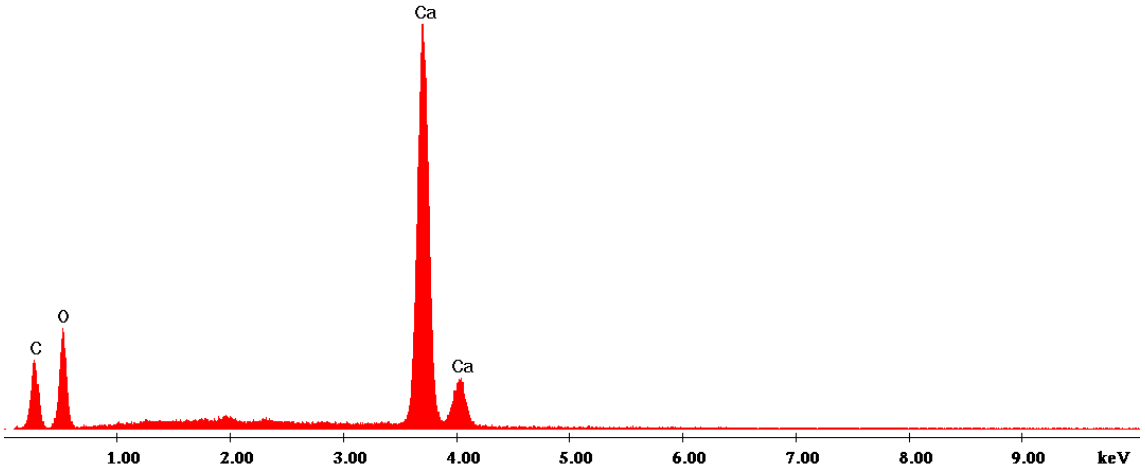

Point 3 - Quartz

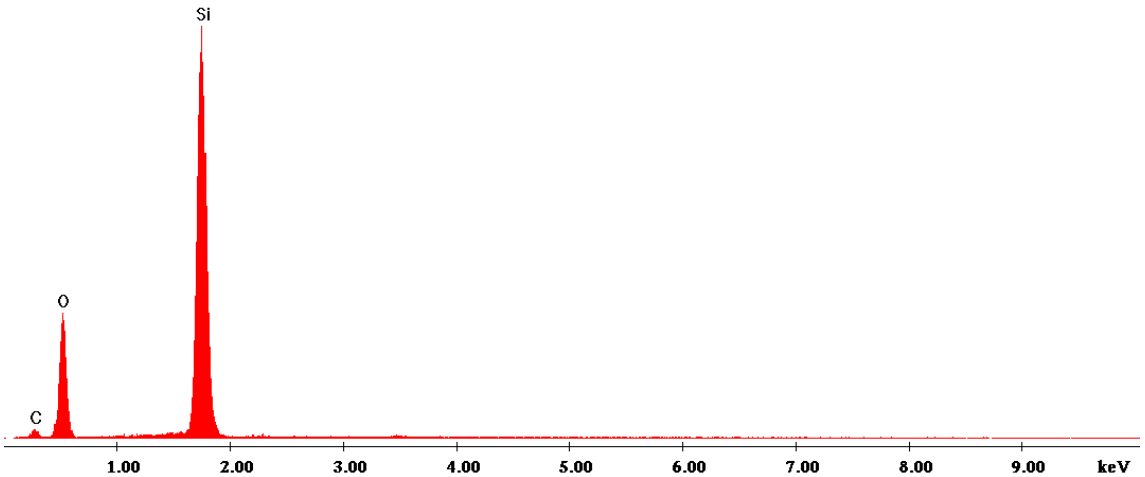

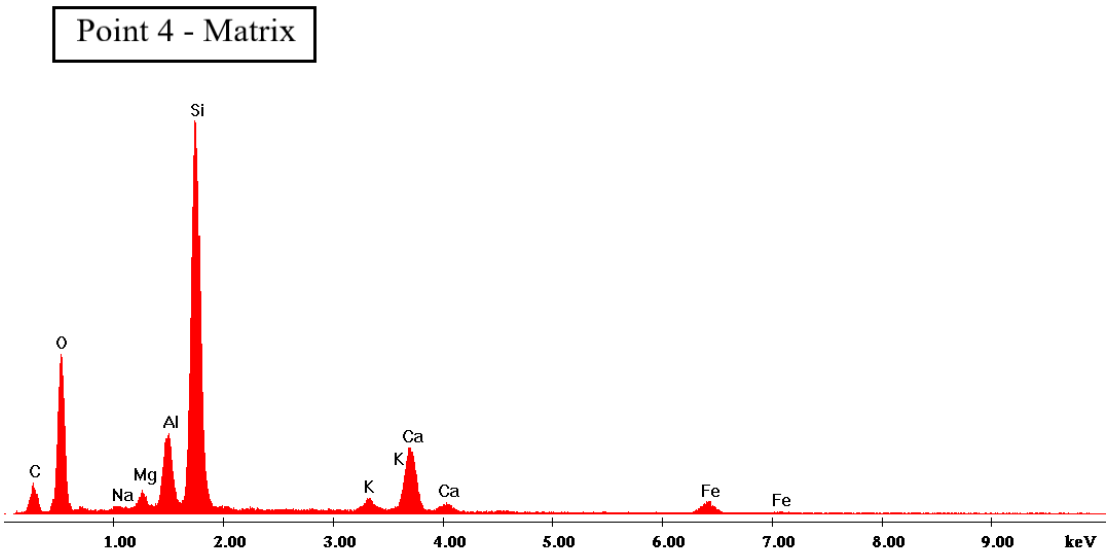

Sample SP.05.2023 also belongs to the more micaceous fabric group 2. Figures 56 and 57 indicate that the inclusions are K-feldspar, quartz, titanium oxide, and iron oxide. Additionally, the matrix mainly comprises Si, O, lower amounts of C, Al, and Ca, and traces of Na, Mg, K, and Fe. The slip is composed of two layers: an external layer with a high amount of Ca, P, Si, O lower of Al, C, traces of F, Mg, K, Fe, and an internal layer with a high amount of Si, Al, O, minor of K, and traces of C, Na, Mg, Fe.

Figure 56. Backscattered electron image of sample SP.05.2023 and EDS spectra collected on various inclusions and on the slip.

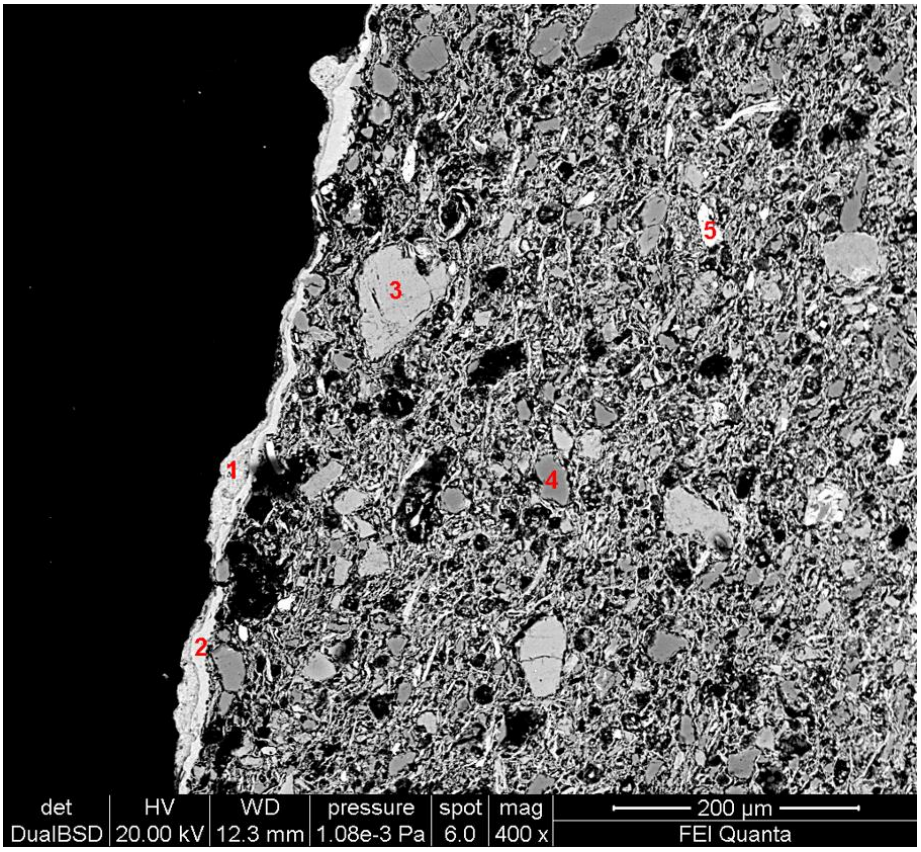

Point 1 - External layer of slip

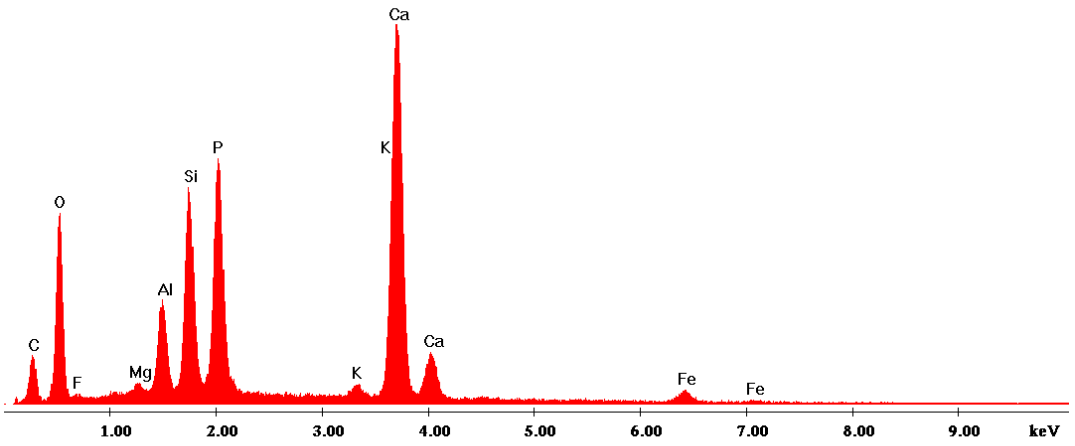

Point 2 - Internal layer of slip

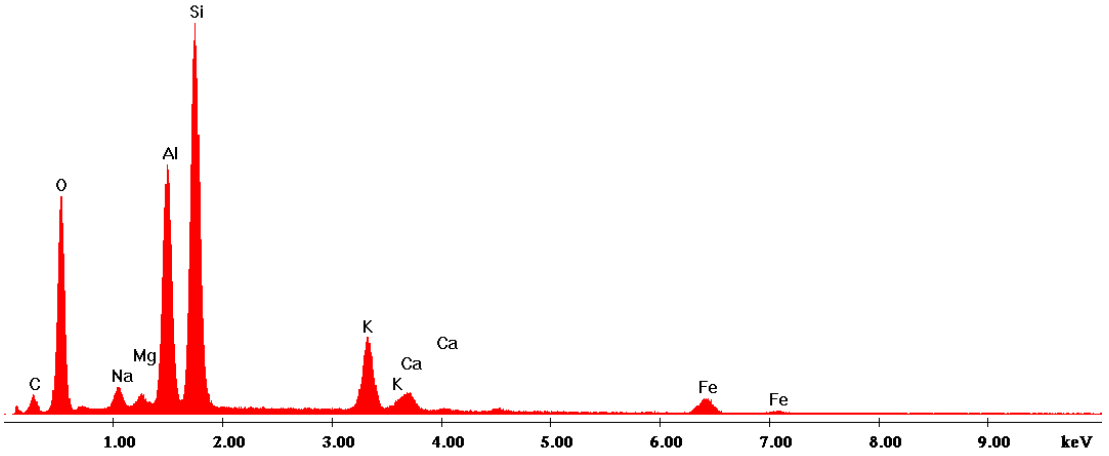

Point 3 - K-feldspar

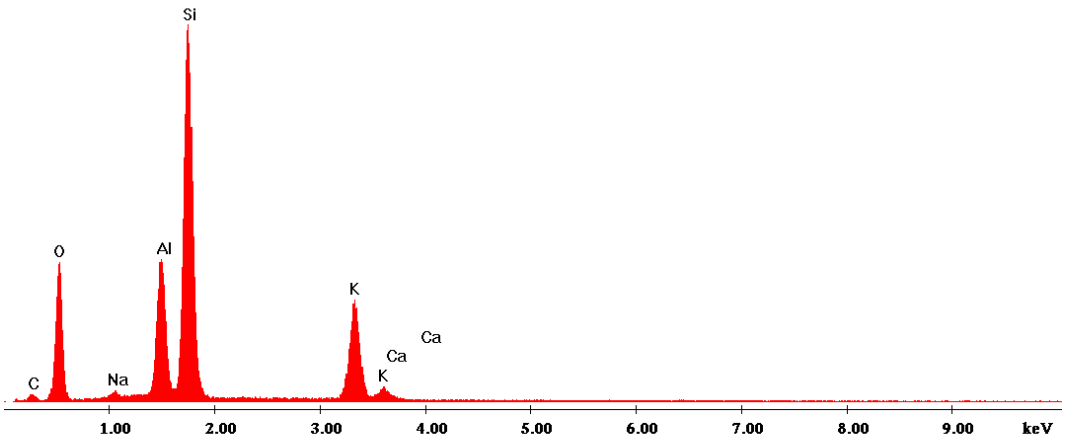

Point 4 - Quartz

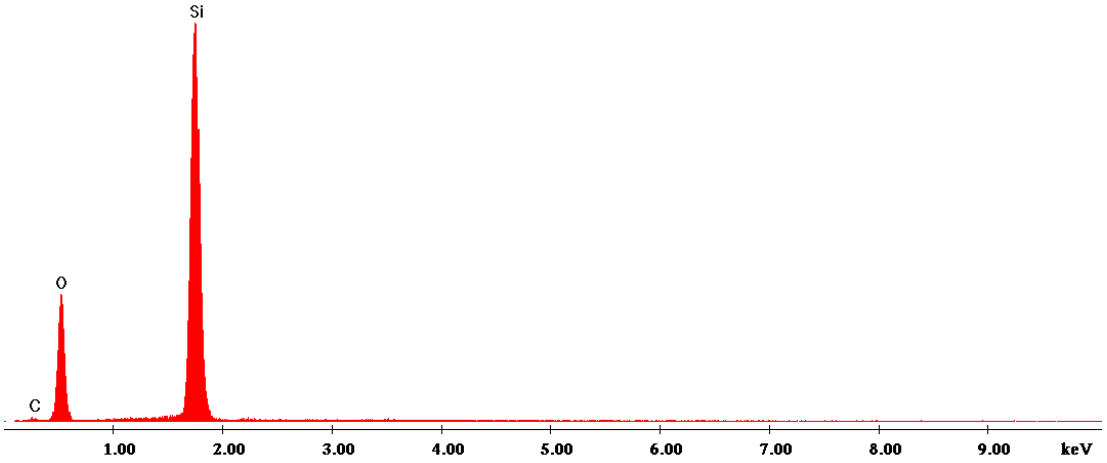

Point 5 - Titanium oxide

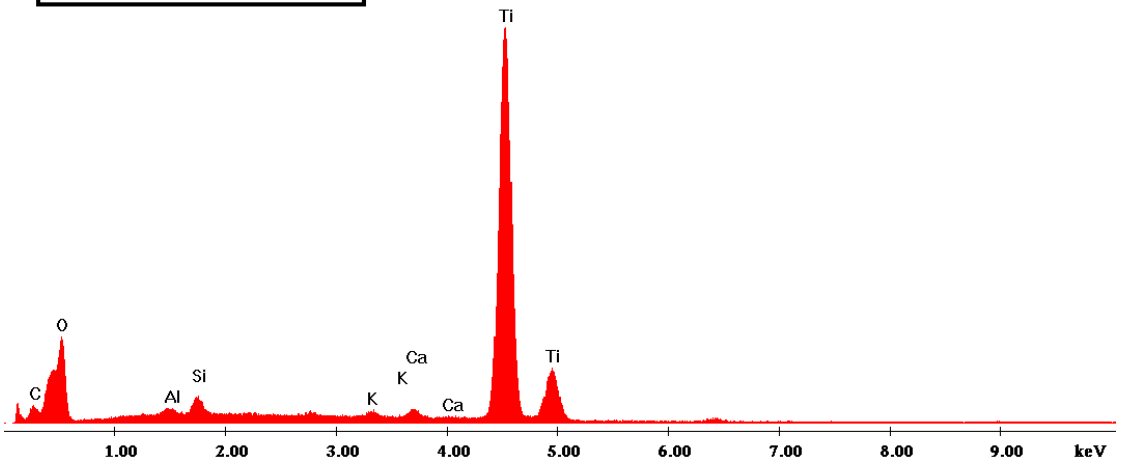

Figure 57. Backscattered electron image of sample SP.05.2023 and EDS spectra collected on an inclusion and on the matrix.

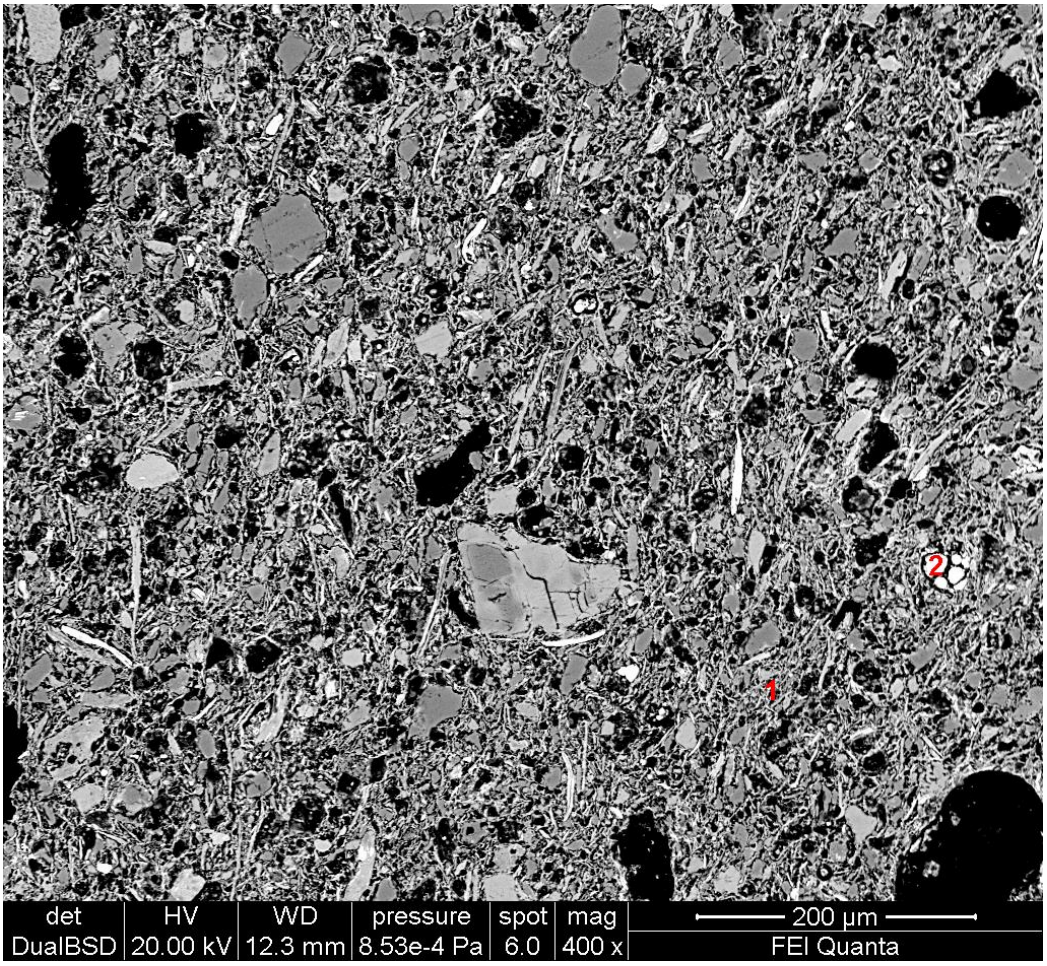

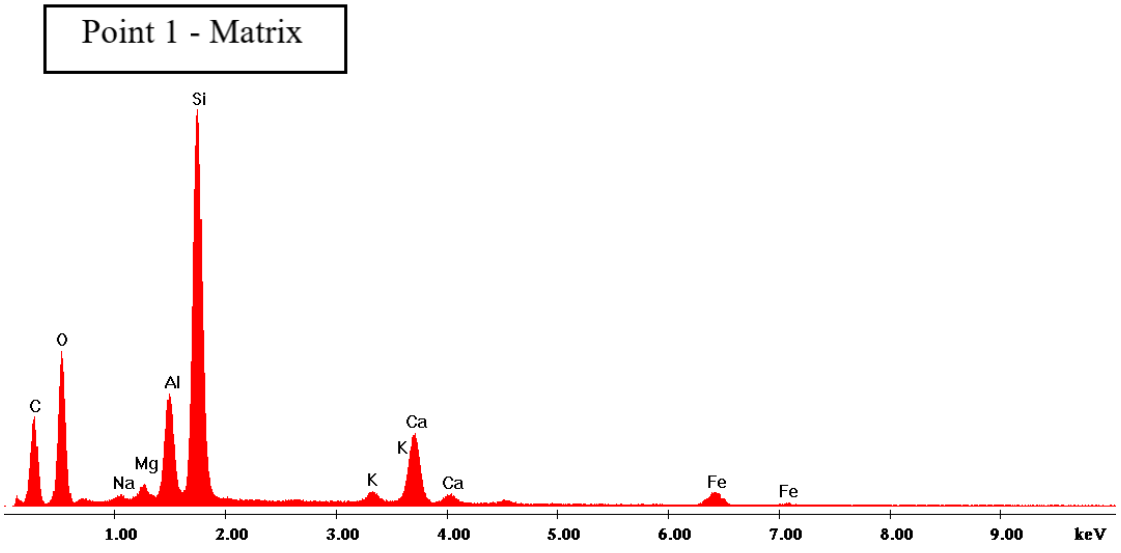

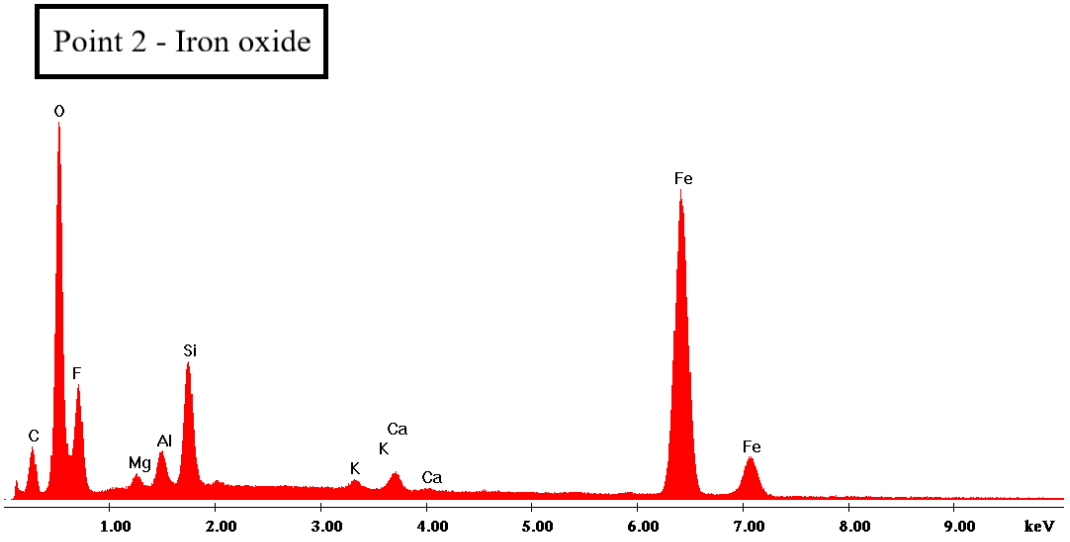

Loners

Sample SP.07.2023 is a loner. Figures 58 and 59 show that the inclusions are K-feldspar, quartz, iron oxides, and biotite. The matrix mainly comprises Si, Al, C, O, minor amounts of Ca, and traces of Na, Mg, K, and Fe. The slip is composed of one layer with a high amount of Si, Al, O, lower of C, K, and traces of F, Na, Mg, Ca, and Fe.

Figure 58. Backscattered electron image of sample SP.07.2023 and EDS spectra collected on various inclusions and on the matrix.

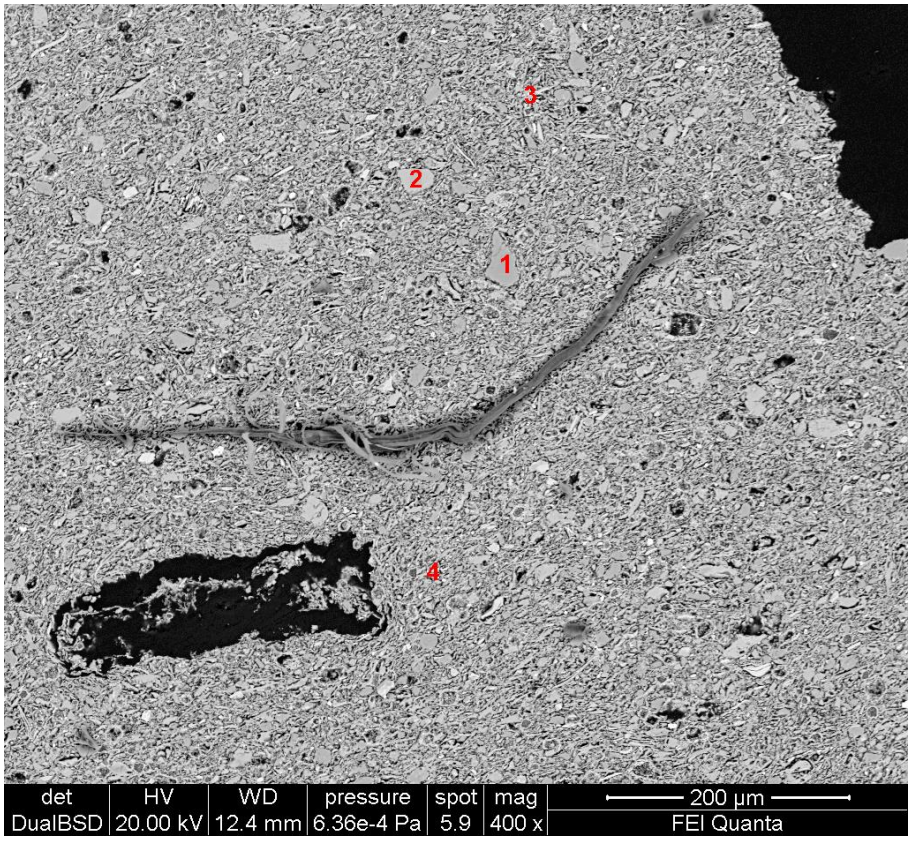

Point 1 - K-feldspar

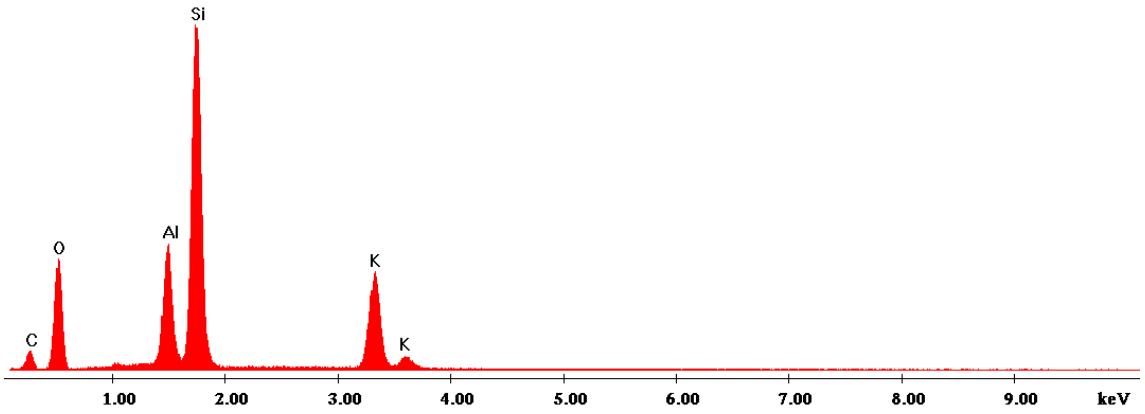

Point 2 - Quartz

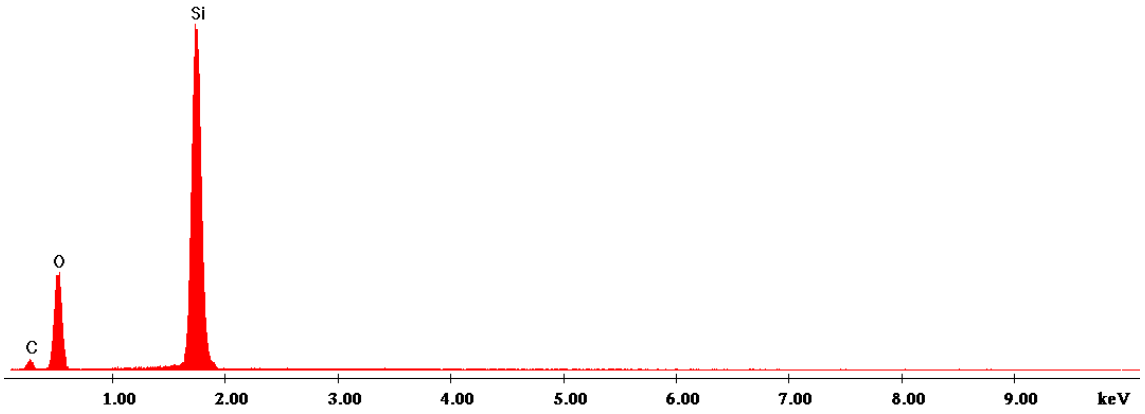

Point 3 - Biotite

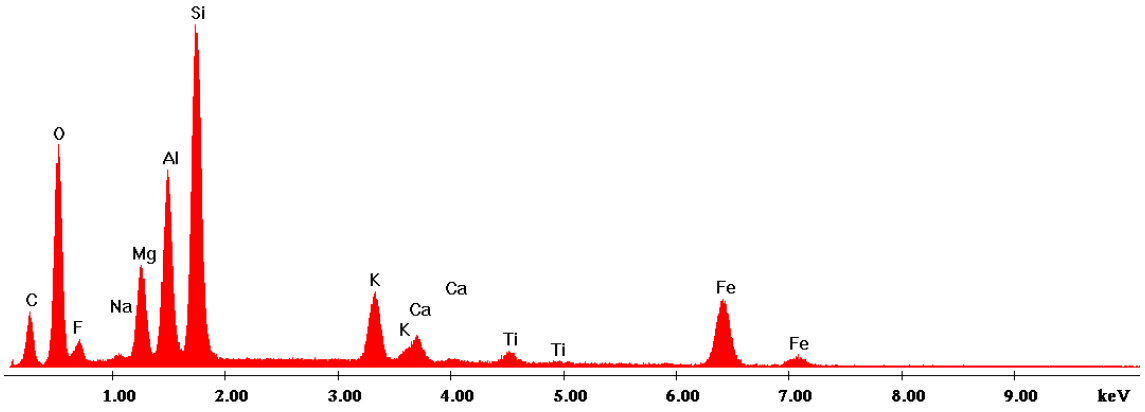

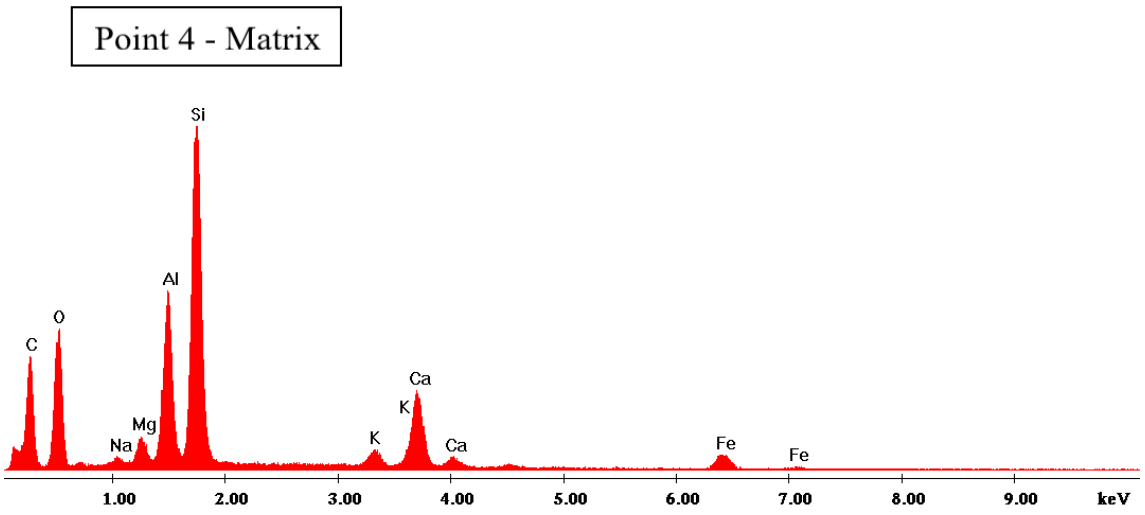

Figure 59. Backscattered electron image of sample SP.07.2023 and EDS spectra collected on an inclusion and on the slip.

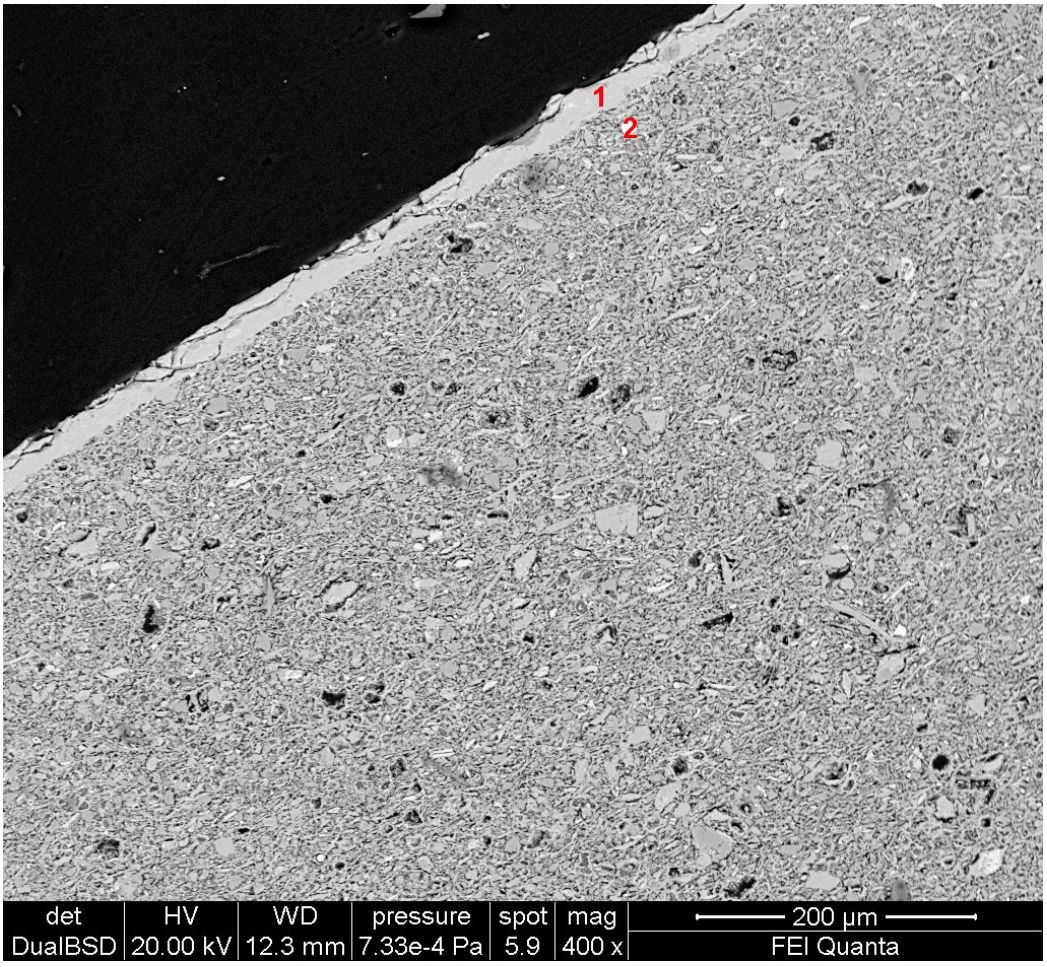

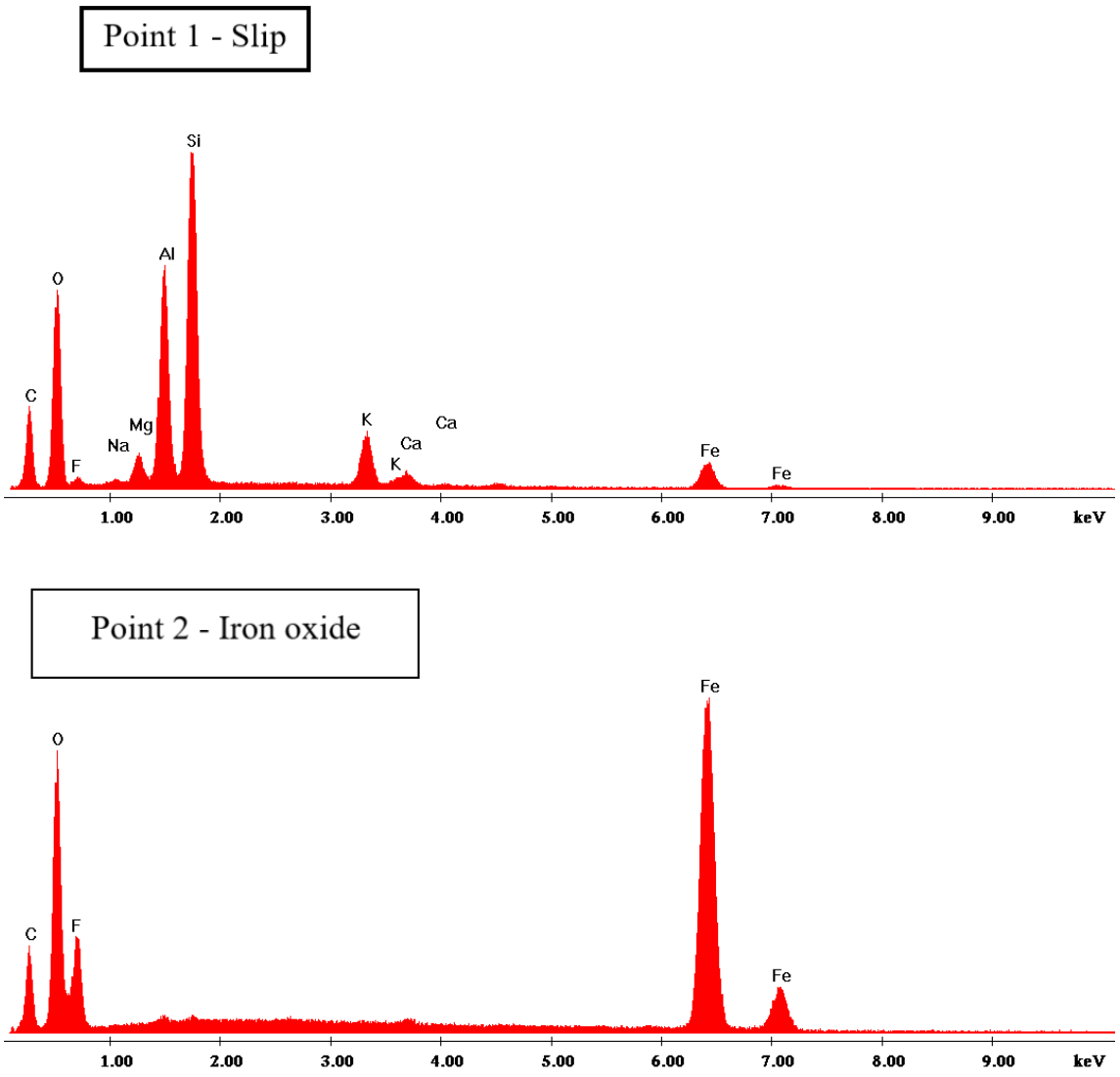

Sample SP.15.2023 is a loner. Figures 60 and 61 show that the inclusions are calcareous microfossils, K-feldspar, quartz, biotite, iron oxides, and calcium carbonates. The matrix comprises mainly Si, O, minor amounts of C, Al, and Ca, and traces of Mg, K, Fe, F, and P. The slip is composed of one layer with a high amount of Si, O, Ca, minor of Al, P, C, and traces of F, Na, Mg, K, Ti, and Fe.

Figure 60. Backscattered electron image of sample SP.15.2023 and EDS spectra collected on various inclusions and on the matrix.

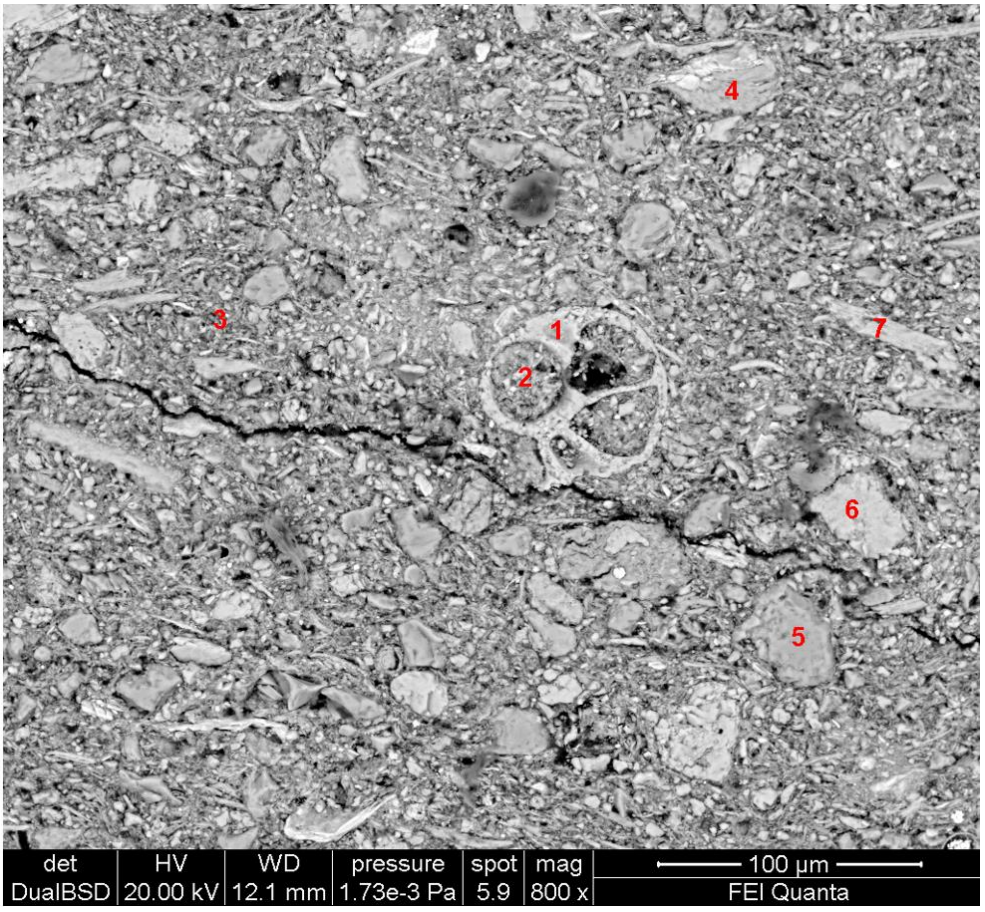
4
3
1
2
7
6
5
det
DualBSD
HV
20.00 kV
WD
12.1 mm
pressure
1.73e-3 Pa
spot
5.9
mag
800 x
100 µm
FEI Quanta

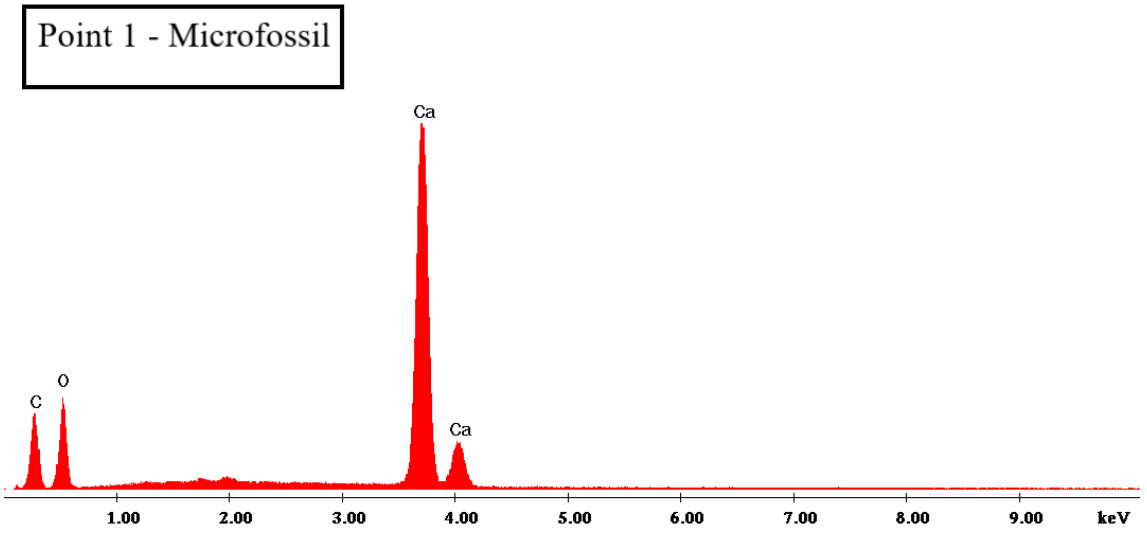
Point 1 - Microfossil
Ca
O
C
Ca
1.00
2.00
3.00
4.00
5.00
6.00
7.00
8.00
9.00
keV

Point 2 - Matrix within the microfossil

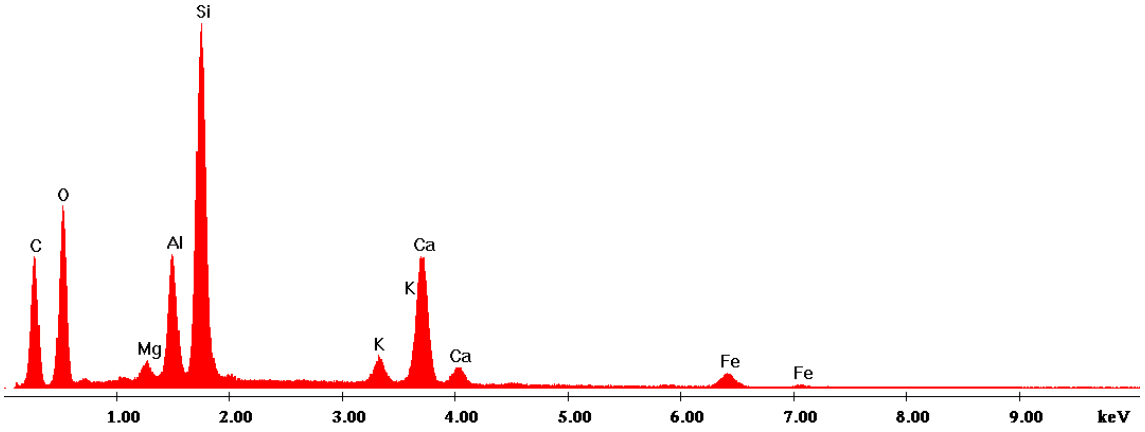

Point 3 - Matrix on the exterior of the microfossil

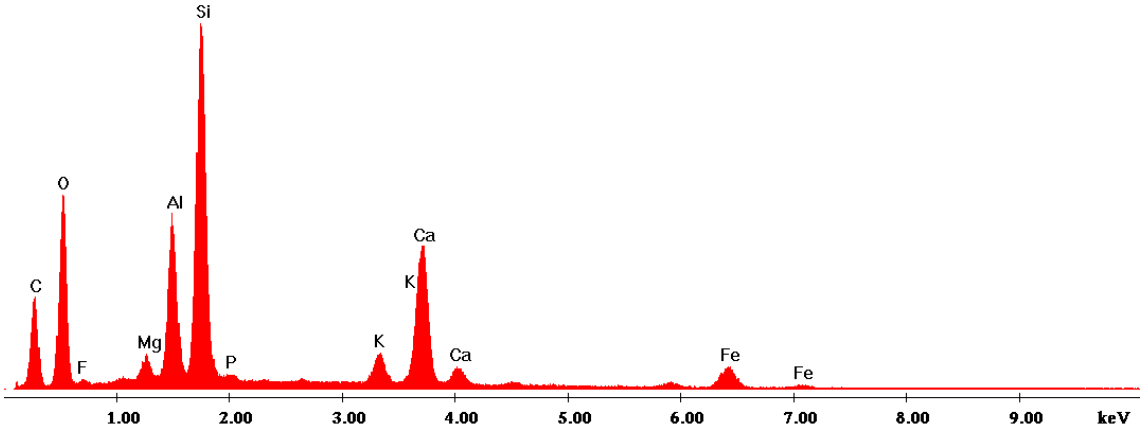

Point 4 - K-feldspar

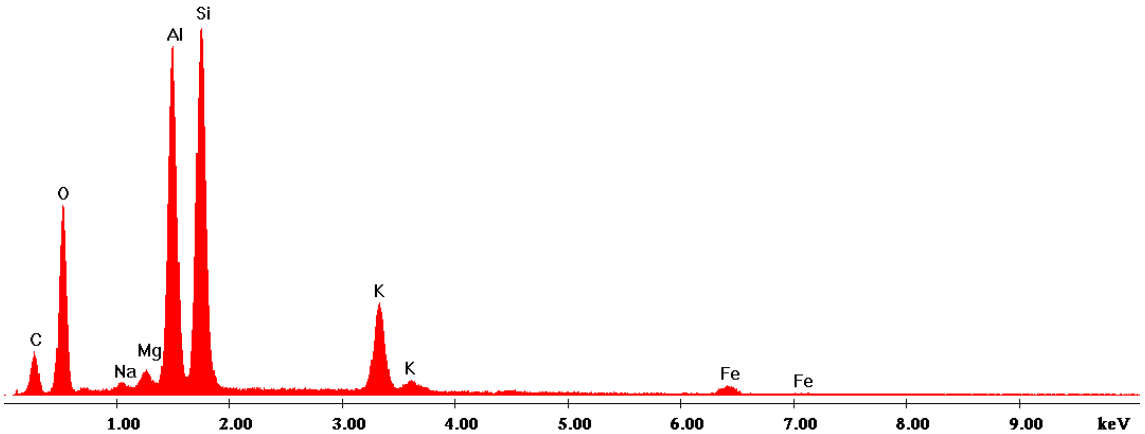

Point 5 - Quartz

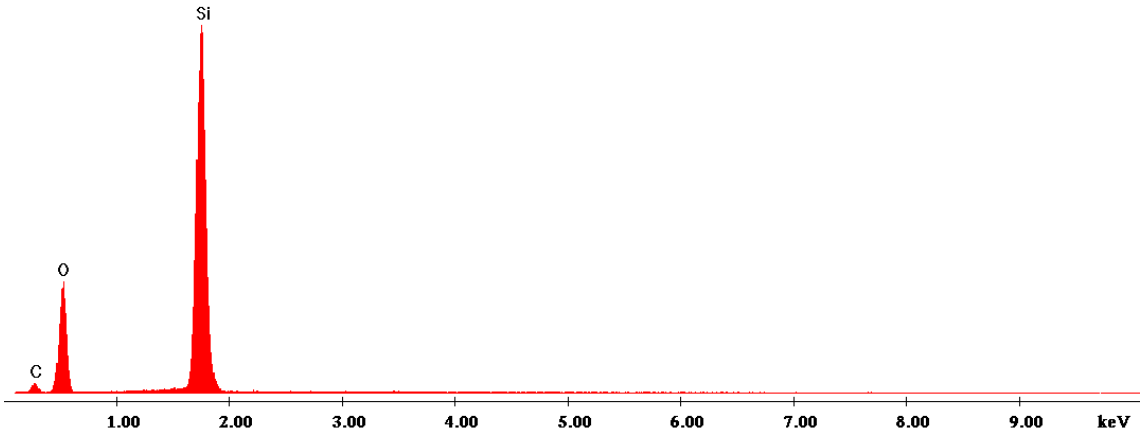

Point 6 - Calcium carbonate

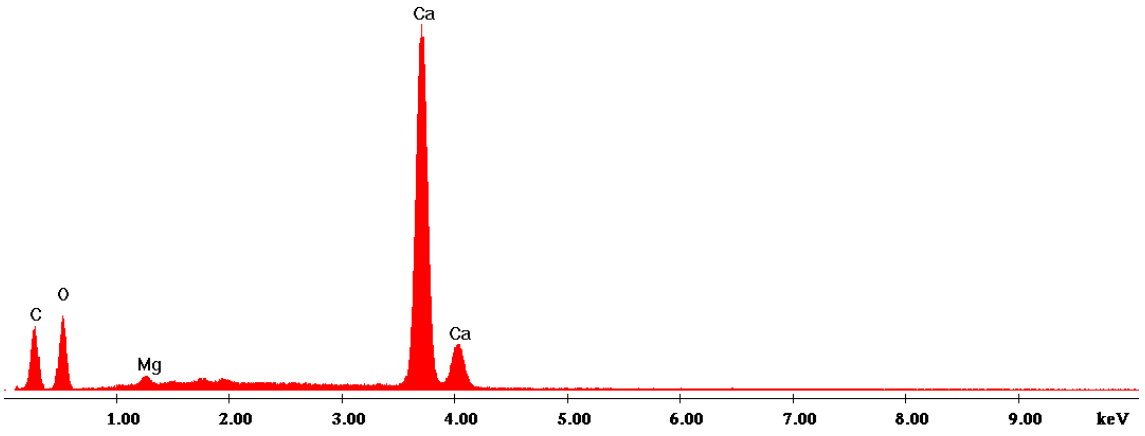

Point 7 - Biotite

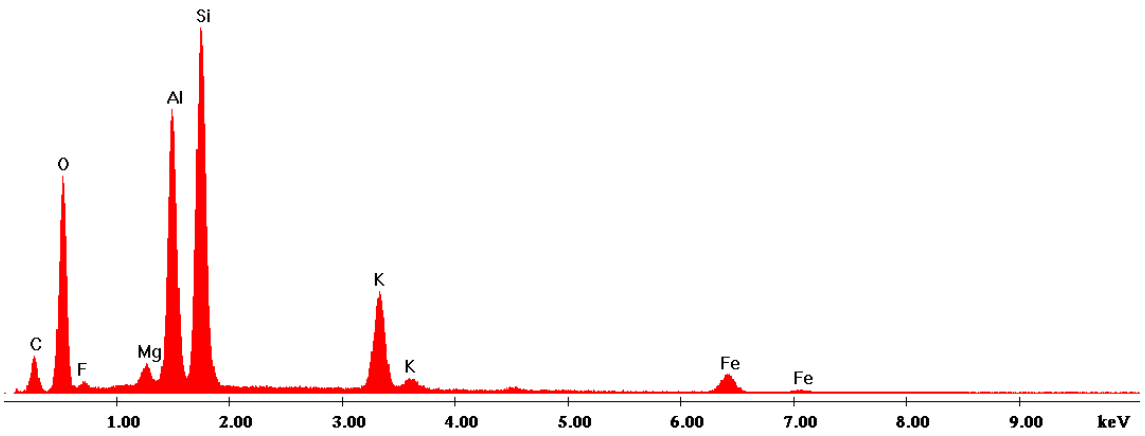

Figure 61. Backscattered electron image of sample SP.15.2023 and EDS spectra collected on an inclusion and on the slip.

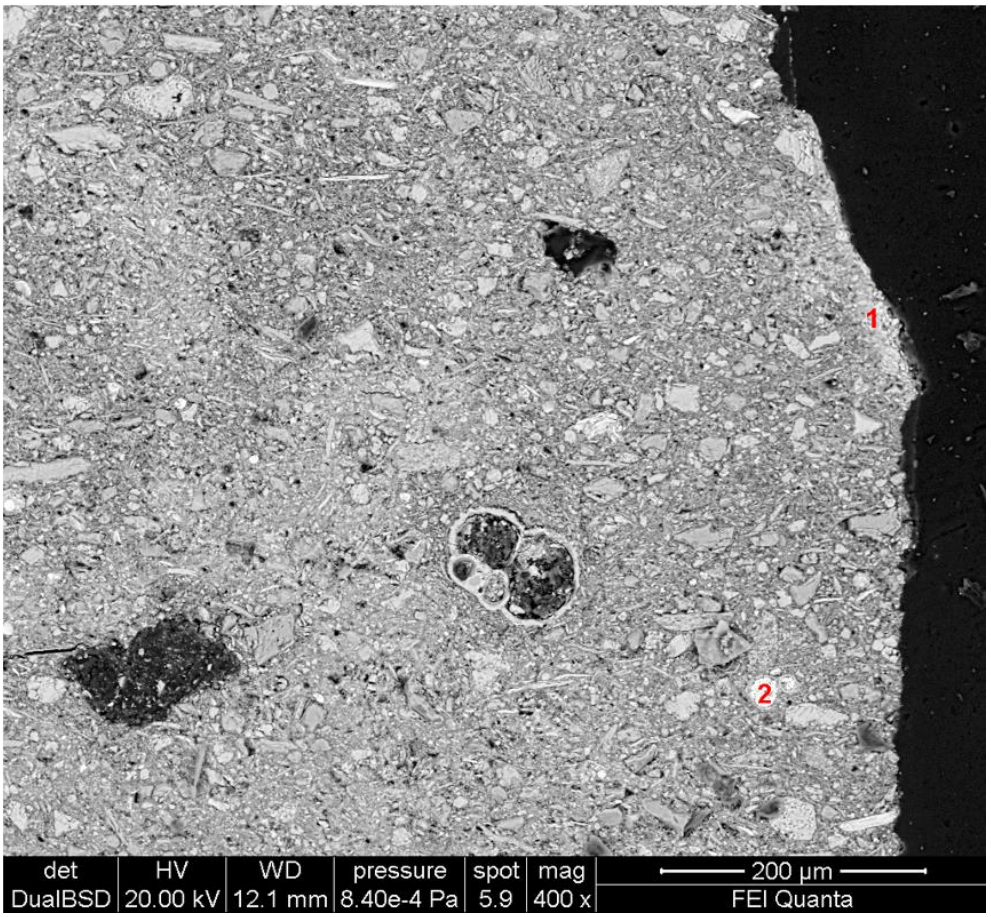

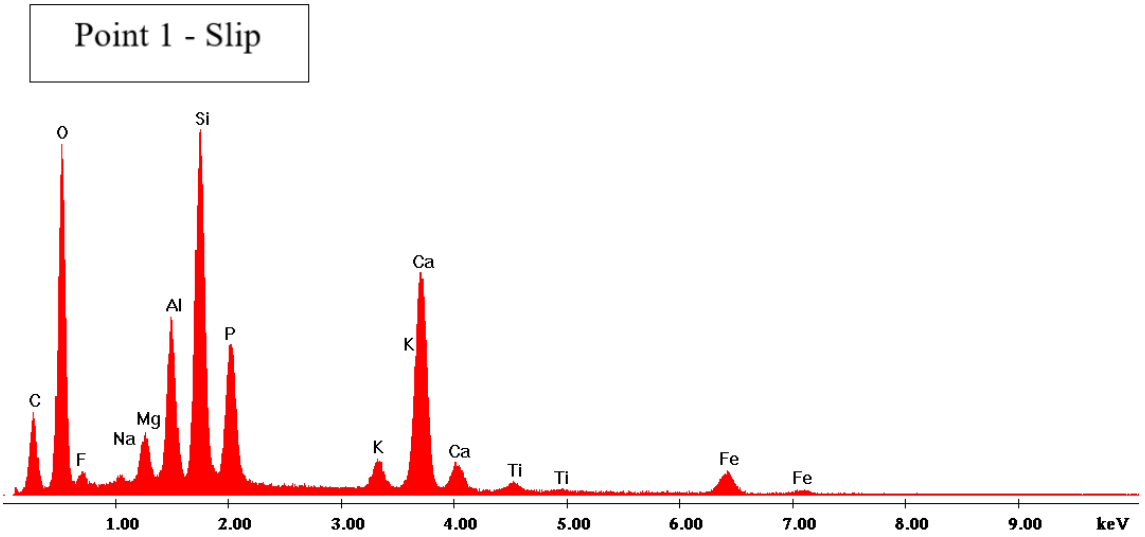

Point 2 - Iron oxide

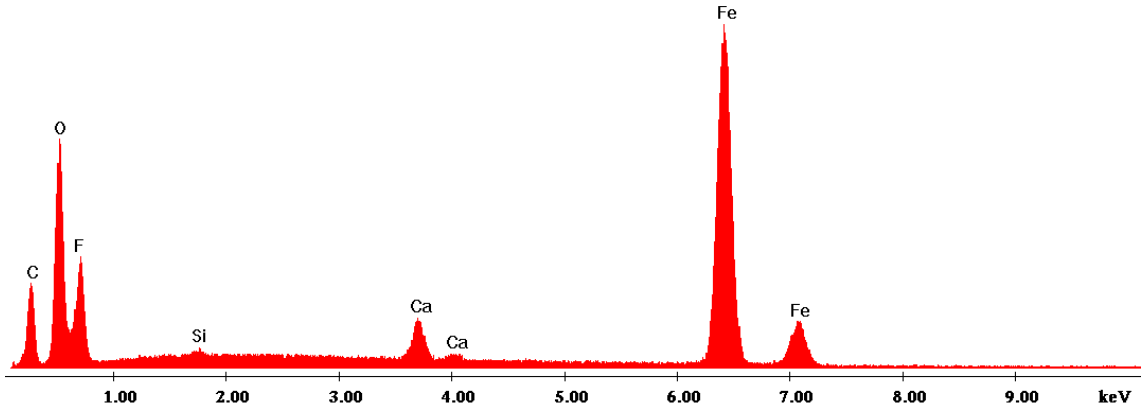

3.3 Fourier-transform infrared spectroscopy (FTIR)

For this study, infrared spectra of terra sigillata samples were collected and analyzed by ATR and transmission mode. Both modes complement each other and yield representative results. ATR identifies the bulk mineral composition of the samples, as it investigates a volume instead of a surface. On the contrary, micro-FTIR point analysis can verify the presence of minerals or mineral phases in traces.

All samples (Table 5) show the presence of silicates and quartz. Extremely common are also clay minerals and carbonates. Silicates present a characteristic absorption band near 1000 cm^{-1} related to the stretching of Si-O bonds and several weak absorption bands in the range of 400-650 cm^{-1} due to the bending of Si-O bonds.

The fundamental vibrations of carbonates are in the spectral regions 1400–1600 cm^{-1} due to asymmetric stretching vibrations and 873–880 cm^{-1}, resulting from out-of-plane bending vibrations. Calcite, for example, can readily be identified because it shows an in-plane band at 711 cm^{-1}, an out-of-plane band at 876 cm^{-1}, and an antisymmetric stretch at 1402 cm^{-1}. Compared to calcite, dolomite displays characteristic FTIR absorptions at 3020, 2626, and 730 cm^{-1}. The intensity of the carbonates and the calcite peak is higher in samples SP.01.2023, SP.14.2023, and SP.15.2023. SP.02.2023, SP.05.2023, SP.07.2023, SP.09.2023, SP.10.2023, SP.11.2023, SP.12.2023, and SP.13.2023 attest the presence of carbonates in lower bands, such as calcite and dolomite.

Considering the ATR results, the most dominant bands are that of clay minerals in the 1000–900 cm^{-1} region and silicates at around 1000 cm^{-1}, whose intensity remains high throughout the samples. They are usually broad, while bands of silicates overlap with those of other clay minerals, and they cannot be discriminated easily.

SP.02.2023, SP.07.2023, SP.10.2023, SP.11.2023, and SP.12.2023 bear low-intensity bands of kaolinite. Regarding kaolinite, the Si-O stretching vibrations generally give strong and sharp bands in the 1120–1000 cm^{-1} region. The antisymmetric in-plane Si-O-Si stretching vibrations give strong bands at 1037–1033 cm^{-1} and 1012–1002 cm^{-1}, while a high-frequency band at 1121–1116 cm^{-1} is assigned to the symmetric stretching Si-O vibrations. The Al_2OH bending bands near 915 and 935 cm^{-1} are caused by vibrations of inner and inner-surface OH groups, respectively. The OH stretching region of kaolinite shows four bands at 3694, 3669, 3652, and 3620 cm^{-1}. The 3620 cm^{-1} band comes from the stretching vibrations of single ‘inner’ hydroxyl

groups (n(OH)) within the plane of tetrahedral and octahedral sheets.

Hematite also shows the characteristic absorption bands of iron oxide at the wavenumbers of 431 and 519 cm^{-1}. SP.05.2023, SP.06.2023, SP.07.2023, SP.08.2023, SP.09.2023, SP.10.2023, SP.11.2023, SP.12.2023, SP.13.2023, and SP.15.2023 show moderate intensity bands of hematite. Almost all FT-IR spectra document the presence of water, as the H_2O-stretching band is very broad around 3430 cm^{-1}, and the H_2O bending mode is observed at 1630–1640 cm^{-1}. In addition, diopside can be identified with characteristic bands at 962, 863, and 673 cm^{-1} that correspond to Si-O stretching and O-Si-O bending vibrations. In samples SP.03.2023, SP.04.2023, SP.08.2023, SP.09.2023, SP.10.2023, and SP.11.2023, low-intensity bands of diopside can be observed.

Figure 62. FTIR spectra of sample SP.01.2023.

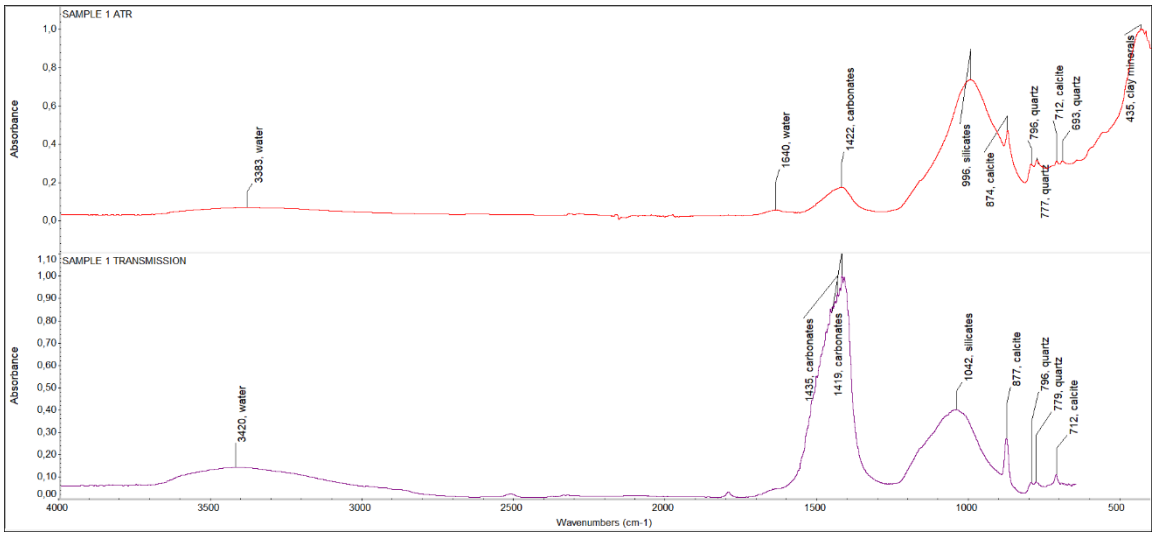

Figure 63. FTIR spectra of sample SP.02.2023.

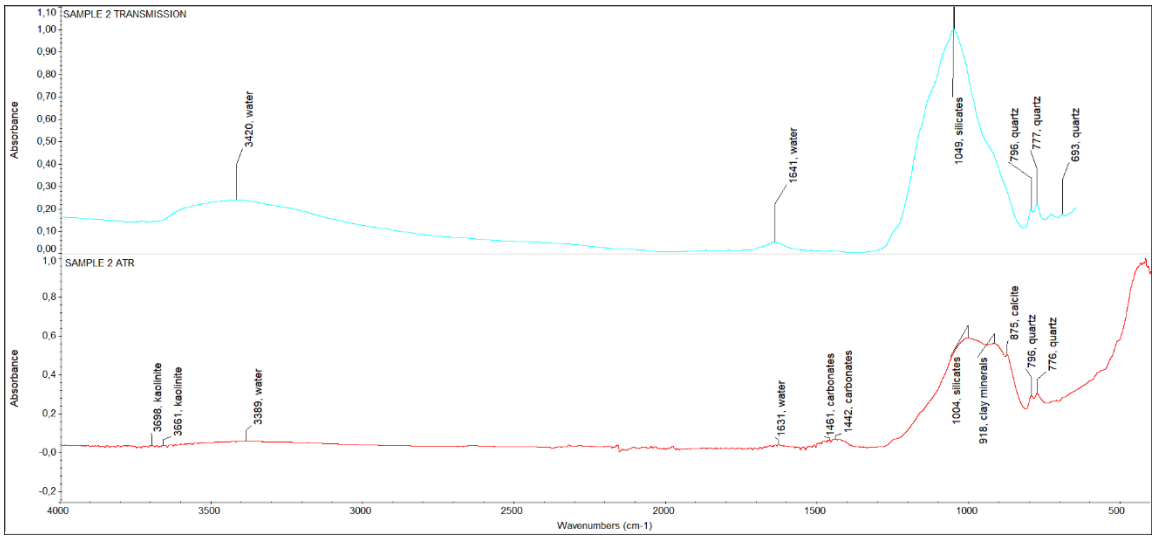

Figure 64. FTIR spectra of sample SP.03.2023.

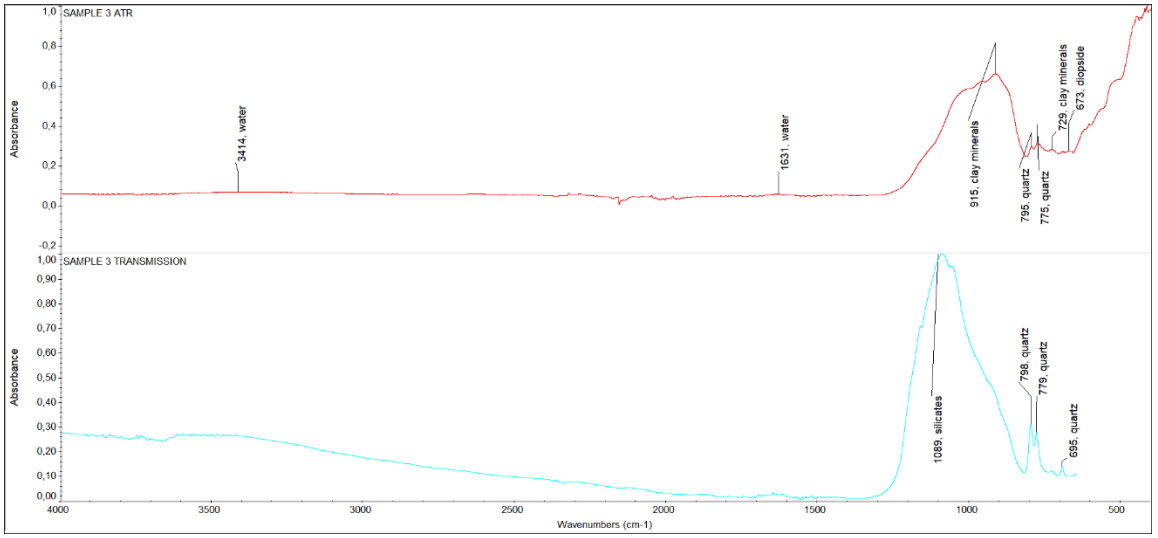

Figure 65. FTIR spectra of sample SP.04.2023.

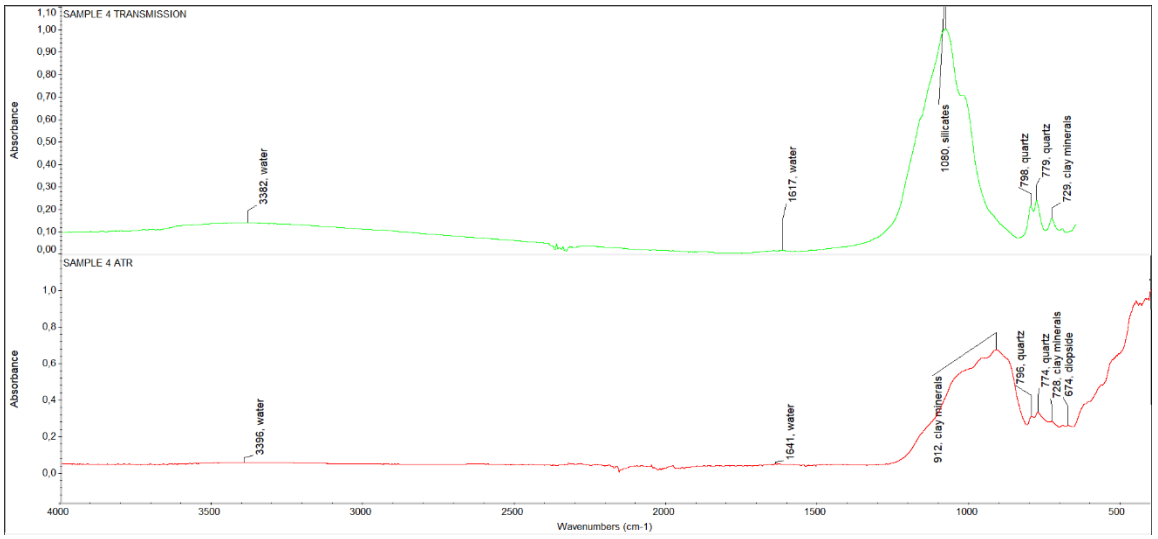

Figure 66. FTIR spectra of sample SP.05.2023.

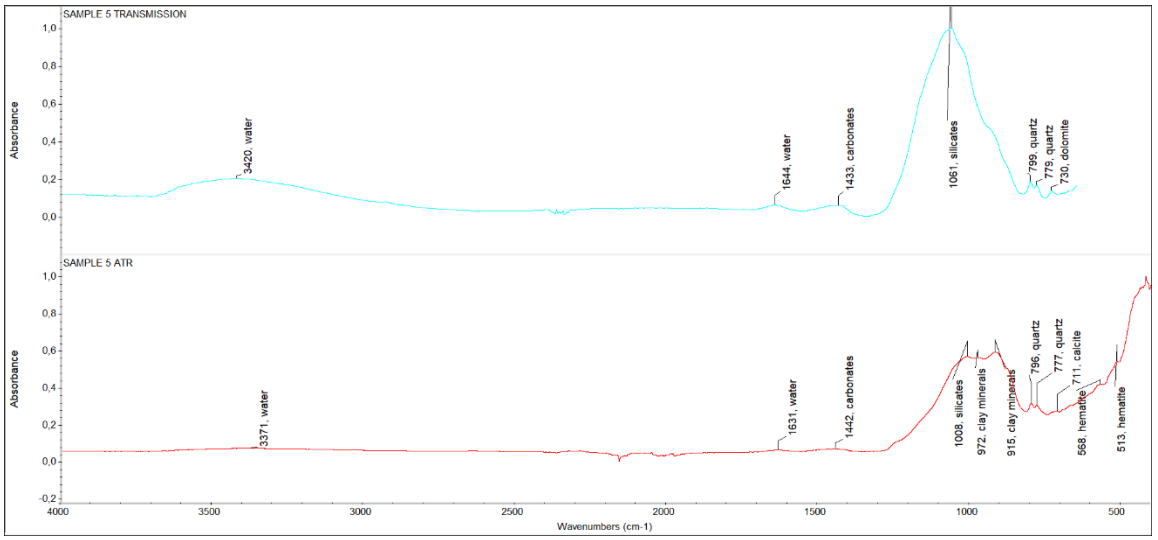

Figure 67. FTIR spectra of sample SP.06.2023.

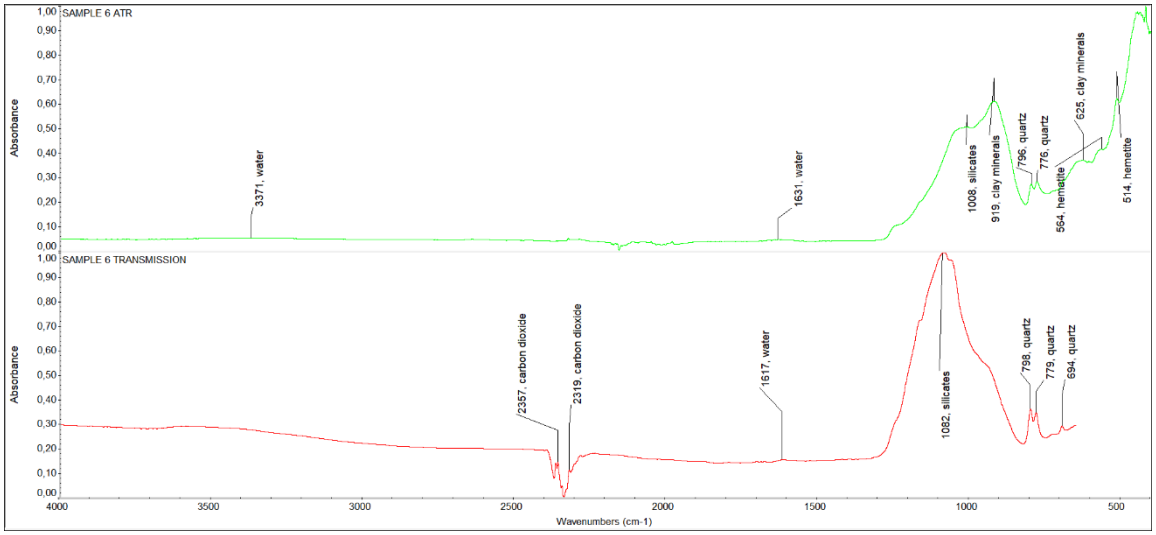

Figure 68. FTIR spectra of sample SP.07.2023.

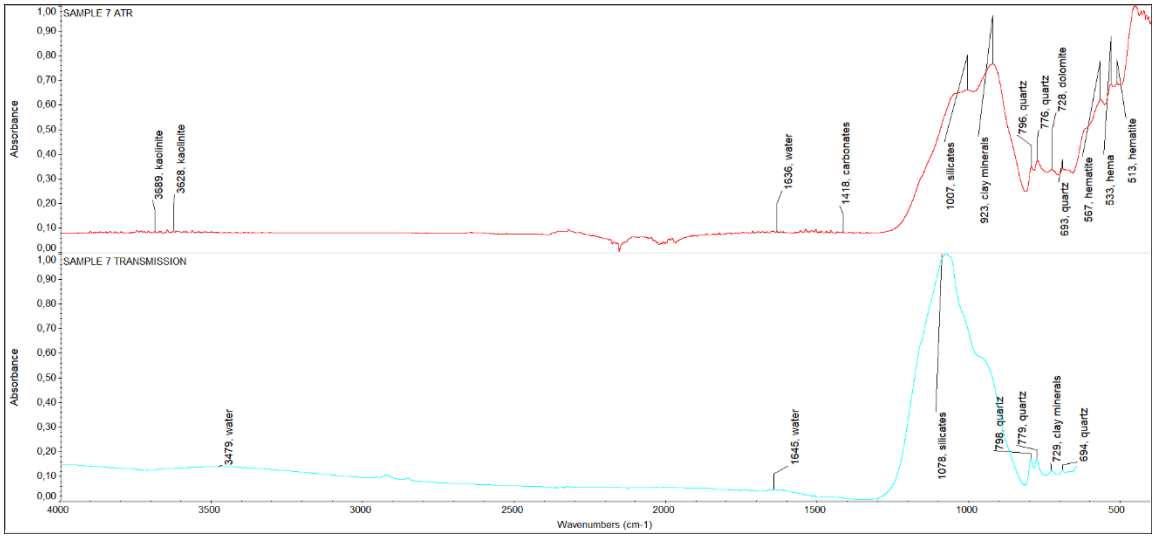

Figure 69. FTIR spectra of sample SP.08.2023.

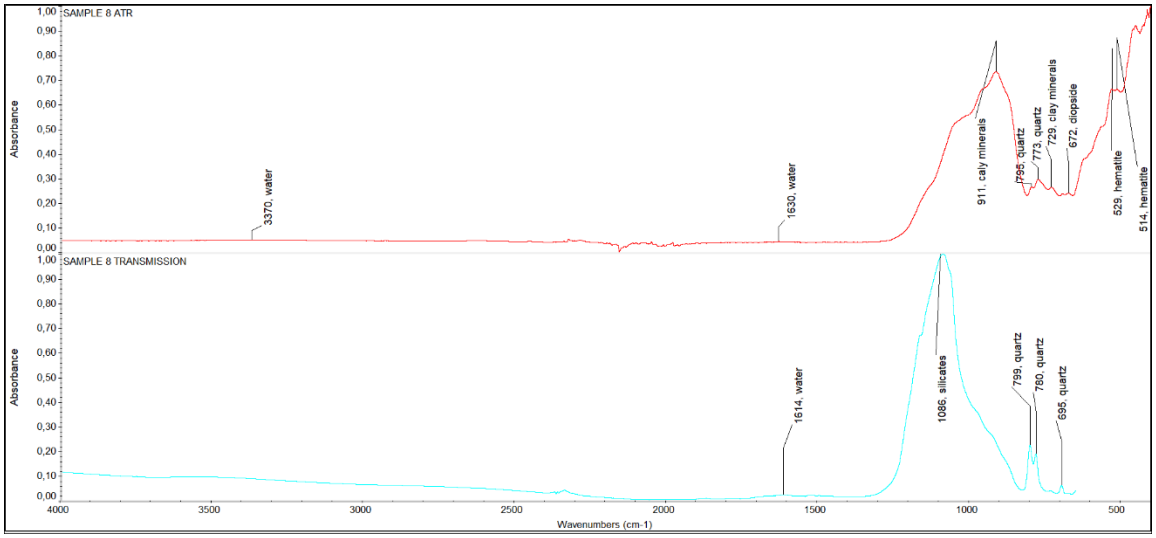

Figure 70. FTIR spectra of sample SP.09.2023.

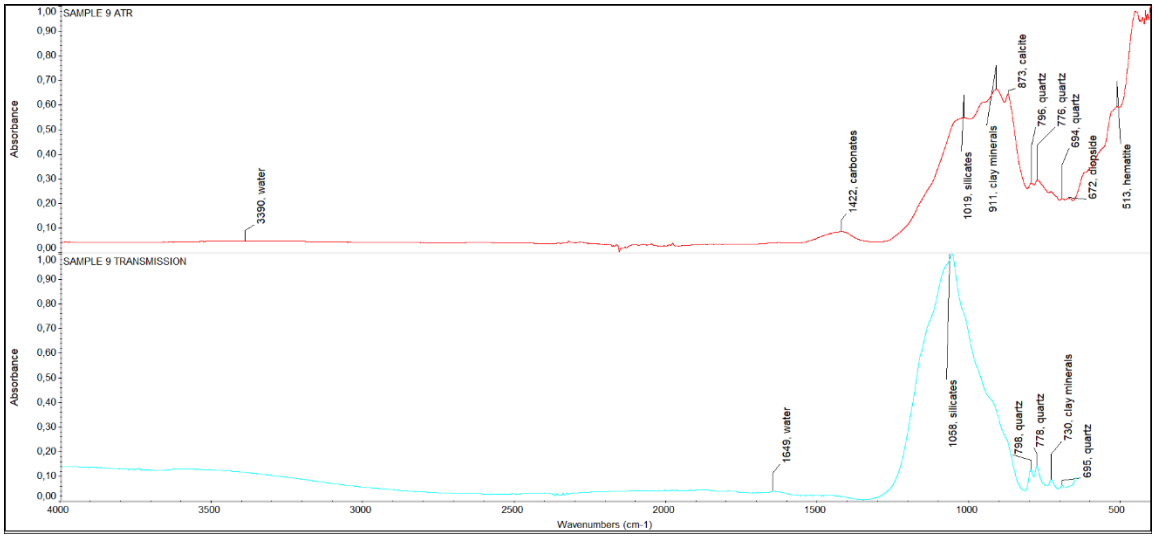

Figure 71. FTIR spectra of sample SP.10.2023.

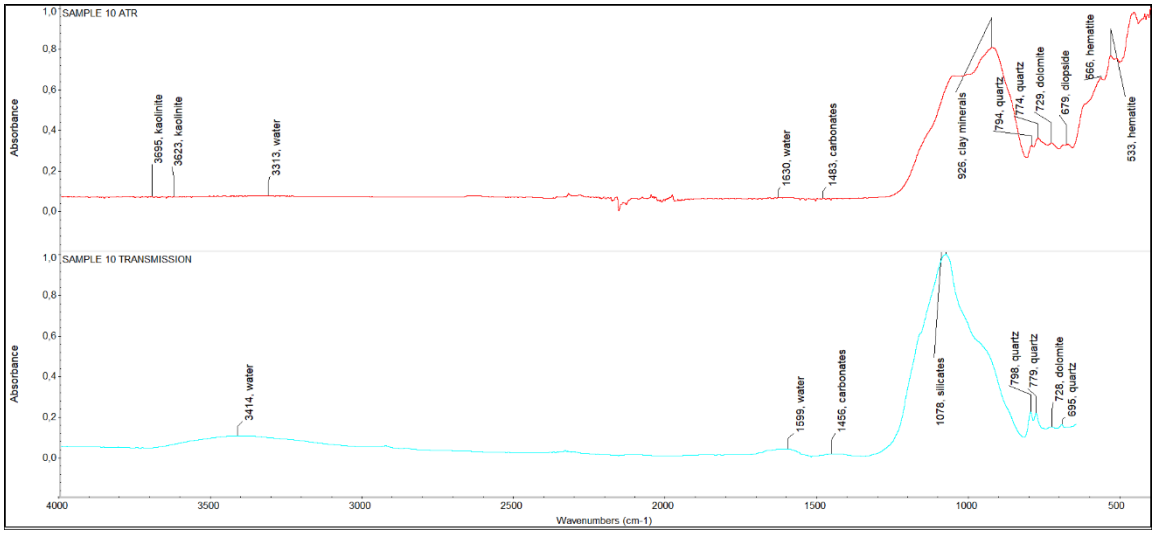

Figure 72. FTIR spectra of sample SP.11.2023.

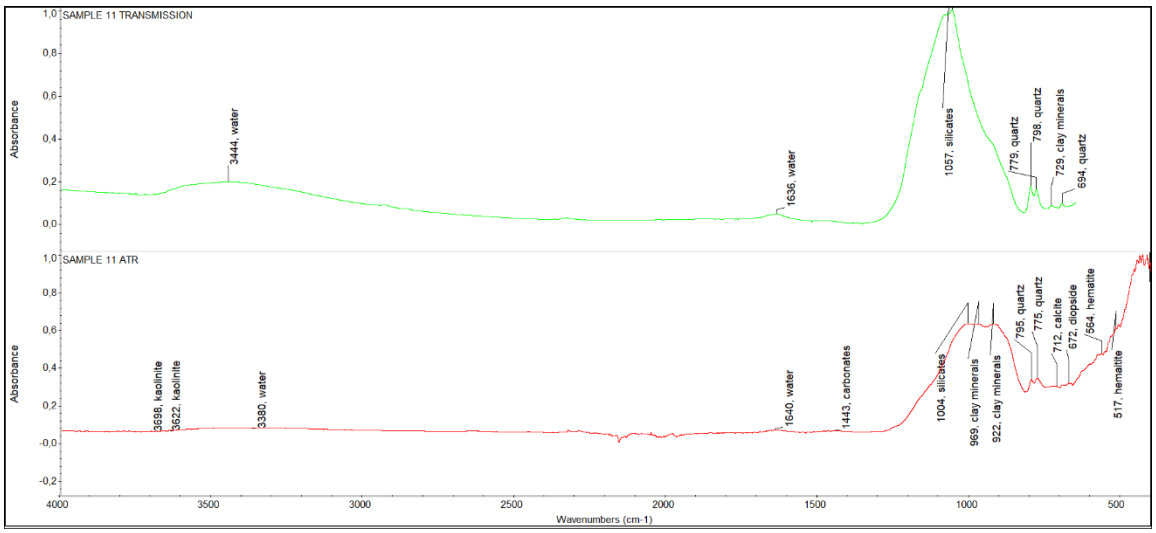

Figure 73. FTIR spectra of sample SP.12.2023.

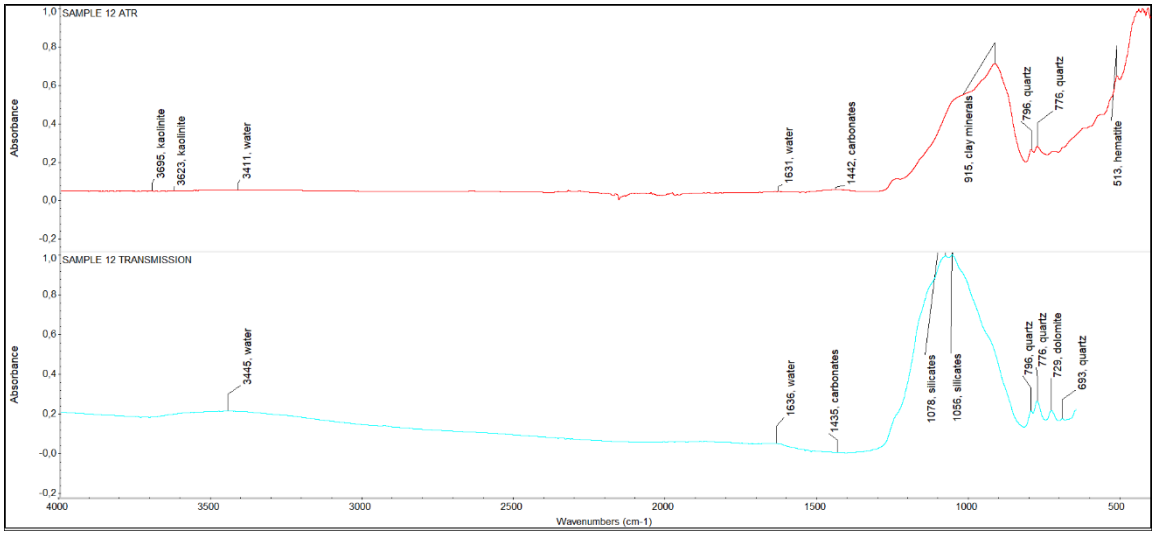

Figure 74. FTIR spectra of sample SP.13.2023.

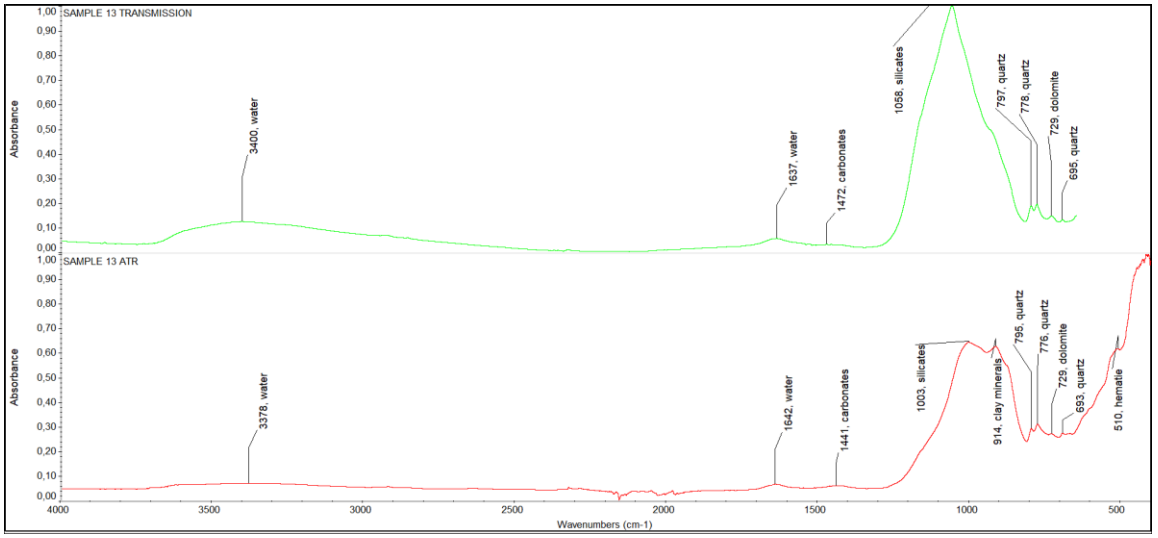

Figure 75. FTIR spectra of sample SP.14.2023.

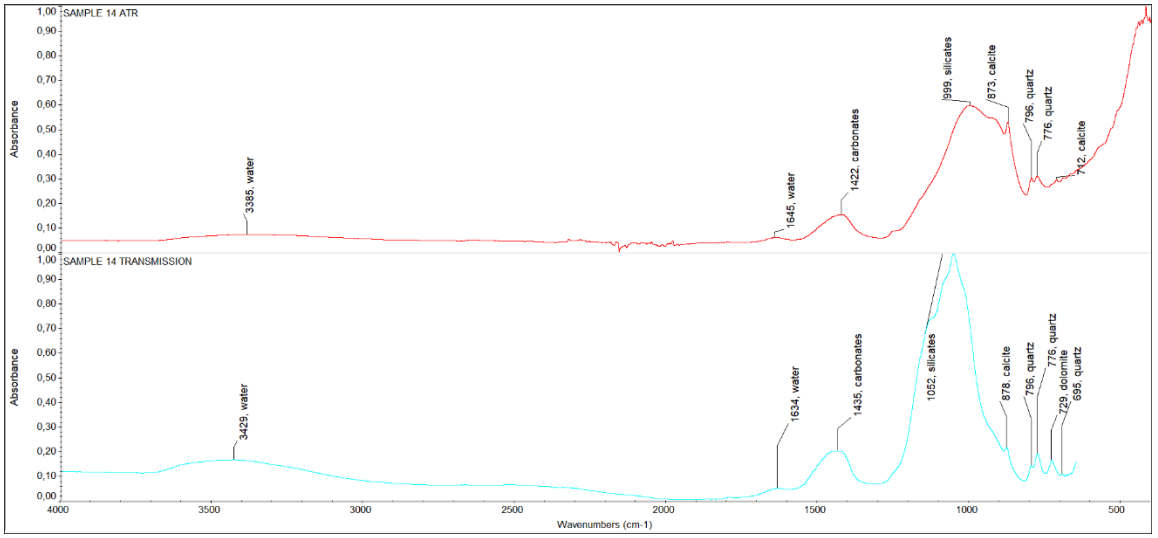

Figure 76. FTIR spectra of sample SP.15.2023.

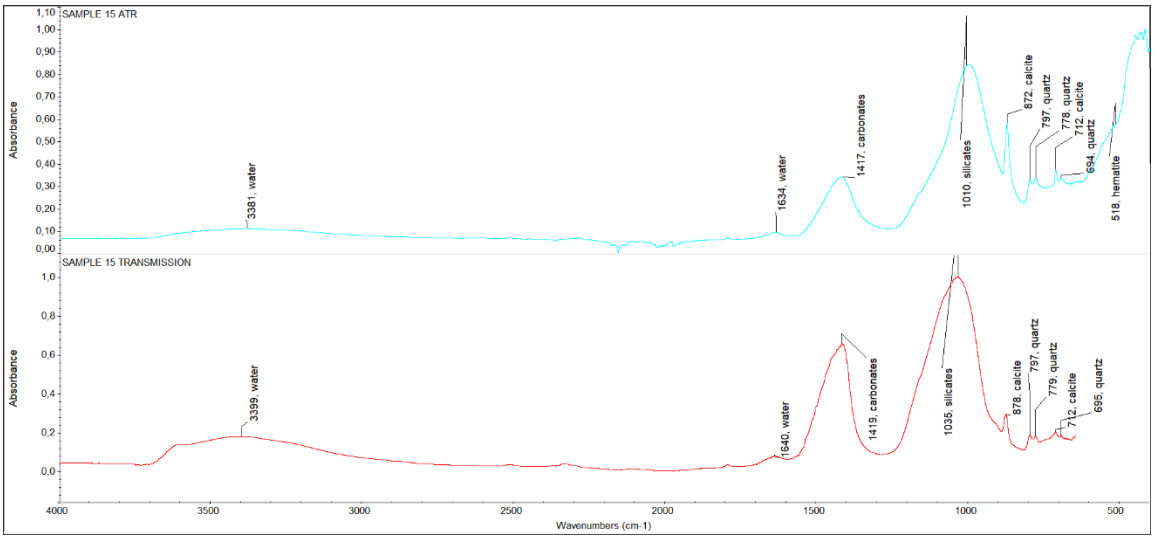

Table 4. Summary of the identified minerals by ATR in each sample with their characteristic absorption bands.

Sample	Minerals	Bands (cm^{-1})
SP.01.2023	clay minerals	435
	silicates	996
	calcite	874, 712
	quartz	796, 777, 693
	carbonates	1422
	H_2O	3383, 1640
SP.02.2023	silicates	1004
	clay minerals	918
	quartz	796, 776
	calcite	875
	carbonates	1461, 1442
	kaolinite	3698, 3661
	H_2O	3389, 1631
SP.03.2023	clay minerals	915, 729
	quartz	795, 775
	diopside	673
	H_2O	3414, 1631
TRANSMISSION	silicates	1089
SP.04.2023	clay minerals	912, 728
	quartz	796, 774
	diopside	674

	H_2O	3396, 1641
TRANSMISSION	silicates	1080
SP.05.2023	clay minerals	972, 915
	silicates	1008
	quartz	796, 777
	hematite	568, 513
	calcite	711
	carbonates	1442
	H_2O	3371, 1631
TRANSMISSION	dolomite	730
SP.06.2023	clay minerals	919, 625
	hematite	564, 514
	silicates	1008
	quartz	796, 776
	H_2O	3371, 1631
TRANSMISSION	CO_2	2357, 2319
SP.07.2023	clay minerals	923
	silicates	1007
	hematite	567, 533, 513
	quartz	796, 776, 693
	dolomite	728
	carbonates	1418
	kaolinite	3689, 3628
	H_2O	1636
SP.08.2023	clay minerals	911, 729
	hematite	529, 514
	quartz	795, 773
	diopside	672
	H_2O	3370, 1630
TRANSMISSION	silicates	1086
SP.09.2023	clay minerals	911
	calcite	873
	hematite	513
	silicates	1019
	quartz	796, 776, 694
	diopside	672
	carbonates	1422
	H_2O	3390
	clay minerals	926
	hematite	566, 533

SP.10.2023	quartz	794, 774
	dolomite	729
	diopside	679
	kaolinite	3695, 3623
	carbonates	1483
	H_2O	3313, 1630
TRANSMISSION	silicates	1078
SP.11.2023	silicates	1004
	clay minerals	969, 922
	hematite	564, 517
	quartz	795, 775
	calcite	712
	diopside	672
	carbonates	1443
	H_2O	3380, 1640
	kaolinite	3698, 3622
SP.12.2023	clay minerals	915
	hematite	513
	quartz	796, 776
	carbonates	1442
	H_2O	3411, 1631
	kaolinite	3695, 3623
TRANSMISSION	silicates	1078, 1056
	dolomite	729
SP.13.2023	silicates	1003
	clay minerals	914
	hematite	510
	quartz	795, 776, 693
	dolomite	729
	carbonates	1441
	H_2O	3378, 1642
SP.14.2023	silicates	999
	calcite	873, 712
	quartz	796, 776
	carbonates	1422
	H_2O	3385, 1645
TRANSMISSION	dolomite	729
	silicates	1010
	calcite	872, 712
	carbonates	1417

SP.15.2023	quartz	797, 778, 694
	hematite	518
	H_2O	3381, 1634

Table 5. Summary of samples analyzed with FTIR and their identified minerals.

SAMPLE	MINERALS
SP.01.2023	clay minerals, silicates, calcite, quartz, carbonates, H_2O
SP.02.2023	silicates, clay minerals, quartz, calcite, carbonates, kaolinite, H_2O
SP.03.2023	clay minerals, quartz, diopside, H_2O, silicates
SP.04.2023	clay minerals, quartz, diopside, H_2O, silicates
SP.05.2023	clay minerals, silicates, quartz, hematite, calcite, carbonates, H_2O, dolomite
SP.06.2023	clay minerals, hematite, silicates, quartz, H_2O, CO_2
SP.07.2023	clay minerals, silicates, hematite, quartz, dolomite, carbonates, kaolinite, H_2O
SP.08.2023	clay minerals, hematite, quartz, diopside, H_2O, silicates
SP.09.2023	clay minerals, calcite, hematite, silicates, quartz, diopside, carbonates, H_2O
SP.10.2023	clay minerals, hematite, quartz, dolomite, diopside, kaolinite, carbonates, H_2O, silicates
SP.11.2023	silicates, clay minerals, hematite, quartz, calcite, diopside, carbonates, H_2O, kaolinite
SP.12.2023	clay minerals, hematite, quartz, carbonates, dolomite, H_2O, kaolinite, silicates
SP.13.2023	silicates, clay minerals, hematite, quartz, dolomite, carbonates, H_2O
SP.14.2023	silicates, calcite, quartz, carbonates, H_2O, dolomite
SP.15.2023	silicates, calcite, carbonates, quartz, hematite, H_2O

The fifteen terra sigillata samples could be divided into four groups based on their similar mineralogical composition. Group 1 (Figure 77) includes samples SP.03.2023, SP.04.2023, SP.05.2023, SP.06.2023, SP.08.2023, SP.09.2023, SP.11.2023, SP.12.2023, SP.13.2023. Group 2 (Figure 78) consists of samples SP.02.2023 and SP.14.2023, Group 3 (Figure 79) is composed of samples SP.07.2023 and SP.10.2023, and Group 4 (Figure 80) of samples SP.01.2023 and SP.15.2023.

Figure 77. Group 1 of FTIR-ATR spectra.

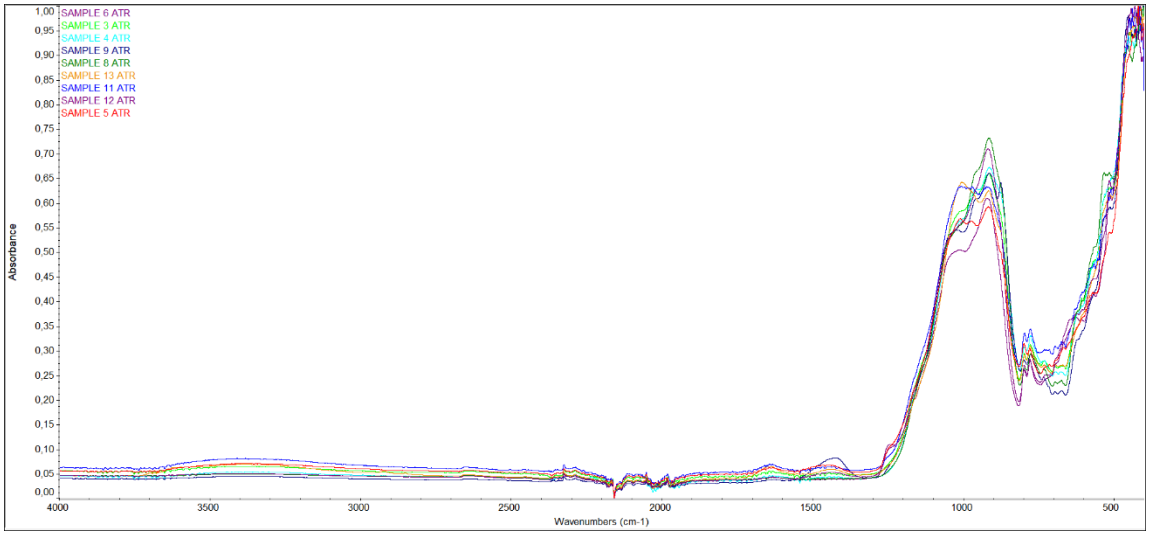

Figure 78. Group 2 of FTIR-ATR spectra.

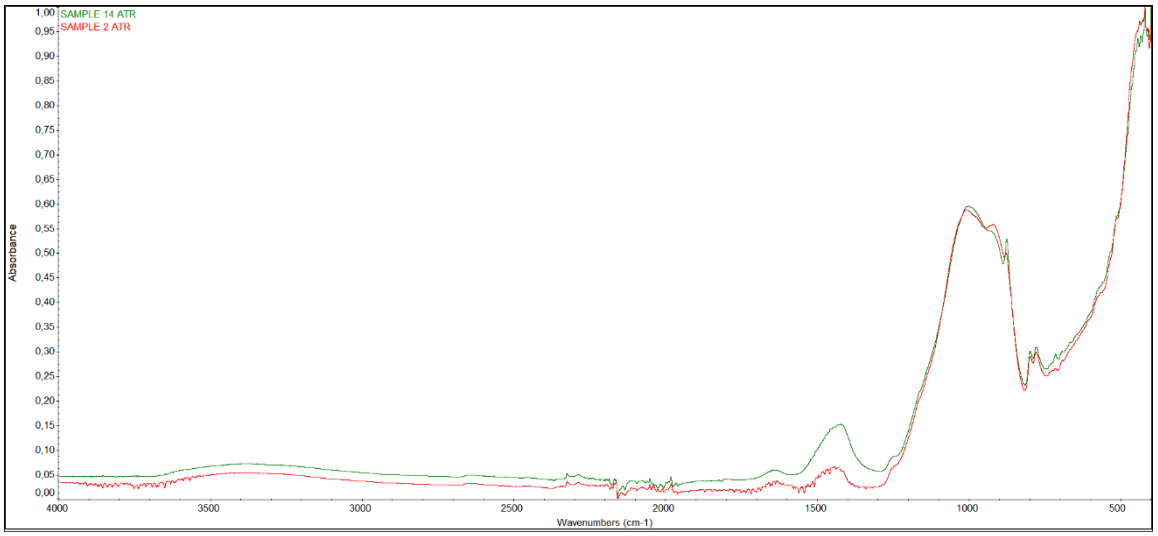

Figure 79. Group 3 of FTIR-ATR spectra.

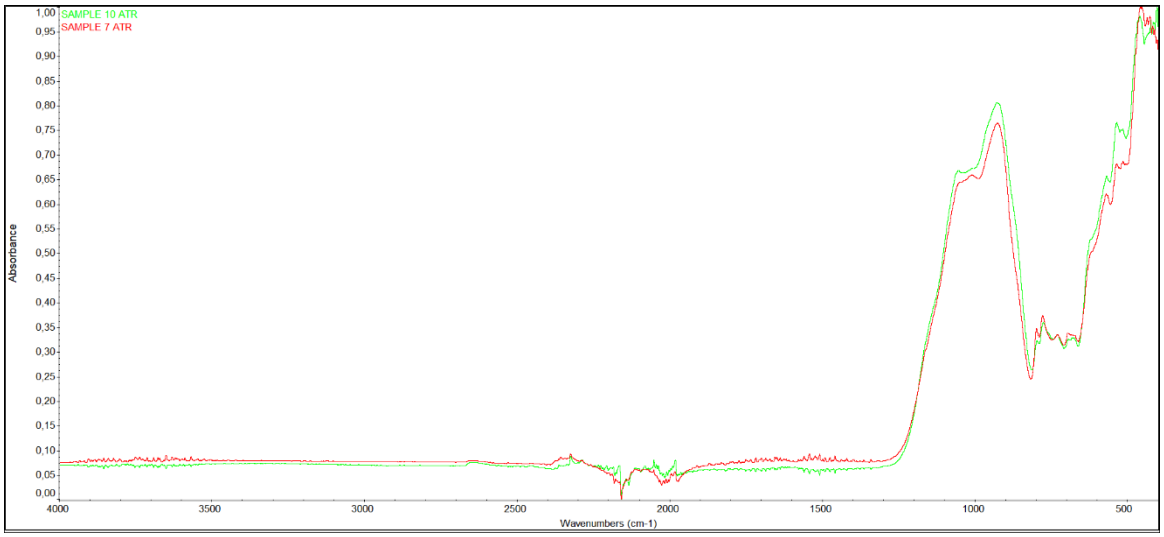

Figure 80. Group 4 of FTIR-ATR spectra.

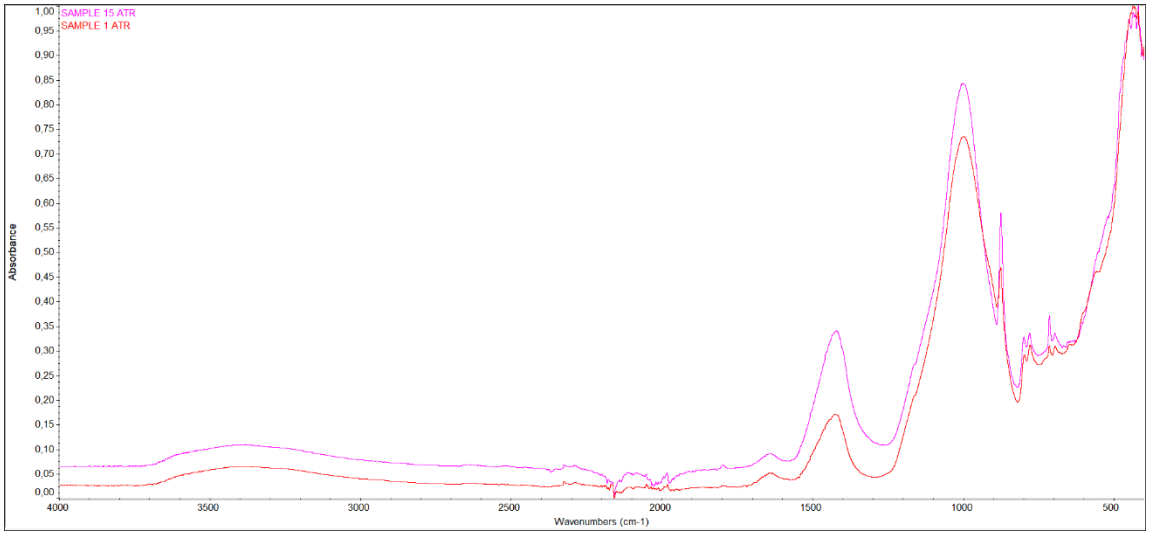

CHAPTER 4: DISCUSSION

The combined application of OM, FTIR, and SEM-EDS yields essential findings about the chemical and mineralogical composition of terra sigillata pottery from Spoletino. Archaeometric analysis has enabled us to draw conclusions regarding the production techniques, the firing conditions, and the possible provenance of the fifteen samples.

All potsherds show fine inclusions of quartz, mica, and nodules of iron oxides set in very fine pastes. SEM-EDS and FTIR results also indicated the presence of K-feldspar, plagioclase, hematite, diopside, carbonates, and other silicates. The most significant differences among all the investigated samples are the inclusion percentage (which never surpasses 30%, and it can be as low as 10%) and the color of the matrix; the matrix in all samples varies from light to dark brown in PPL, and it can be considered heterogeneous, apart from SP.07.2023 which is homogeneous. Heterogeneity in the matrix can be present for various reasons, such as natural compositional differences in the clay, the intentional mixing of clay by the potters, fluctuations in the firing atmosphere, and post-depositional processes (Quinn, 2013).

4.1 Production process

Ceramic body

As stated in Chapter 1.5, fine quartz sand was mainly used to produce terra sigillata (Ettlinger, 1990). OM confirmed this fact since quartz was the dominant inclusion in all cases, and their particle size was relatively small (<0.3 mm). Quartz is the most common mineral on the earth's continental surface. It has a very simple chemical formula (SiO_2), but the provenance of quartz inclusions can rarely be determined (Velde & Druc, 1999). Sandstones contain mostly quartz and K-feldspar or plagioclase with inclusions ranging from 0.06 to 2 mm (Braekmans & Degryse, 2017); therefore, clay deposits formed partly from sandstone weathering could be suitable for sigillata production.

Calcareous clays were intentionally selected for terra sigillata production (Ettlinger, 1990; Van Oyen, 2016). SEM-EDS and FTIR analysis indicate the calcareous nature of the clay matrix due to carbonates, such as calcite and dolomite. SP.15.2023 is particularly calcareous, as SEM-EDS revealed the presence of calcareous microfossils

(foraminifera). Both primary calcite crystals (minerals from the original clay that were not extinguished during firing) and micritic calcite crystals (dispersed regularly among the clay minerals) have been documented (Quinn, 2013; Reedy, 2008).

The distinction between primary and secondary calcite by IR spectroscopy is achieved since the main CO_3 band of the secondary calcite is found at a higher frequency (1430-1450 cm-^{1}) than that of the primary calcite (1420-1430 cm-^{1}) (Shoval, 2017). Specifically, samples SP.01.2023, SP.07.2023, SP.09.2023, SP.14.2023, and SP.15.2023 bear primary calcite since the band of carbonates is found in the 1420-1430 cm-^{1} range, either by ATR or Transmission mode (see Table 4).

On the other hand, samples SP.02.2023, SP.05.2023, SP.10.2023, SP.11.2023, SP.12.2023, and SP.13.2023 show bands of secondary calcite, generally within the 1430-1450 cm-^{1} spectral range. Moreover, the TiO_2 (Figure 56) found in the sample SP.05.2023 (the *unicum*) is an accessory mineral commonly present in clay deposits (Velde & Druc, 1999).

Before production, the raw clay was purified to remove the coarser fraction, as the absence of coarse inclusions indicates. Terra sigillata clays were refined through levigation. The clay was passed through a chain of overflowing basins, and each basin withheld a part of the coarser fabric until the material acquired the proper plasticity. The heaviest or biggest inclusions fell out first, the lightest or smallest last, and a fine clay slurry was collected at the bottom of the last basin (Van Oyen, 2016; Velde & Druc, 1999).

This refinement process was reserved for this type of fine tableware with particular uses. Refined clays resulted in low porosity and, thus, low permeability, the degree to which water passes through the vessel walls. Moreover, the lack of aplastic temper made sigillata susceptible to thermal shock and discouraged its use for cooking (Quinn, 2022). Low porosity and absence of large aplastic inclusions render sigillata vessels impermeable and suitable for drinking, eating, serving, and mixing food. However, in the Roman world, eating and drinking were connected with many social activities, so sigillata pottery is also found in funerary and ritual contexts. The fact that sigillata pots were used for ritualistic purposes, such as libation ceremonies, was probably related to the strength, the smoothness, and the impermeability of their surface (Kenrick, 1993; Ortalli, 2017; Van Oyen, 2016).

All samples are characterized by unimodal grain size distribution and very low

porosity, with less than 5% of voids throughout the samples. The levigation process may also cause strongly unimodal grain size distribution, as it increases the relative proportion of clay and alters the grain size distribution of the inclusions (Quinn, 2022). Very rare clay pellets were observed only in SP.01.2023 (Figure 54). Rounded clay pellets with sharp boundaries will likely occur naturally during clay deposition (Quinn, 2013). All the above, including the general absence of clay pellets, indicate an even mixing of the ceramic paste and a noteworthy lack of added temper (Velde & Druc, 1999).

After clay refinement, it is known from archaeological literature that vessels were formed on the fast-turning wheel. Molds were used for decorated vessels, while plain vessels were mainly hand-thrown. Wooden templates and formers could be utilized to form the accentuated profiles of the vessels with remarkable consistency (Ettlinger, 1990; Van Oyen, 2016). Unfortunately, it is unknown if the fragments were cut in vertical, horizontal, or tangential orientations during sampling, so it is difficult to draw conclusions about the vessel-forming techniques (Quinn, 2022).

Slip

After forming, the vessels were stamped while the clay was still wet. Stamps were usually placed on the inner base of the plain ware, but on mold-decorated vessels, they could be part of the decoration, for example, placed on the sides (Fülle, 1997; Kiiskinen, 2013). Then, the pots were submerged upside-down in the slip, a fine clay suspension, and left to dry. A brush may also have been used to lay down the slip on the ceramic surface (Ettlinger, 1990; Mirti et al., 1999; Van Oyen, 2016). In Scoppieto, the upper part of some pots near the rim has been submerged twice inside the slip, resulting in a darker double-dipping streak (Bergamini, 2016).

Most samples, such as SP.01.2023, SP.02.2023, SP.03.2023, SP.04.2023, SP.07.2023, SP.08.2023, and SP.10.2023, showed an even application of the slip under OM examination, which is consistent with dipping the vessel in a suspension. SP.01.2023 also shows a light-yellow preparation layer of polishing under the slip (Figure 42). However, such a preparation layer was not evident when examining the rest of the samples.

It is generally accepted that illitic clays were purified extensively and used for the slip. Plant ash could also be added, as the high potassium content of the slip may indicate (Bimson, 1956; Mirti et al., 1999; Rice, 2015). Bimson (1956) discussed a series of

experimental firings in the British Museum laboratories. She observed a similarity, apparent before firing, between the shiny appearance of sigillata slip and the luster achieved by polishing other clays (such as kaolinite, montmorillonite, and smectite). She suggested that clay minerals aligning parallel to the ceramic surface may result in this luster. In polishing, parallel orientation is achieved by applying external pressure, while in the case of terra sigillata, illite clay minerals take up a similar alignment due to their surface forces.

Traces of kaolinite clay mineral in the ceramic body were found in samples SP.02.2023, SP.07.2023, SP.10.2023, SP.11.2023, SP.12.2023. The matrix of many ceramics consists primarily of illitic clay, sometimes with kaolinite and, more rarely, smectite. This could be explained by the fact that kaolinite and illite could coexist in the same clay deposit (Huggett, 2005; Ionescu & Hoeck, 2017). However, traces of illite could not be distinguished in the FTIR-ATR spectra, as illite is not so readily detectable by FTIR when mixed with kaolinite.

Based on SEM-EDS results, the slip and the matrix showcase slightly different chemical compositions, which is an outcome of the extensive purification of the slip. EDS spectra of SP.04.2023 (Figure 53), SP.01.2023 (Figure 55), and SP.07.2023 (Figures 58 and 59) show that the slip is more enriched in Al_2O_3, K_2O, and Fe_2O_3 than the matrix, while the matrix is more calcareous than the slip. However, the slip and the matrix generally exhibit a relatively low amount of Fe, and their chemical composition does not show significant differences.

According to the existing literature, the raw material that forms the slip could come from separately mined clays or the same clay deposit (Ettlinger, 1990; Van Oyen, 2016). Regarding samples SP.01.2023, SP.04.2023, and SP.07.2023, the slip may have formed from an iron-rich clay suspension that was purified from the same clay with the matrix. The inner layer of the slip in SP.05.2023 also seems more embedded in the matrix and shows similar chemical composition (Figures 56 and 57). The same argument cannot be supported for SP.15.2023 (Figures 60 and 61), given that the slip is significantly more calcareous than the matrix. Therefore, pinpointing the slip's origin is more complicated in this case.

SEM images reveal good adhesion of the slip to the body and a high degree of sintering. In all fragments, the line of separation between slip and body is quite definite, apart from samples SP.05.2023 and SP.15.2023. These samples are again

characterized by a reasonably high degree of sintering, but the slip is thinner and irregular. Sintering is another reason why sigillata vessels are impermeable and suitable for tableware, as the slip acquires glaze-like qualities (Van Oyen, 2016).

Firing temperature and atmosphere

Concerning the atmosphere developed during the firing process, the diffuse presence of nodules of iron oxides in thin sections has been confirmed by identifying hematite through SEM-EDS and FTIR analysis. Nodules of iron oxides are common inclusions in all sigillata samples and are responsible for the heterogeneous color of the matrix. For example, samples SP.06.2023 (Figure 39), SP.02.2023 (Figure 43), SP.09.2023 (Figure 46), SP.12.2023 (Figure 48), and SP.15.2023 (Figure 52) show darker grey-black areas due to the diffusion of iron oxides.

As mentioned in Chapter 1.5, the reddish appearance of terra sigillata directly results from the presence of hematite after firing in an oxidizing atmosphere (Ettlinger, 1990; Van Oyen, 2016). Hematite can be included in the raw clay material or present due to reactions from the dehydroxylation of goethite. In the latter, it forms at around 500 °C but remains poorly ordered up to 900 °C and appears well ordered from 900 to 1200 °C. When hematite is initially present in the clay, it remains constant or shows a minor increase at 700 °C (Gliozzo, 2020b). The higher iron (Fe_2O_3) content of the slip compared to the matrix, as shown in EDS spectra, also explains why the slip has such a shiny red color.

The vessel's firing temperature influences the clay matrix's color and optical activity. The samples are characterized by moderate or weak optical activity. For this reason, temperatures are thought to be lower than 850 °C (Ready, 2008). Clay matrices lose their birefringence between 800–850 °C during firing. Given that the birefringence is weak or moderate, samples can be interpreted as having an approximate firing temperature of 800–850 °C. One possible explanation for the isotropic slip of SP.15.2023 is likely the presence of K_2O, Fe_2O_3, and CaO that act as fluxes and lower the sintering temperature (Quinn, 2013).

In particular, because Ca and Mg behave as fluxes, clay rich in carbonates has significantly lower sintering (around 800 °C) and vitrification temperature than non-calcareous material (Quinn, 2022). Calcium carbonate dissolves into calcium oxide (lime) at 600-850 °C, releasing carbon dioxide. Thus, primary calcium carbonate (such as calcite that has not undergone recrystallization) is a marker of relatively low firing

temperatures (Braekmans & Degryse, 2017; Schneider, 2017). Primary calcite more commonly disappears at temperatures between 750 and 850-900 °C. However, it can be destabilized entirely within a temperature range between 600 and 1000 °C, depending on grain size (the smaller the grain size, the lower the temperature of destabilization), the heating rate and cooling time, and other possible factors (Gliozzo, 2020b; Velde & Druc, 1999).

The associated carbonate mineral dolomite dissolves at a slightly lower temperature than calcite. At 800-850 °C, the free lime that forms as calcium carbonate dissolves and reacts with clay minerals (such as illite) to create neo-formed minerals (Quinn, 2022; Shoval, 2017). FTIR results highlighted the absence of specific clay minerals besides kaolinite, which was found in traces. This lack of clay minerals indicates 750 °C as a lower firing limit, the temperature at which clay minerals (kaolinite) are still present. Clay minerals, such as illite and smectite, are generally dehydrated at temperatures between 459 and 900 °C. At higher temperatures, recrystallization, sintering, or collapse of metakaolinite can happen between 720 and 850 °C (Gliozzo, 2020b).

The collapse of clay minerals at about 900 °C leads to neo-formed minerals and phases directly influenced by the clay raw material. For example, high-lime clays tend to form plagioclase, diopside, gehlenite, and hematite under oxidizing conditions, while low-lime clays form plagioclase, sanidine, spinel, and hematite (Braekmans & Degryse, 2017).

FTIR spectra also revealed the presence of diopside ($CaMgSi_2O_6$), a type of pyroxene. However, it is impossible to claim whether it is primary or secondary diopside. If it is a newly formed diopside, it typically appears at a temperature range between 800 and 950 °C when CaO reacts with illite clay minerals in the matrix. The small size of diopside crystals (1 μm or less, sometimes 5-10 μm) makes their identification difficult (Braekmans & Degryse, 2017; Gliozzo, 2020b).

If diopside is a primary mineral naturally existing in the raw clay, it could be related to volcanic deposits and is not diagnostic of the firing temperature. In SP.03.2023 and SP.09.2023, among other samples, diopside was identified, and these samples can be linked to the Scoppieto workshop due to their stamps. Pyroxenes are characteristic minerals present in the volcanic outcrops surrounding Scoppieto (Bergamini, 2016).

Quartz is mineralogically stable at the firing range of most ancient ceramics (until

approximately 1150 °C), although a reversible transition from α-quartz (trigonal) to β-quartz (hexagonal) takes place at 573 °C (Braekmans & Degryse, 2017; Gliozzo, 2020b). Feldspars, however, dissolve between 1050–1200 °C, so the presence of both K-feldspars and plagioclases suggests that the ceramics were fired below this temperature (Quinn, 2022). Based on the combined chemical and mineralogical data from OM, SEM-EDS, and FTIR, the selected sigillata shreds were probably fired between 750–850 °C. This fact fits into the classification by Rice (2015) of terra sigillata as a high-fired terracotta or a low-fired earthenware.

To conclude, terra sigillata was fired under oxidizing conditions inside double-chambered kilns. Firing conditions were carefully controlled to ensure the uniform appearance of the pottery (Maritan et al., 2018; Van Oyen, 2016). However, the temperature distribution was possibly not uniform inside the kiln, and vessels fired simultaneously could show temperature fluctuations of as much as 100 °C in different parts of the kiln (Mirti et al., 1999). These temperature fluctuations may be partly responsible for the heterogeneous color of the matrix in most samples.

SEM images also indicate the sintering of the slip and the matrix. Sinterization begins at temperatures of 600 °C and continues until the start of vitrification at around 800–850 °C (Quinn, 2022). X-ray diffraction (XRD) analysis could define the mineralogical composition of the selected sigillata samples more efficiently, thus providing a stricter range regarding the firing temperature.

Post-depositional processes

Secondary calcite originates from primary calcite being redistributed through the matrix. It can be found at the edges of the thin section or around voids, and it could be precipitated by groundwater penetrating the strata of an archaeological site (Quinn, 2022). Precipitated calcite is connected with the presence of water rich in calcium bicarbonate in the burial soil. Chemical and physical alterations in the environment can cause the chemical precipitation of calcite (Fabbri et al., 2014):

$$Ca(HCO_3)_2 \rightarrow CaCO_3 + H_2O + CO_2.$$

In the case of the Spoletino cistern, the high amount of secondary calcite can be explained by the fact that ceramics were found submerged in water. In SP.15.2023 (Figures 60 and 61), the highly calcareous slip can be explained by the influence of secondary calcite that precipitates along the edges of the section.

Moreover, the slip of SP.15.2023 and the external layer of the slip in SP.05.2023 are enriched with phosphates (P_2O_5). This fact could be attributed to post-depositional processes since phosphorus is an element easily affected by contamination from groundwater (Guarino et al., 2011). Phosphorus derives from the soil in which pottery is buried. It can have an exceptionally high concentration in humid climates and acid soils containing bones and organic waste. Regarding terra sigillata, phosphorus is documented to reach up to 10 wt.% P_2O_5 or more in the ceramic body, and that percentage could be even higher in the surface layers (Schneider, 2017).

The ability of ceramics to retain phosphate could be linked to the amorphous silicate phases produced during firing. These amorphous silicate phases act as chemically active substrates upon which phosphate is adsorbed or precipitated. For this reason, along with the purified nature of the slip, we could not pinpoint discrete inclusions of a phosphate phase in OM (Ettlinger, 1990; Freestone et al., 1985). Finally, it should be noted that FTIR analysis of SP.06.2023 showed a double notch for CO_2 at 2357 cm^{-1} and 2319 $cm^{-1,}$ which may originate from the atmosphere (Figure 67) and hence does not require any discussion.

4.2 Provenance of materials

Some tentative assessments can be made regarding the possible provenance of the terra sigillata samples from Spoletino. In this case, it is impossible to identify the provenance using inclusions under OM because levigation was involved in the ceramic production. The size of the inclusions is too small, and the material is exceptionally well-mixed and homogeneous. Bulk analysis by FTIR-ATR, however, pinpointed some significant mineralogical similarities between the samples, which can be divided into four groups.

Group 1 (Figure 77) includes samples SP.03.2023, SP.04.2023, SP.05.2023, SP.06.2023, SP.08.2023, SP.09.2023, SP.11.2023, SP.12.2023, SP.13.2023. SEM-EDS results also showed that this group has a quite uniform chemical composition. Given that SP.03.2023 and SP.09.2023 originate from Scoppieto due to their stamps, it could be suggested that the rest of the samples in this group could have a similar origin. This assumption is probably correct, especially for samples SP.04.2023 and SP.13.2023, which were assumed to come from (or near) Scoppieto, and SP.05.2023, initially thought to come from the middle Tiber Valley.

Archaeometric studies from Scoppieto show that vessels stamped by L. Plotidius Zosimus (OCK 1488) are composed of calcareous clay with a primarily potassium-enriched slip and some iron, in accordance with SEM-EDS results from Spoletino. Some typical mineral phases of Scoppieto and Spoletino involve quartz, K-feldspars, calcite, micas, plagioclase, and, in the case of Scoppieto, clinopyroxene (Bergamini, 2016).

The same principle applies to Group 4 (Figure 80) of samples SP.01.2023 and SP.15.2023, which showcase roughly similar mineralogical composition. Since SP.01.2023 originates from Scoppieto due to its *planta pedis* stamp, SP.15.2023 could also originate from Scoppieto or the middle Tiber Valley. SP.15.2023 is a particularly calcareous sample; therefore, it could be considered diagnostic of marine sedimentary deposits such as marl from Marine Pliocene (and Lower Pleistocene) sedimentary outcrops in the Tiber Valley (Olcese, 2004; Quinn, 2022).

Group 3 (Figure 79) comprises samples SP.07.2023 and SP.10.2023. EDS spectra of SP.07.2023 indicate a relatively lower amount of potassium in the slip and the matrix. Marti et al. (2018) discussed that potassium was only found in increased concentration in the Gallic and central Italian products, which was about two to three times the level in the body. On the contrary, potassium content was depleted in the Po Valley ware. For this reason, a Padanian origin seems more probable for SP.07.2023 and SP.10.2023. Finally, Group 2 (Figure 78) consists of samples SP.02.2023 and SP.14.2023. The comparatively moderate amount of carbonates in the ceramic body indicates a different provenance than the other samples. The lack of volcanic inclusions, such as pyroxenes, may infer that these samples belong to another central Italian workshop, such as Vasanello (VT) or the OctPro-OctSal group (Ettlinger, 1990; Grifa et al., 2019; Olcese, 2004).

Nevertheless, to confirm any of the above hypotheses, it is suggested to conduct further research. Analytical techniques such as inductively coupled plasma mass spectrometry (ICP-MS) and instrumental neutron activation analysis (INAA) can detect trace elements on both terra sigillata samples and geological clay samples, so they prove to be more beneficial for provenance studies (Quinn, 2022).

4.3 Conclusion

This preliminary study aimed to shed light on terra sigillata pottery found at Spoletino,

Viterbo, Italy. A multi-analytical approach (OM, SEM-EDS, and FTIR) was applied and provided information about raw materials, their selection and refinement, the production process, superficial treatments, firing conditions, post-depositional processes, and the origin of clay materials.

The ceramic body comprises quartz, mica, iron oxides, K-feldspar, plagioclase, hematite, diopside, carbonates, and clay minerals (kaolinite). Both the ceramic body and the slip were purified through levigation. Vessels were formed on the fast-turning wheel and dipped into the slip. EDS spectra of SP.04.2023, SP.01.2023, and SP.07.2023 generally indicate that the slip is more enriched in Al_2O_3, K_2O, and Fe_2O_3 than the body, while the latter has a greater CaO content. K_2O, Fe_2O_3, and CaO act as flux agents and lower the sintering temperature of clay.

SEM images display the sinterization of the slip and the matrix with the fusion of clay minerals. The presence of primary calcite in some samples with the persistence of kaolinite clay minerals in traces attests to a relatively lower firing range. Hematite results in the famous coral-red color of terra sigillata, while, according to the scientific literature, illite clays were used for the slip. The heterogeneous appearance of the matrix could be a consequence of the presence of iron oxides and fluctuations in the firing temperature.

Due to the moderate or weak optical activity observed in all samples, the firing temperature is estimated at 750–850 °C under controlled oxidizing conditions. The slip of SP.15.2023 and the external layer of the slip in SP.05.2023 show a high content of phosphates (P_2O_5). This fact could be attributed to post-depositional processes, along with the precipitation of secondary calcite.

The mineralogical composition of the sigillata samples in Group 1 (Figure 77) and Group 4 (Figure 80) is consistent with the Scoppieto (TR) workshop. This fact is strongly supported by the archaeological context with the presence of *planta pedis* stamps by L. Plotidius Zosimus (OCK 1488) and P. AV( ) GL ( ) (OCK 362.1). Group 3 (Figure 79) probably originates from the Po Valley, while Group 2 (Figure 78) is associated with some other central Italian workshop, such as Vasanello (VT) or the OctPro-OctSal group.

The pottery samples from Spoletino (VT) represent the high-quality tableware that is terra sigillata, made with fine, well-sorted clays. Clay selection and firing are vital components that render terra sigillata an outstanding technical achievement of Roman

times. The expertise of ancient potters is evident, even though the samples from Spoletino did not reach the high degree of sintering documented in some terra sigillata vessels from Arezzo or Gaul. Gaulish terra sigillata, for instance, could reach temperatures as high as 1050 °C during the firing process (Van Oyen, 2016).

It should be noted that the cistern in Spoletino, where the samples were found, was part of a Roman *villa*, which is considered a pottery consumption center. As of date, remains of pottery workshops, such as kilns, have not been discovered on the site. Therefore, terra sigillata was imported into the *villa* to be used by its residents. Spoletino is located near the Tiber River and was part of a complex trade system that took advantage of the river's navigability to carry goods. Scoppieto and other central Italian workshops would supply Spoletino with pottery and, subsequently, Rome since it was the capital of the Roman empire and the most significant market of the time.

The relatively high quality of terra sigillata found in Spoletino allows us to glimpse everyday life in a “rural” Roman *villa*. At the same time, it reflects the advanced socioeconomic connections of the *villa's* owners (Borgia, 2022). Application of additional analytical techniques, such as X-ray diffraction (XRD), inductively coupled plasma mass spectrometry (ICP-MS), and instrumental neutron activation analysis (INAA), could offer more in-depth information about the Tiber Valley trade by identifying more clearly the mineralogical composition and provenance of the selected fragments.

Bibliography

Artioli, G., & Angelini, I. (2010). *Scientific Methods and Cultural Heritage: An Introduction to the Application of Materials Science to Archaeometry and Conservation Science*. Oxford University Press.

Assenti, G. (2018). Terra sigillata italica. In A. Coralini (Ed.), *Pompei. Insula IX 8. Vecchi e Nuovi Scavi (1879-)* (pp. 589–608). Ante Quem.

Ballet, P., Bonifay, M., & Marchand, S. (2012). Africa vs Aegyptus : routes, rythmes et adaptations de la céramique africaine en Égypte. In S. Guédon (Ed.), *Entre Afrique et Égypte : relations et échanges entre les espaces au sud de la Méditerranée à l'époque romaine* (pp. 87–117). Ausonius Éditions.

Barberi, F., Buonasorte, G., Cioni, R., Fiordelisi, A., Foresi, L. M., Iaccarino, S. M., Laurenzi, M. A., Sbrana, A., Vernia, L., & Villa, I. M. (1994b). Plio-Pleistocene geological evolution of the geothermal area of Tuscany and Latium. *Memorie Descrittive Della Carta Geologica D'Italia, 49*, 77–134. https://usiena-air.unisi.it/handle/11365/41670?mode=full.1

Barraud, D., Bonifay, M., Dridi, F., & Pichonneau, J.-F. (1998). L'industrie céramique de l'Antiquité tardive. In H. Ben Hassen & L. Maurin (Eds.), *Uthina (Oudhna): La redécouverte d'une ville antique de Tunisie* (pp. 139–167). Ausonius Publications.

Bergamini, M., & Thirion-Merle, V. (2003). Una produzione firmata da Marcus Perennius Crescens a Scoppieto. In *Rei Cretariae Romanae Fautorum acta 38*, 133–144.

Bergamini, M. (2007). *Scoppieto: Il territorio e i materiali (Lucerne, Opus doliare, Metalli)* (Vol. 1). Quasar.

Bergamini, M. (2013). *Scoppieto: Lo scavo, le strutture, i materiali (coroplastica, marmi)* (Vol. 3). Quasar.

Bergamini, M. (2014). *Scoppieto: I materiali. Terra sigillata decorata a rilievo* (Vol. 4.1). Quasar.

Bergamini, M. (2015). *Scoppieto: I materiali. Ceramiche comuni* (Vol. 5). Quasar.

Bergamini, M. (2016). *Scoppieto: I materiali. Terra sigillata liscia, punzoni e matrici* (Vol. 4.2). Quasar.

Bes, P. (2015b). *Once upon a Time in the East: The Chronological and Geographical Distribution of Terra Sigillata and Red Slip Ware in the Roman East*.

Archaeopress Publishing Ltd.

Bimson, M. (1956). The technique of Greek black and terra sigillata red. *The Antiquaries Journal*. https://doi.org/10.1017/s0003581500061096

Bonfante, L., Nagy, H., & Collins-Clinton, J. (2015). *The Collection of Antiquities of the American Academy in Rome*. University of Michigan Press.

Bonifay, M. (2014). Céramique africaine et imitations: Où, quand, pourquoi? In R. Morais, A. Fernández & M. J. Sousa (Eds.), *As Produções Cerâmicas de Imitação na Hispania* (pp. 75–91). Ex Officina Hispana.

Borgia, E. (2022, September 25–30). *Eastern Sigillata vessels from the Roman Cistern at Spoletino (Civitella D'Agliano, Viterbo, Italy)* [Paper presentation]. RCFA: 32nd Congress of the Rei Cretariae Romanae Fautores, Athens, Greece.

Braekmans, D. & Degryse, P. (2017). Petrography: Optical Microscopy. In A. M. W. Hunt (Ed.), *Oxford Handbook of Archaeological Ceramic Analysis* (pp. 233–265). Oxford University Press.

Carandini, A., & Panella, C. (1978). *Ostia. 4 : Le Terme del Nuotatore. Scavo dell'ambiente XVI e dell'area XXV*. De Luca.

Carter, C. B., & Norton, M. G. (2007). *Ceramic Materials: Science and Engineering*. Springer Science & Business Media.

Coltorti, M., Di Battistini, G., Nappi, G., Renzulli, A., & Zeda, O. (1991). Structural setting and magmatic evolution of Montefiascone volcanic complex, vulsini district, central Italy. *Journal of Volcanology and Geothermal Research, 46*(1–2), 99–124. https://doi.org/10.1016/0377-0273(91)90078-e

Di Buduo, G., Costantini, L., Fiore, I., Marra, F., Palladino, D. M., Petronio, C., Rolfo, M. F., Salari, L., Ceruleo, P., Florindo, F., Gaeta, M., Gatta, M., Modesti, V., Pandolfi, L., & Sottili, G. (2020). The Bucobello 322 ka-fossil-bearing volcaniclastic-flow deposit in the eastern Vulsini Volcanic District (central Italy): Mechanism of emplacement and insights on human activity during MIS 9. *Quaternary International*. https://doi.org/10.1016/j.quaint.2020.04.04

Dragendorff, H. (1895). *Terra sigillata: ein Beitrag zur Geschichte der griechischen und römischen Keramik.*

Egerton, R. (2006). *Physical Principles of Electron Microscopy: An Introduction to TEM, SEM, and AEM.* Springer Science & Business Media.

Ettlinger, E. (1990). *Conspectus formarum terrae sigillatae Italico modo confectae*. Rudolf Habelt.

Fabbri, B., Gualtieri, S., & Shoval, S. (2014). The presence of calcite in archeological ceramics. *Journal of the European Ceramic Society*, *34*(7), 1899–1911. https://doi.org/10.1016/j.jeurceramsoc.2014.01.007

Freda, C., Palladino, D. M., Pignatti, S., Trigila, R., Onorati, G., & Poscolieri, M. (1990b). Volcano-tectonic scenario of Vulsini volcanoes (Central Italy) from LANDSAT-MSS images and digital elevation data. *Isprs Journal of Photogrammetry and Remote Sensing, 45*(5–6), 316–328. https://doi.org/10.1016/0924-2716(90)90026-8

Freestone, I. C., Meeks, N., & Middleton, A. (1985). Retention of Phosphate in Buried Ceramics: An Electron Microbeam Approach. *Archaeometry*, *27*(2), 161–177. https://doi.org/10.1111/j.1475-4754.1985.tb00359.x

Fülle, G. (1997). The Internal Organization of the Arretine Terra Sigillata Industry: Problems of Evidence and Interpretation. *Journal of Roman Studies, 87*, 111–155. https://doi.org/10.1017/s0075435800058111

Gliozzo, E. (2020a). Ceramics investigation: research questions and sampling criteria. *Archaeological and Anthropological Sciences, 12*(8). https://doi.org/10.1007/s12520-020-01128-9

Gliozzo, E. (2020b). Ceramic technology: How to reconstruct the firing process. *Archaeological and Anthropological Sciences*, *12*(11). https://doi.org/10.1007/s12520-020-01133-y

Goudineau, C. (1968). *Fouilles de l'École Française de Rome à Bolsena (Poggio Moscini): La céramique arétine lisse (1962-1967)* (Vol. 4). École Française de Rome.

Grifa, C., Germinario, C., De Bonis, A., Langella, A., Mercurio, M., Izzo, F., Smiljanic, D., Guarino, V., Di Mauro, S., & Soricelli, G. (2019). Comparing ceramic technologies: The production of Terra Sigillata in Puteoli and in the Bay of Naples. *Journal of Archaeological Science: Reports*, *23*, 291–303. https://doi.org/10.1016/j.jasrep.2018.10.014

Guarino, V., De Bonis, A., Grifa, C., Langella, A., Morra, V., & Pedroni, L. (2011). Archaeometric study on terra sigillata from Cales (Italy). *Periodico Di Mineralogia*, *80*(3). https://doi.org/10.2451/2011pm0030

Hayes, J. W. (1997). *Handbook of Mediterranean Roman Pottery* (Revised). University of Oklahoma Press.

Hayes, J. W. (2008). *Roman Pottery: Fine-ware Imports*. Athenian Agora: Results of

Exc.

Huggett, J. M. (2005). Sedimentary Rocks: Clays and Their Diagenesis. In R. C. Selley, L. R. M. Cocks & I. R. Plimer (Eds), *Encyclopedia of Geology* (pp. 62–70). Elsevier. https://doi.org/10.1016/B0-12-369396-9/00311-7.

Ionescu, C. & Hoeck, V. (2017). Electron Microprobe Analysis (EMPA). In A. M. W. Hunt (Ed.), *Oxford Handbook of Archaeological Ceramic Analysis* (pp. 288–304). Oxford University Press.

Kenrick, P. M. (1985). *Excavations at Sidi Khrebish, Benghazi (Berenice): The fine pottery* (Vol. 3.1). Society for Libyan Studies.

Kenrick, P. M. (1993). Italian Terra Sigillata: A Sophisticated Roman Industry. *Oxford Journal of Archaeology*, *12*(2), 235–242. https://doi.org/10.1111/j.1468-0092.1993.tb00294.x

Kiiskinen, H. (2013). *Production and Trade of Etrurian Terra Sigillata pottery in Roman Etruria and beyond between c. 50 BCE and c. 150 CE*. Turun Yliopisto University of Turku.

Leng, Y. (2009). *Materials characterization: Introduction to Microscopic and Spectroscopic Methods*. John Wiley & Sons.

Leon, Y., Sciau, P., Passelac, M., Sanchez, C., Sablayrolles, R., Goudeau, P., & Tamura, N. (2015). Evolution of terra sigillata technology from Italy to Gaul through a multi-technique approach. *Journal of Analytical Atomic Spectrometry*, *30*(3), 658–665. https://doi.org/10.1039/c4ja00367e

Loeschcke, S. (1909). *Keramische Funde in Haltern: ein Beitrag zur Geschichte der augusteischen Kultur in Deutschland*.

Luberti, G. M., Marra, F., & Florindo, F. (2017). A review of the stratigraphy of Rome (Italy) according to geochronologically and paleomagnetically constrained aggradational successions, glacio-eustatic forcing and volcano-tectonic processes. *Quaternary International, 438*, 40–67. https://doi.org/10.1016/j.quaint.2017.01.044

Lund, J. (2003). Eastern Sigillata B: a ceramic fine ware industry in the political and commercial landscape of the Eastern Mediterranean. In *Les céramiques en Anatolie aux époques hellénistiques et romaines. Actes de la Table Ronde d'Istanbul, 23-24 mai 1996. Istanbul* (pp. 125–136) https://www.persee.fr/doc/anatv_1013- 9559_2003_act_15_1_1035

Maritan, L., Mazzoli, C., Sasso, G. D., Mazzocchin, S., & Cipriano, S. (2018).

Archaeometric study on the ceramic production of the Roman Time potters' quarter of via Montona in Padua, Italy: From the reference groups to the regional distribution of coarse and fine ware. *European Physical Journal Plus*, *133*(9). https://doi.org/10.1140/epjp/i2018-12227-3

Marra, F., Petronio, C., Salari, L., Florindo, F., Giaccio, B., & Sottili, G. (2018). A review of the Villafranchian fossiliferous sites of Latium in the framework of the geodynamic setting and paleogeographic evolution of the Tyrrhenian Sea margin of central Italy. *Quaternary Science Reviews, 191*, 299–317. https://doi.org/10.1016/j.quascirev.2018.05.011

Marra, F., Costantini, L., Di Buduo, G., Florindo, F., Jicha, B. R., Monaco, L., Palladino, D. M., & Sottili, G. (2019). Combined glacio-eustatic forcing and volcano-tectonic uplift: Geomorphological and geochronological constraints on the Tiber River terraces in the eastern Vulsini Volcanic District (central Italy). *Global and Planetary Change, 182*, 103009. https://doi.org/10.1016/j.gloplacha.2019.103009

Mayya, S. (2019). *Environmental archaeology from a Roman Villa at Spoletino (Viterbo, Italy)* [Master's thesis, Universidade de Évora] Repositório Digital de Publicações Científicas. http://hdl.handle.net/10174/27750.

Medeghini, L., Mignardi, S., De Vito, C., & Conte, A. M. (2016). Evaluation of a FTIR data pretreatment method for Principal Component Analysis applied to archaeological ceramics. *Microchemical Journal*, *125*, 224–229. https://doi.org/10.1016/j.microc.2015.11.033

Mirti, P., Appolonia, L., & Casoli, A. (1999). Technological Features of Roman Terra Sigillata from Gallic and Italian Centres of Production. *Journal of Archaeological Science*, *26*(12), 1427–1435. https://doi.org/10.1006/jasc.1999.0435

Moevs, M. T. M. (2006). *Cosa: The Italian Sigillata*. University of Michigan Press.

Munsell Color Company (1975). *Munsell soil color charts*. Munsell Color Company.

Munsell Color Company (1994). *Munsell soil color charts*. Munsell Color Company.

Nappi, G., Antonelli, F., Coltorti, M., Milani, L., Renzulli, A., & Siena, F. (1998). Volcanological and petrological evolution of the Eastern Vulsini District, Central Italy. *Journal of Volcanology and Geothermal Research, 87*(1–4), 211–232. https://doi.org/10.1016/s0377-0273(98)00093-6

Olcese, G. (2004). Italian terra sigillata in Rome and the Rome area: production,

distribution, and laboratory analysis. In J. Poblome, P. Talloen, R. Brulet & M. Waelkens (Eds.), *Early Italian Sigillata: The Chronological Framework and Trade Patterns. Proceedings of the First International ROCT-Congress, Leuven, May 7 and 8, 1999* (pp. 279–298). Bulletin antieke beschaving.

Ortalli, J. (2017). Archaeology and funerary cult: The stratigraphy of soils in the cemeteries of Emilia Romagna (northern Italy). In J. Pearce & J. Weekes (Eds), *Death as a process: The archaeology of the Roman Funeral* (pp. 125–158). Oxbow Books.

Oswald, F., & Pryce, T. O. (1920). *An introduction to the study of terra sigillata treated from a chronological standpoint*. Longmans, Green and Co.

Oxé, A., Comfort, H., & Kenrick, P. M. (2000). *Corpus Vasorum Arretinorum: A Catalogue of the Signatures, Shapes and Chronology of Italian Sigillata*. Rudolf Habelt.

Peacock, D. P. S. (1982). *Pottery in the Roman World: An Ethnoarchaeological Approach*. Addison-Wesley Longman Limited.

Pedroni, L., & Soricelli, G. (1996). Terra sigillata da Cales. *Archeologia Classica, 48*, 169–91.

Pollard, A. M., & Heron, C. (2015). *Archaeological Chemistry*. Royal Society of Chemistry.

Pucci, G. (1980). Le officine ceramiche tardo-italiche. *Annales littéraires de l'Université de Besançon, 242*, 135–157.

Quaresma, J. C. (2013). Economic growth in the early and middle Imperial periods, pre-200 AD: an economic approach from a peripheral province, Lusitania. In T. Brennan & E. C. De Sena (Eds.), *The Roman Empire during the Severan Dynasty. Case Studies in History, Art, Architecture, Economy, and Literature* (pp. 377–413). Gorgias Press.

Quinn, P. S. (2013). *Ceramic Petrography: The Interpretation of Archaeological Pottery & Related Artefacts in Thin Section*. Archaeopress Publishing Ltd.

Quinn, P. S. (2022). *Thin Section Petrography, Geochemistry and Scanning Electron Microscopy of Archaeological Ceramics*. Archaeopress Publishing Ltd.

Reedy, C. L. (2008). *Thin-section Petrography of Stone and Ceramic Cultural Materials*. Archetype Publications.

Rice, P. M. (2015). *Pottery Analysis, Second Edition: A Sourcebook*. University of Chicago Press.

Rizzo, G. (1998). Samia etiamnunc in esculentis laudantur (Pl., N.H. XXXV, 160-161): I vasi «aretini» a Roma. *Mélanges De L'École Française De Rome. Antiquité*, *110*(2), 799–848. https://doi.org/10.3406/mefr.1998.2053

Roux, V. (2017). Ceramic manufacture: the chaîne opératoire approach. In A. M. W. Hunt (Ed.), *Oxford Handbook of Archaeological Ceramic Analysis* (pp. 101–113). Oxford University Press.

Schneider, G. (2017). Mineralogical and Chemical Alteration. In A. M. W. Hunt (Ed.), *Oxford Handbook of Archaeological Ceramic Analysis* (pp. 162–180). Oxford University Press.

Sciau, P., Sanchez, C., & Gliozzo, E. (2020). Ceramic technology: how to characterize terra sigillata ware. *Archaeological and Anthropological Sciences, 12*(9). https://doi.org/10.1007/s12520-020-01137-8

Shoval, S. (2017). Fourier Transform Infrared Spectroscopy (FT-IR) in Archaeological Ceramic Analysis. In A. M. W. Hunt (Ed.), *Oxford Handbook of Archaeological Ceramic Analysis* (pp. 509–530). Oxford University Press.

Soricelli, G. (1994). L'origine della "Tripolitanian Sigillata":"Produzione A della Baia di Napoli". In G. Olcese (Ed). *Ceramica romana e archeometria: Lo stato degli studi. Atti delle giornate internazionali di studio, Castello di Montegufoni (Firenze), 26-27 aprile 1993* (pp. 67–88). All'Insegna del Giglio.

Soricelli, G. (2004). La produzione di terra sigillata in Campania. In J. Poblome, P. Talloen, R. Brulet & M. Waelkens (Eds.), *Early Italian Sigillata: The Chronological Framework and Trade Patterns. Proceedings of the First International ROCT-Congress, Leuven, May 7 and 8, 1999* (pp. 299–307). Bulletin antieke beschaving.

Spanu, M. (2021). Breve rassegna sull'occupazione della Teverina laziale in epoca romana. *Orizzonti: rassegna di archeologia, XXII*, 155–166.

Sternini, M. (2016). Italian Sigillata: Some Insights into a Complex Reality. *Herom, 5*(2), 143–161. https://doi.org/10.11116/herom.5.2.1

Sternini, M. (2019). The production centres and river network of Italian terra sigillata between the Arno and Tiber valleys: a geographical point of view. *Journal of Roman Archaeology, 32*, 485–494. https://doi.org/10.1017/s1047759419000254

Stone, S. F. (2015). *Morgantina Studies* (Vol. 6). Princeton University Press eBooks. https://doi.org/10.1515/9781400845163

Theophanides, T. (2012). *Infrared spectroscopy: Materials Science, Engineering and Technology*. IntechOpen.

Tol, G., De Haas, T., & Attema, P. (2021). Terra sigillata in southern Latium: The evidence from the Pontine Region Project, 1987-2014. *Palaeohistoria*, 203–272. https://doi.org/10.21827/602fcb6729b40

Tyers, P. (1996). *Roman Pottery in Britain*. Routledge.

Van Oyen, A. (2015a). The Roman City as Articulated through Terra Sigillata. Oxford *Journal of Archaeology, 34*(3), 279–299. https://doi.org/10.1111/ojoa.12059

Van Oyen, A. (2016). *How Things Make History: The Roman Empire and its terra sigillata Pottery.* Amsterdam University Press.

Varekamp, J. C. (1979). Geology and petrology of the Vulsinian volcanic area (Latium, Italy). *Geologica Ultraiectina, 22*, 1–384.

Velde, B., & Druc, I. C. (1999). *Archaeological Ceramic Materials: Origin and Utilization.* Springer.

Washington, H. S. (1906). *The Roman Comagmatic Region*. Carnegie Institute of Washington.

Whitbread, I. K. (1995). *Greek Transport Amphorae: A Petrological and Archaeological Study.* British School at Athens.

Appendix

Photographs of the sampled fragments from terra sigillata vessels with a stamp.

Figure 1. Dish of *Conspectus* Form 3 with a stamp in *planta pedis* of L. Plotidius Zosimus (OCK 1488.8). Sample SP.01.2023.

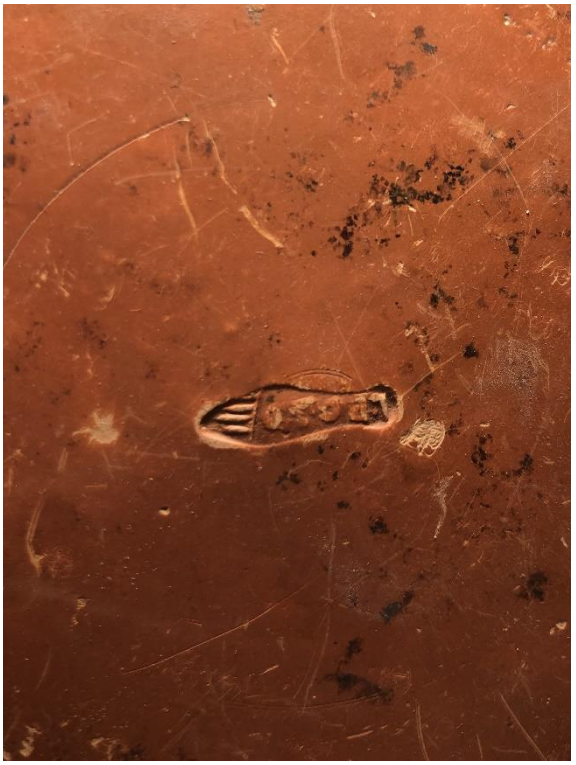

Figure 2. Bowl of *Conspectus* Form 33 with a stamp in *planta pedis*, too worn to be identified. One possible suggestion is that it refers to L. Plotidius (OCK 1484.8?). Sample SP.02.2023.

Figure 3. Bowl of *Conspectus* Form 36 with a stamp in *planta pedis* of L. Plotidius Zosimus (OCK 1488.6). Sample SP.03.2023.

Figure 4. Bowl of *Conspectus* Form 36 with a stamp in *planta pedis*, which is very worn but can be tentatively attributed to Scoppieto (OCK 1488.33?). Sample SP.04.2023.

Figure 5. Dish similar to *Conspectus* Form 39. Sample SP.07.2023.

Figure 6. Dish of *Conspectus* Form 3 with a stamp in *planta pedis* of L. Plotidius Zosimus (OCK 1488.39). Sample SP.09.2023.

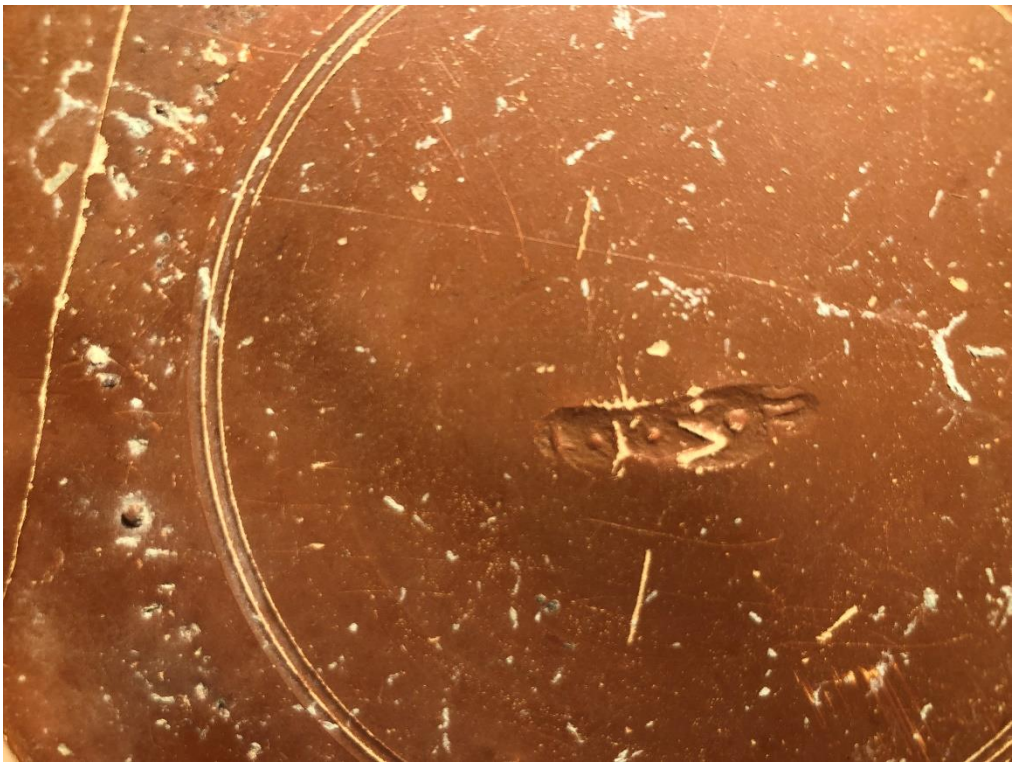

Figure 7. Dish of *Conspectus* Form 3 with a stamp of Cornelius in *planta pedis* (OCK 612). Sample SP.10.2023.

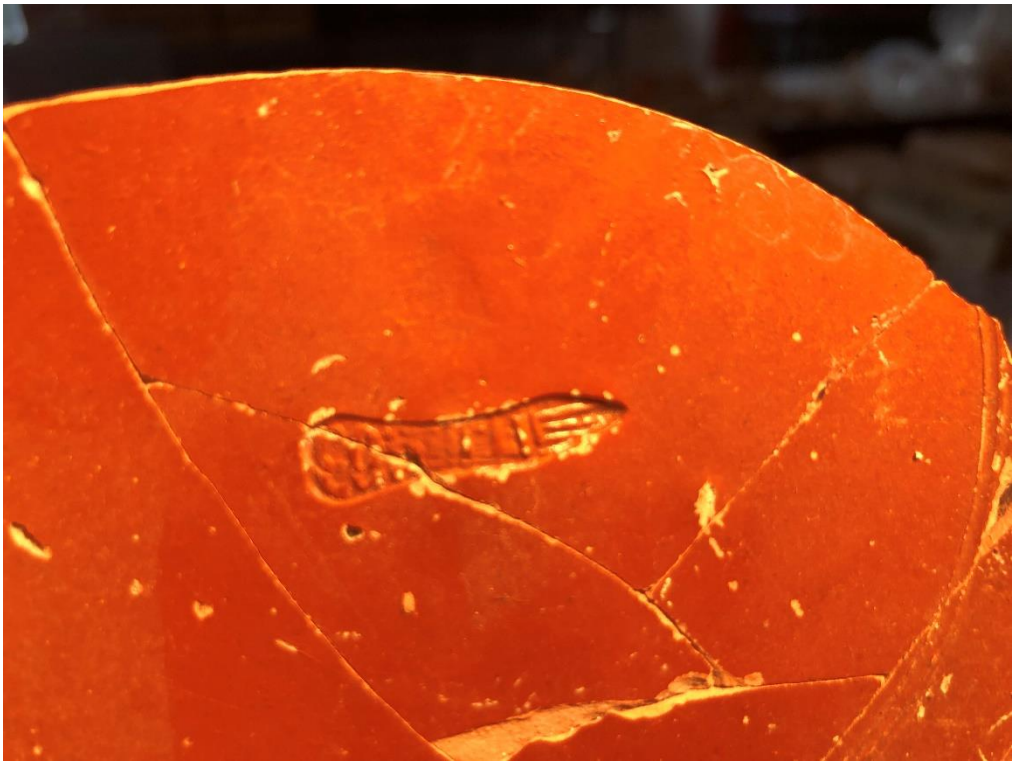

Figure 8. Bowl of *Conspectus* Form 36 with a stamp in *planta pedis* of P. AV( ) GL ( ) (OCK 362.1). Sample SP.13.2023.